UNIVERSIDAD AUTONOMA DE MADRID

Facultad de Ciencias
Departamento de Física de Materiales

# Quantum - Dot Single Photon Sources for Quantum Information Treatment

PhD Thesis

Presented by

Anna Kamila Nowak

Dissertation submitted for the degree of Doctor of Science at Universidad Autónoma de Madrid

Madrid, 2011

Facultad de Ciencias
Departamento de Física de Materiales

# Quantum - Dot Single Photon Sources for Quantum Information Treatment

*Emisores de fotones individuales basados en puntos cuánticos de semiconductores para el tratamiento cuántico de la información*

Tesis doctoral

Presentada por:

Anna Kamila Nowak
Licenciada en Ciencias Físicas

Director:

José Manuel Calleja Pardo
Catedrático de Universidad

Madrid, 2011

# Acknowledgements

I would like to express my deepest gratitude to the director of the PhD thesis, Prof. José Manuel Calleja, for introducing me into the world of semiconductor nanostructures and optical spectroscopy. I will always be very grateful to him for mostly personal and friendly treatment in my entire stay and work at the university.

I would also like to thank my colleagues of the group Eva, Maria, and Dipankar for friendly and successful collaboration. The long hours spent together in the laboratory were a great experience that I really appreciate. Part of the experimental results has been measured in the Laboratory of Ultra-fast Spectroscopy of Prof. Luis Viña. I am indebted with Lola Martin for collaboration in the TRPL measurements and her friendly companionship I received outside the laboratory. I would like to thank Profesors Herko van der Meulen, Luis Viña and Carlos Tejedor for fruitful discussions and help. Their ideas and advices were many times the clue to continue the scientific research in the right direction. Thanks to the other members of the SemicUAM group: Ligia, Francesca, Rita, Alberto, Alejandro, Carlos, Daniele, Dario, Emiliano, Guiherme y Jorge, for the exchange of ideas and nice company.

I would like to acknowledge to Luisa González, Yolanda González and José Ripalda, and their co-workers, who grew and provided us the quantum dot samples. I am also indebted to Elias for technical support and help in “emergency” cases; as well to Manolo and José for helium delivery.

During the past years I had the opportunity to stay at different laboratories and collaborate with other groups to get insight into other fields and techniques. I would like to express my special gratitude to Dr Ewa Popko (Wroclaw University of Technology) for supervising me in the predoctoral studies and encouraging me to study physics at all. I am also grateful to Prof. Grzegorz Karczewki (Polish Academy of Science, Warsaw), thanks to whom I got in touch with SemicUAM group, and to his colleagues Dr Valery Kolkovsky and Dr Marek Guziewicz for a

short training in sample grow and contact annealing. I am also indebted with Prof. Atac Imamoglu, Dr Tomas Voltz and Dr Martin Winger (Institute for Quantum Electronics, ETH Zurich) for inviting me to their laboratory and sharing ideas and experimental solutions.

Thanks also to the other members of the department: Ivan, Marta, Javi, Juancho, Maysoun, Olga, Susana, Emma, Nina and Mariano for their cheerful company, help, lunch time and really great time spent together as well outside the university.

Finally, I would like to thank to all my friends and family, especially to my parents and Esteban for their love and greatest support I have been receiving every day.

# Introducción y Objetivos

Las aplicaciones de los objetos nanométricos para el desarrollo de fuentes de fotones individuales se han hecho muy atractivas para la comunidad científica en las últimas tres décadas. Ello es debido a su potencial implementación en tecnologías de información quántica. El uso de los sistemas que obedecen las leyes de la mecánica quántica para la codificación, manipulación o lectura de la información cuántica da nuevas posibilidades en comparación con su equivalente clásico [1]. Además, los emisores de fotones individuales (EFI) garantizan la seguridad máxima de las comunicaciones a través de protocolos criptográficos cuánticos [2]. Todo ello constituye una gran motivación para el desarrollo de emisores y detectores de fotones individuales para el tratamiento quántico de la información.

El grupo de los sistemas más prometedores para el desarrollo de fuentes de fotones individuales emitidos *a demanda* incluye puntos cuánticos (PC) de semi-conductores [3]. En comparación con átomos [4] o iones [5], los PC de semiconductores son fáciles de usar, escalables y de diseño flexible debido al desarrollo de nuevas tecnologías de crecimiento de hetero-estructuras. Sin embargo, dichos PC poseen algunas desventajas como tiempo de coherencia corto (comparando con los átomos) o la variabilidad de sus propiedades dependiendo del tamaño, composición, tensiones o su entorno electrostático propio. La intensa investigación para mejorar y desarrollar las tecnologías de crecimiento de las heterostructuras semiconductoras, junto con las técnicas de espectroscopía muy precisas, abre nuevas posibilidades para el diseño de nuevas nano-estructuras e investigación del espectro de la emisión óptica de un solo PC. Todos estos requisitos previos han permitido el intenso desarrollo de los EFI [6]. Su eficiencia y control todavía pueden ser mejorados al acoplar excitones de un PC con los modos electromagnéticos de una micro-cavidad mediante el posicionamiento preciso de un solo PC dentro de la cavidad fotónica [7].

El diseño de un EFI adecuado para las tecnologías de la información cuántica requiere un conocimiento detallado de la estructura electrónica de un PC individual. Dicha estructura está determinada por la estructura cristalina del PC y por todos los factores que influyen en ella. Además, la interacción de Coulomb entre los portadores presentes dentro del PC afecta notablemente a su estructura electrónica y, consecuentemente, a su espectro de emisión óptica y la dinámica de dicha emisión. La influencia del tamaño y de la forma sobre el espectro de

luminiscencia, la dinámica y la emisión de fotones individuales por un punto cuántico se puede encontrar en la referencia [8]. Los efectos del potencial piezoeléctrico (presente en los materiales tipo zinc-blenda) [9] junto con tensiones dentro de la red cristalina (debido al desajuste de las constantes de red) [10] también afectan a la estructura electrónica y a las transiciones ópticas del PC.

Otros factores como la influencia de campos externos o los efectos intrínsecos influyen en las propiedades ópticas de un PC, como por ejemplo, los cambios de energía o el desdoblamiento de niveles debido a un campo magnético [11]. Asimismo, un campo eléctrico externo produce el desplazamiento de los niveles energéticos o la creación de nuevos estados excitonicos (excitones cargados) [12]. La excitación óptica con energía y/o intensidad adecuada introduce cambios en la respuesta del PC, tales como la aparición de resonancias con estados excitados, o la formación de múltiples estados excitonicos debido a la interacción de Coulomb entre las cargas foto-creadas. Por otra parte, se ha observado la modulación del desdoblamiento de estructura fina en un campo magnético [13] y eléctrico [14]. También se han observado cambios en dicho desdoblamiento mediante la variación de la energía de excitación [15] o debido a tensiones de la red cristalina [16].

La estructura electrónica del PC, su dinámica y la emisión de fotones individuales experimentan diferentes efectos debido a la temperatura. Los fonones pueden influir la población de los portadores confinados dentro de un PC, proporcionar los canales no-radiativos de recombinación de los excitones, o contribuir a la emisión de fondo [9]. Por lo tanto, la mayoría de los experimentos ópticos con nano-estructuras semiconductoras se realiza a temperaturas criogénicas. Sin embargo, se ha medido la emisión de fotones individuales a temperatura ambiente en PC coloidales de CdSe/ZnS [3].

La interacción de Coulomb entre las cargas es responsable de los efectos colectivos (*many-body*) y puede afectar a la estructura electrónica y a las propiedades ópticas de un material. Un aumento de la densidad de las cargas libres en un semiconductor intensifica la correlación entre los portadores y la interacción de intercambio, que influye la estructura de bandas [17]. El caso más frecuente es el desplazamiento de los niveles hacia más altas o más bajas energías y por lo tanto la renormalización de la banda prohibida (en inglés *Band-gap Renormalization* – BGR). Este fenómeno afecta no solamente a los semiconductores en volumen o a los pozos quánticos [18], sino también a los hilos cuánticos [19] y PC [14].

El objetivo principal de ésta Tesis es el estudio de las propiedades de los puntos individuales de InP/GaInP como potenciales EFI. La razón por la cual se

han elegido estos PC (en vez de el bien conocido InAs/GaAs) es la búsqueda de EFI en el rango visible, dado que su emisión se produce entre 660 nm y 740 nm, por lo cual puede ser medida eficazmente con los detectores comerciales (max. eficiencia para 670 nm). Además, el sistema InP/GaInP se caracteriza por la discontinuidad negativa de la banda de valencia (ingl. *band offset*) por lo cual los huecos están confinados en un PC únicamente por las tensiones locales del propio PC. Esto puede producir efectos que no se observan en otro tipo de PC, por ejemplo la renormalización de la banda prohibida.

Para investigar las propiedades ópticas de los PC de InP y la dinámica de su emisión se han usado diferentes técnicas experimentales. Se ha diseñado y desarrollado el sistema de medida de Correlación de Fotones Individuales (ingl. *Single Photon Correlation* – SPC) para el propósito de ésta Tesis. El método SPC junto con micro-fotoluminiscencia (ingl. *Photoluminescence* – PL), PL de Excitación (PLE) y PL resuelta en tiempo (ingl. *Time-Resolved PL* – TRPL) proporciona una información completa sobre las propiedades ópticas de un PC individual como posible EFI.

La Tesis está organizada de la siguiente forma:

El Capitulo 2 es una introducción a los temas de las fuentes de fotones individuales para el tratamiento cuántico de la información. Se da una breve descripción del fotón como portador de información cuántica – *qubit*, continuando con las propiedades generales de los PC de semiconductores, y finalmente se describen los estados excitonicos de dichos PC y los efectos de confinamiento.

El Capitulo 3 describe diferentes tipos de espectroscopia utilizados para el estudio de las propiedades ópticas y de la estructura electrónica de los PC de InP/GaInP. Una descripción del método de la Correlación de Fotones Individuales junto con el interferómetro de Hanbury-Brown y Twiss es más detallada debido a la realización y desarrollo de dicho método especialmente para ésta Tesis.

El Capitulo 4 presenta los resultados más relevantes sobre la emisión óptica de los PC de InP/GaInP. Los espectros de luminiscencia revelan multitud de líneas de emisión procedente de distintos PC. Las energías de los estados excitados se obtienen mediante PLE para distintos PC. La dinámica de la emisión de los distintos PC se obtiene midiendo PL resuelta en tiempo (TRPL). También se presentan los resultados sobre la influencia de temperatura y modo de excitación óptica sobre dicha dinámica.

El Capitulo 5 se dedica a los espectros de PL y PLE medidos para unos PC de InP más pequeños. Se observa un continuo y sistemático corrimiento hacia el rojo de

las líneas de emisión de los excitones. El fenómeno se ve claramente para las energías e intensidades de excitación crecientes. Éste comportamiento se asocia al efecto de BGR. Además, las energías de emisión de los excitones presentan un corrimiento hacia el rojo coincidiendo con el aumento de la absorción (los máximos de la PLE) lo cual sugiere que la población de los estados excitados determina el BGR en nuestros PC. Se observa también una modificación del desdoblamiento de la estructura fina del exciton. Éste fenómeno se analiza en términos de los efectos colectivos sobre la estructura electrónica de un PC.

El Capitulo 6 proporciona los resultados de la correlación de fotones en los PC de InP/GaInP. Se analizan los efectos de la temperatura y excitación sobre la eficiencia y dinámica de los PC como FFI. Al aumentar la temperatura se observan diferentes comportamientos en la dinámica de emisión de fotones individuales en distintos PC. Se analiza la influencia del tamaño de un PC sobre la recombinación de los excitones. También se investigan los efectos de la excitación *cuasi*-resonante sobre la emisión de fotones individuales en dichos PC.

Las conclusiones más relevantes de la Tesis se dan en el Capitulo 7.

# Referencias

[1] *Véase por ejemlo*: Michael A. Nielsen, Isaac L. Chuang, "*Quantum computation and quantum information"*, Cambridge University Press (2000).

[2] C. H. Bennett, F. Bessette, G. Brassard, L. Salvail and J. Smolin "*Experimental Quantum Cryptography*" Journal of Cryptology vol.5, no.1, pp. 3-28 (1992).

[3] P. Michler, A. Imamoglu, M. D. Mason, P. J. Carson, G. F. Strouse, and S. K. Buratto, Nature (London) 406, 268 (2000).

[4] H. J. Kimble, M. Dagenais, L. Mandel, Phys. Rev. Lett. 39, pp. 691-694 (1977).

[5] F. Diedrich and H. Walther, Phys. Rev. Lett. 58, pp. 203-206 (1987).

[6] A. Dousse, L. Lanco, J. Suffczyński, E. Semenova, A. Miard, A. Lemaître, I. Sagnes, C. Roblin, J. Bloch, and P. Senellart, Phys. Rev. Lett. 101, 267404 (2008).

[7] K. Hennessy, A. Badolato, M. Winger, D. Gerace, M. Atature, S. Falt, E. L. Hu, and A. Imamoglu, Nature 445, 896 (2007).

[8] A. K. Nowak, E. Gallardo, D. Sarkar, H. P. van der Meulen, J. M. Calleja, J. M. Ripalda, L. González, and Y. González, Phys. Rev. B 80, 161305 (2009).

[9] D. Sarkar, H. P. van der Meulen, J. M. Calleja, J. M. Becker, R. J. Haug, and K. Pierz, Phys. Rev. B 78, 241305 (2008).

[10] M. Wimmer, S. V. Nair, and J. Shumway, Phys. Rev. B **73**, 165305 (2006).

[11] R. Rinaldi, P. V. Giugno, and R. Cingolani, H. Lipsanen, M. Sopanen, and J. Tulkki, J. Ahopelto, Phys. Rev. Lett. 77, 342–345 (1996).

[12] N. A. J. M. Kleemans, J. van Bree, A. O. Govorov, J. G. Keizer, G. J. Hamhuis, R. Nötzel, A. Yu. Silov and P. M. Koenraad, Nature Physics 6, pp. 534-538 (2010).

[13] R. M. Stevenson, R. J. Young, P. Atkinson, K. Cooper, D. A. Ritchie and A. J. Shields, Nature (London) 439, 179-182 (2006).

[14] A. Mohan, M. Felici, P. Gallo, B. Dwir, A. Rudra, J. Faist & E. Kapon, Nature Photonics 4, 302 - 306 (2010).

[15] A. K. Nowak, E. Gallardo, H. P. van der Meulen, J. M. Calleja, J. M. Ripalda, L. González, and Y. González, Phys. Rev. B **83**, 245447 (2011).

[16] G.W. Bryant, M. Zieliński, Natalia Malkova, James Sims, W. Jaskólski, and J. Aizpurua PRL 105, 067404 (2010) and references therein.

[17] W. F. Brinkman and T. M. Rice, Phys. Rev. B 7, 4, pp. 1508 – 1523 (1973)

[18] S. Schmitt-Rink, C. Ell, S. W. Koch, H. E. Schmidt and H. Haug, Solid State Communications 52, 123 (1984).

[19] W. Wegscheider, L. N. Pfeiffer, M. M. Dignam, A. Pinczuk, K. W. West, S. L. McCall and R. Hull, Phys. Rev. Lett. **71**, 4071 (1993).

# Conclusiones

La presente tesis aporta un estudio detallado de las propiedades ópticas y de la estructura electrónica de puntos cuánticos (PC) de InP/GaInP como potenciales emisores de fotones individuales. Las conclusiones generales de este trabajo se presentan en continuación.

La emisión óptica de PC pequeños de InP (1-2 nm de altura) incluidos en una matriz de GaInP ha sido estudiada bajo diferentes condiciones de excitación y temperatura. La separación media entre los PC (~0.2 μm) habilita el acceso óptico a PC individuales sin necesidad de usar mascaras o mesas. El sistema experimental de micro-PL permite la observación repetible de las líneas de emisión de un solo PC en el rango espectral: 660 nm – 670 nm (1.85 eV – 1.88 eV).

Los espectros de micro-PLE tomados para varios PC revelan picos de intensidad de luminiscencia por debajo de la *wetting layer* (WL) correspondientes a transiciones entre estados excitados. Para energías mayores que 1.88 eV se observa un incremento y ensanchamiento del espectro de PLE correspondiente a la WL. El tamaño pequeño de los PC junto con el desajuste (*band offset*) pequeño de la banda de valencia (VB) origina una hibridación de los estados excitados con el continuum de la WL, especialmente en la banda de valencia donde los huecos están confinados principalmente por las tensiones de la red cristalina en el entorno del PC (*band offset* negativo).

Las diferencias en el espectro (energía de ligadura del biexciton y el desdoblamiento de la estructura fina) y en los tiempos de recombinación del exciton observadas en distintos PC proporcionan información sobre el tamaño de los mismos. Los tiempos de recombinación medidos en nuestros PC están de acuerdo con los valores calculados por Wimmer *et al.* (2006). También la energía de ligadura de biexciton está en el rango calculado. Aunque los valores presentados por Wimmer *et al.* han sido calculados para los PC más grandes que nuestros, los resultados obtenidos en ésta Tesis sugieren que los PC de InP/GaInP están en el régimen de confinamiento intermedio.

La dinámica de la emisión de los PC individuales ha sido medida para diferentes potencias de excitación y a diferentes temperaturas. Los tiempos de recombinación de exciton y biexciton siguen las tendencias esperadas. El tiempo de vida del exciton aumenta progresivamente con la potencia mientras que el del biexciton permanece constante. Los experimentos de TRPL en función de temperatura revelan diferentes comportamientos del tiempo de recombinación dependiendo del tamaño del PC. Ello es debido a dos procesos térmicamente activados que compiten entre sí: 1) El cambio de espín (mediado por fonones) del estado oscuro de exciton pasando al estado brillante, lo que disminuye el tiempo de recombinación y 2) La excitación térmica de los portadores a estados excitados o la WL. Dependiendo del proceso dominante, el tiempo de recombinación aumenta (PC pequeños), disminuye (PC grandes) o permanece constante si los dos procesos se compensan. Por encima de 50 K todos los PC presentan una disminución del tiempo de recombinación debido al escape de los portadores a la WL mediado por fonones.

Se observa un continuo y sistemático desplazamiento hacia rojo de las líneas de emisión de exciton con el incremento de la energía y/o intensidad de excitación. Este efecto se explica por la renormalización del gap (BGR) debida a la interacción colectiva de los portadores. El cambio de la energía de emisión de un exciton puede ser hasta 0.4 meV. Los mínimos de la energía de emisión corresponden al aumento de la intensidad de emisión en el espectro PLE. El efecto de BGR es debido a la hibridación de los estados excitados de los huecos con el continuum de la WL. El pequeño tamaño de los PC de InP/GaInP acerca los estados excitados a la WL habilitando la hibridación.

Se observa una modulación del desdoblamiento de la estructura fina $\Delta_{FSS}$ (hasta un 10%) para la excitación cuasi-resonante en un estado excitado, que presenta un desdoblamiento de polarización propio. Este fenómeno es causado por el efecto de BGR dependiente de la polarización de excitación y emisión. La ventaja del control de $\Delta_{FSS}$ por la energía de excitación sobre otros es el empleo de medios exclusivamente ópticos y la reversibilidad del proceso. Sin embargo la cancelación total del desdoblamiento mediante de este método es probablemente imposible.

Las medidas de auto-correlación de la emisión excitonica de los PC de InP muestran un desagrupamiento (antibunching) de fotones tipico de la emisión de fotones individuales. Para excitación no resonante los valores de $g^{(2)}(0)$ están por debajo de 0.2, incluso para temperaturas altas. Ello es debido a la baja contribución de la luminescencia del fondo a la emisión del PC. Para excitación cuasi-resonante en los estados excitados del PCs se observan valores incluso más bajos (≈0.1) por

la menor influencia de procesos de relajación lenta o de los procesos de carga de defectos. Para bajos niveles de excitación el tiempo de recarga del PC (tiempo de *antibunching*) está en el rango de 0.5 hasta 0.8 ns, dependiendo del tamaño del PC o la temperatura.

Se observa una reducción del tiempo de recarga en la función de correlación $g^{(2)}(\tau)$ al acercar la energía de excitación al estado excitado del PC (estado p). Ello se interpreta como el incremento de la probabilidad de absorción a medida que la excitación se acerca a la energía del estado p. La bajada del tiempo de recarga al aumentar la potencia de excitación se explica de forma similar.

La función de auto-correlación del exciton medida para temperatura variable revela el mismo comportamiento que las medidas de TRPL, debido a dos procesos activados térmicamente: 1) activación térmica de los huecos (tiempo de recarga ($\tau_R$) aumenta), y 2) Transición del estado oscuro (DX) al estado brillante (BX) del exciton lo que aumenta su ocupación y reduce el tiempo $\tau_R$. La energía de activación térmica de los huecos ha sido estimada entre 7 meV y 30 meV dependiendo del tamaño del PC. La transición DX – BX tiene energía de activación térmica de 3.6 meV en el PC más grande de los tres estudiados.

# Contents

# Abbreviations

| | |
|---|---|
| APD | avalanche photodiode |
| AFM | Atomic Force Microscopy |
| BS | beam splitter |
| BX | bright exciton |
| CB | conduction band |
| CCD | charged-coupled device |
| DX | dark exciton |
| *e-h* | electron-hole pair |
| FSS | fine structure splitting |
| FWHM | full width at half maximum |
| H | horizontal |
| HBT | Hanbury-Brown and Twiss interferometer |
| IRF | instrumental response function |
| LA | longitudinal acoustic |
| LO | longitudinal optic |
| MBE | Molecular Beam Epitaxy |
| MOCVD | Metal Organic Chemical Vapour Deposition |
| PL | Photoluminescence |
| PLE | Photoluminescence Excitation |

| | |
|---|---|
| QD | quantum dot |
| QW | quantum well |
| QWR | quantum wire |
| SEM | Scanning Electron Microscopy |
| SPC | Single Photon Correlation |
| SPE | Single Photon Emission |
| TCSPC | Time-Correlated Single Photon Counting |
| TO | transverse optical |
| TRPL | Time-Resolved Photoluminescence |
| VB | valence band |
| V | vertical |
| WL | wetting layer |
| X ($X^0$) | exciton (neutral) |
| XX ($XX^0$) | biexciton (neutral) |
| $X^{1-}$ ($X^{1+}$) | negative (positive) trion |

# Chapter 1

## Introduction and Objectives

Application of quantum-mechanical objects as single-photon sources has become very attractive to the scientific community in the last few decades for their potential implementation in the quantum-information technologies. Using of quantum-mechanical objects for encoding, manipulation or measuring of the quantum-information gives new possibilities in computational science, which is much more efficient than its classical equivalent [1]. Moreover, the single photon emitters (SPE) can guarantee an unconditional security in the communication via quantum cryptography protocols [2]. All this is a great motivation for studying and developing of the single-photon sources and single-photon detectors for quantum-information treatment.

The group of the most promising systems for single photon emission "on demand" includes semiconductor quantum dots (QDs) [3]. In comparison to other SPE, i.e. atoms [4] or ions [5], semiconductor QDs are easy to use, scalable and flexible to design due to newly developed technologies of nanostructures growth. However, they have some important disadvantages, like the short decoherence time (compared to atoms) or the variability of their properties depending on their size or crystallographic structure (i.e. composition, strain and electrostatic environment). The intense research on semiconductor nanostructure growth, together with highly precise spectroscopy techniques, is giving the possibility to design new nano-structures and study their optical emission spectrum at the single QD level. These prerequisites have enabled the development of efficient SPEs [6]. Their efficiency and control can be greatly improved by coupling the QD excitons to confined electromagnetic modes by precise positioning of the QD inside a photonic cavity, as reported by Hennessy et al. [7].

Designing of a SPE adequate for, quantum-information technologies, requires a detailed knowledge of the electronic structure of an individual QD. This

structure is determined firstly by the crystal structure of the dot, and all factors affecting it. Also, Coulomb interaction between carriers present in the QD have an important effect on its electronic structure and, consequently, on the optical spectrum and emission dynamics of the QD (see §2.3). The QD size and shape influence on luminescence spectrum, optical dynamics and single photon emission have been studied in Ref. [8]. The effects of piezoelectric potential (present in zincblende materials) [9] and strain [10] (due to the crystal lattice mismatch) also affect electronic structure and optic transitions of a dot.

Other factors like external fields or intrinsic effects inflence the optical properties of an individual QD as well. The electronic levels experience energy shifts and energy splittings under an external magnetic field [11]. The external electric field introduces shift of energy levels or creates new (charged) excitonic states [12]. Optical excitation with proper energy and/or intensity results in changes in the QD response, as the appearance of resonances at QD excited states, or the formation of a manifold of excitonic states resulting from the Coulomb interaction between the photo-created carriers. Moreover, a modulation of the fine structure splitting has been observed under magnetic [13] and electric [14] fields, as well as under variable excitation energy [15] or due to strain in the crystal lattice [16].

The QD electronic structure, its dynamics and single photon emission properties are also affected by temperature. Phonons can influence the population of carriers confined inside the QD, provide non-radiative channels for exciton recombination and also can contribute to the background emission [9]. Thus, the majority of the optics experiments performed on semiconductor nanostructures is done at cryogenic temperatures. However, single photon emission at room temperature was reported in CdSe/ZnS colloidal QDs [3].

The Coulomb interaction between carriers inside a crystal lattice is responsible for many-body effects, which affect the electronic structure and optical properties of the material. Increase of the free-carrier density in a semiconductor enhances the influence of correlation and exchange interaction on the band structure [17]. The most frequent effects are energy level shifts towards lower or higher energies, and in particular the band gap “renormalization” causing a red-shift in the emission spectrum. This phenomenon influences the band structure, not only in bulk semiconductors or quantum wells (QW) [18], but also in wires (QWr) [19] and QDs [14].

The main objective of this Thesis is the investigation of the optical properties of individual InP/GaInP QDs as potential SPEs. The main reason for studying these QDs instead of the well known InAs/GaAs QDs is to search for SPE

in the visible range, as their luminescence lies in the wavelength range from 660 nm to 740 nm, which meets the efficiency maximum of the commercial detectors. Additionally, InP/GaInP QDs have negative band offset in the valence band, and hence holes are confined only by strain. This influences the wave function of the confined carriers and origins effects, which are not observed in other type of QDs, like band-gap renormalization.

In order to investigate the optical properties of the InP QDs and their emission dynamics different experimental techniques have been used. The Single-Photon Correlation (SPC) method has been developed especially for the purpose of this research. Complemented with micro-Photoluminescence (PL), Photo-luminescence Excitation (PLE) and Time-Resolved PL (TRPL) experiments, the SPC method gives good insight into the optical properties of individual InP/GaInP QDs and dynamic processes occurring in these SPE.

This thesis is organized as follows:

Chapter 2 gives an introduction to the topics of single photon sources for quantum information treatment. First, the insight to the single photon emission is given. In continuation, general properties of the semiconductor QDs, their growth process and photon-emission is discussed. Finally, details on the excitonic states in the QD and the confinement effects are presented.

Chapter 3 describes the different types of spectroscopy used for studding the optical properties and electronic structure of InP/GaInP QDs. Special emphasis is put on the Single-Photon Correlation (SPC) method where the Hanbury-Brown and Twiss interferometer and photon correlation are described.

Chapter 4 presents the most relevant results on optical emission of the InP/GaInP QD sample. Luminescence spectra measured by micro-PL reveal a manifold of emission lines deriving from different individual QDs. The excited states energies of single QDs are obtained from micro-PLE spectra. Optical dynamics of individual QDs were studied by TRPL. Different decay characteristics (together with emission energies) reveal differences in QD sizes. The influence of excitation intensity and temperature on the QD emission is discussed.

Chapter 5 shows PL and PLE measurements in small InP/InGaP single QDs which reveal a continuous and systematic red shift of the exciton emission as the excitation energy or the excitation intensity increases. This behaviour is attributed to the BGR effect. Additionally the exciton emission energy presents red-shift dips in a one-to-one correspondence with the PLE peaks, showing that the population of

the QDs excited states determines this type of BGR in single quantum dots. Modification of the exciton fine-structure splitting by simply changing the excitation energy is observed. This phenomenon is discussed in terms of influence of many body-effects on the electronic structure.

Chapter 6 reports results of the photon correlation measurements on single InP/GaInP QDs. Temperature and excitation effects on efficiency and dynamics of the SPEs are presented. Different temperature behaviors in the emission dynamics are observed for distinct QD. The influence of the QD size on the exciton decay is discussed. The quasi-resonant excitation at one of the excited states also reveals changes the QD dynamics while maintaining the efficient single photon emission.

The main conclusions of the Thesis are presented in Chapter 7.

# References


[1] see for instance: Michael A. Nielsen, Isaac L. Chuang, *"Quantum computation and quantum information"*, Cambridge University Press (2000).

[2] C. H. Bennett, F. Bessette, G. Brassard, L. Salvail and J. Smolin "*Experimental Quantum Cryptography*" Journal of Cryptology vol.5, no.1, pp. 3-28 (1992).

[3] P. Michler, A. Imamoglu, M. D. Mason, P. J. Carson, G. F. Strouse, and S. K. Buratto, Nature (London) 406, 268 (2000).

[4] H. J. Kimble, M. Dagenais, L. Mandel, Phys. Rev. Lett. 39, pp. 691-694 (1977).

[5] F. Diedrich and H. Walther, Phys. Rev. Lett. 58, pp. 203-206 (1987).

[6] A. Dousse, L. Lanco, J. Suffczyński, E. Semenova, A. Miard, A. Lemaître, I. Sagnes, C. Roblin, J. Bloch, and P. Senellart, Phys. Rev. Lett. 101, 267404 (2008).

[7] K. Hennessy, A. Badolato, M. Winger, D. Gerace, M. Atature, S. Falt, E. L. Hu, and A. Imamoglu, Nature 445, 896 (2007).

[8] A. K. Nowak, E. Gallardo, D. Sarkar, H. P. van der Meulen, J. M. Calleja, J. M. Ripalda, L. González, and Y. González, Phys. Rev. B 80, 161305 (2009).

[9] D. Sarkar, H. P. van der Meulen, J. M. Calleja, J. M. Becker, R. J. Haug, and K. Pierz, Phys. Rev. B 78, 241305 (2008).

[10] M. Wimmer, S. V. Nair, and J. Shumway, Phys. Rev. B **73**, 165305 (2006).

[11] R. Rinaldi, P. V. Giugno, and R. Cingolani, H. Lipsanen, M. Sopanen, and J. Tulkki, J. Ahopelto, Phys. Rev. Lett. 77, 342–345 (1996).

[12] N. A. J. M. Kleemans, J. van Bree, A. O. Govorov, J. G. Keizer, G. J. Hamhuis, R. Nötzel, A. Yu. Silov and P. M. Koenraad, Nature Physics 6, pp. 534-538 (2010).

[13] R. M. Stevenson, R. J. Young, P. Atkinson, K. Cooper, D. A. Ritchie and A. J. Shields, Nature (London) 439, 179-182 (2006).

[14] A. Mohan, M. Felici, P. Gallo, B. Dwir, A. Rudra, J. Faist & E. Kapon, Nature Photonics 4, 302 - 306 (2010).

[15] A. K. Nowak, E. Gallardo, H. P. van der Meulen, J. M. Calleja, J. M. Ripalda, L. González, and Y. González, Phys. Rev. B **83**, 245447 (2011).

[16] G.W. Bryant, M. Zieliński, Natalia Malkova, James Sims, W. Jaskólski, and J. Aizpurua PRL 105, 067404 (2010) and references therein.

[17] W. F. Brinkman and T. M. Rice, Phys. Rev. B 7, 4, pp. 1508 – 1523 (1973)

[18] S. Schmitt-Rink, C. Ell, S. W. Koch, H. E. Schmidt and H. Haug, Solid State Communications 52, 123 (1984).

[19] W. Wegscheider, L. N. Pfeiffer, M. M. Dignam, A. Pinczuk, K. W. West, S. L. McCall and R. Hull, Phys. Rev. Lett. **71**, 4071 (1993).

# Chapter 2

# Single Photon Sources for Quantum Information Applications

This chapter is organized as follows. A brief introduction to the use of single photons for quantum-information applications will be given in sections §2.1 and §2.2. The properties of the semiconductor QDs, their growth process and photon-emission engineering will be presented in section §2.3. Finally, the detailed description of the excitonic states formation in the QD and the confinement effects will be given in section §2.4.

**Photons as "Flying" Qubits**

A single photon characterized by its momentum, polarization and energy. These are the degrees of freedom which are useful to encode information in the photon, i.e., to use the photon as a perfect *qubit* for the quantum-information treatment [1]. Additionally, photons propagate with velocity of light c, they weakly interact with the environment over long distances, and they can be easily manipulated with linear optics. These features are required for communication applications, especially in quantum-cryptography, where the photons must travel over long channels. However, the security of the communication will depend on the condition that only *one* photon is assigned to one qubit (more than one photon would allow an eventual eavesdropper to gain information). Some cryptographic protocols also require indistinguishable photons [2] or entangled photon pairs [3,4].

## 2.1. Ideal Single-Photon Source

For encoded data transfer or any other quantum-information treatment it is highly important to have a source, which is able to emit single photons at any arbitrary time defined by user, i.e. single photons "on demand". The ideal single photon emitter (SPE) is characterized by 100% probability of triggered photon emission, and no multi-photon emission can occur. The subsequent photons must

be indistinguishable and the repetition rate of the photon generation should be arbitrarily fast, though it is limited by the temporal duration of the single photon pulses.

In the real world one observes deviations from the ideal case: the single photon emission can be lost due to decoherence of the source. The quantum efficiency does not reach the 100% because of the internal absorption or reflection effects in the SPE environment. The emission efficiency (the extraction of emitted photons) is even lower for the same reasons. Finally, multi-photon emission can occur, if the repetition period of the single-photon emission is much shorter than the duration of the excitation pulse. However, for quantum-information technologies it is sufficient to operate with SPE which permit encoding, transfer and decoding the information with relatively low loses (i.e. the message is understandable) [3].

There are various examples of real quantum-mechanical systems that can serve as SPE: single atoms [5], single ions [6], single molecules [7], color centers [8], and quantum dots (QDs) [9]. Though, the single photon emission is achieved in a different manner in the mentioned systems, the description of the photon production process can be ideally described by a two-level system (see Figure 2.1). When a single photon is demanded, an external source of energy controlled by the user puts the quantum system in the excited state $|e\rangle$, where it lasts during a finite time (life time $\tau_0$) until it relaxes to the ground state. The relaxation occurs via radiative recombination producing the desired photon emission. Only one photon can be emitted at a time, since the excited state remains empty until the next excitation, which also takes time. Note that this situation cannot occur in systems with dimensions higher than 0, where a continuum of higher excited states acts as a reservoir to refill $|e\rangle$ in few picoseconds. In consequence, the emitter can produce photons one-by-one, what is evidenced in anti-bunching of photons. More detailed information about photon anti-bunching can be found in chapter §3.4.

## 2.2. Semiconductor Quantum Dots

Semiconductor quantum dots QDs are among the most promising single-photon emitters for quantum information applications due to their versatility, scalability, and ease to handle, as compared to atom or ion-based SPEs. However, the use of semiconductor QDs as true “on demand” [10] SPEs is conditioned by the presence of “background photons” photons emitted outside the QD but at the QD energy, and decoherence.

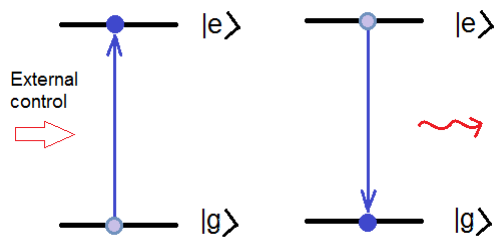


Figure 2.1 Illustration of a single photon emitter (SPE) system in: (*left*) excited state after excitation, (*right*) ground state after exciton recombination.

The most common method for semiconductor QD growth is the molecular beam epitaxy (MBE) or metal organic chemical vapor deposition (MOCVD). Semiconductor QDs grown by these methods are spontaneously formed on the interface between two semiconductors with different band-gaps ($E_g$) due to the mismatch of the crystal lattice constant. This self-assembling of the nano-metric islands of one semiconductor on the surface of the other one was predicted theoretically by Stranski and Krastanow in 1938 [11]. The first successfully demonstrated self-organized QD grown by MBE was reported in 1990 by Mo et al. [12] and Yao et al. [13], and by MOCVD was reported four years later by Carlsson et al., [14] and Notzel et al [15].

As mentioned above, the self-assembled semiconductor QD has a form of an island of energy gap $E_g$ embedded in a semiconductor crystal with grater energy $E_g$. The difference in the energy band-gap in both materials produces a band offset and the formation of a potential well in all three space directions ***xyz*** (so called quantum box or quantum dot). Typical bulk semiconductors have parabolic band and the carriers can propagate in all directions across the crystal lattice. However, a reduction of the material thickness in one or more directions will result in the quantization of energy levels and density of states. The illustration of the three-dimensional confinement in QD, compared with semiconductor bulk band structure and the confinement of a 2D semiconductor quantum well, is shown in Figure 2.2 (after Ref. [16]).

The quantum confinement is reached when the system size is comparable to the de Broglie wavelength ($\lambda_B$) of the carriers. Since the effective mass ($m_{eff}$) of the carriers in a solid (both for electrons and holes) is much smaller than the mass of free carriers ($m_0$), the effects of the quantization can be observed even for layer thickness up to 100 times greater than the lattice constant (contrary to metals, where $\lambda_B$ is of the order of the lattice spacing).

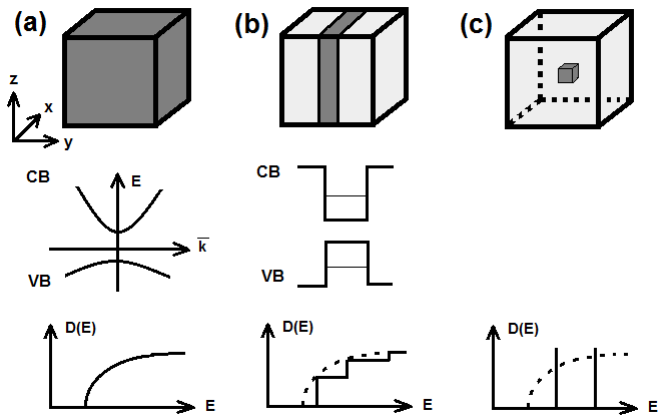


Figure 2.2 Illustration of the electronic state nature in (a) bulk semiconductor (3D), (b) quantum well (2D), and (c) quantum dot (0D). (*Top row*) schematic morphology; (*center row*) electronic structure, (*bottom row*) density of states. After Ref. [16].

The energy level of a semiconductor QD can be understood starting from the band structure of a bulk semiconductor. Figure 2.3 (a) shows a sketch of a typical 3D semiconductor band-structure around the Γ point (***k*** = 0). For small ***k*** the bands follow with good approximation the parabolic energy dispersion (E(***k***)) and the carrier motion can be well described in terms of an effective mass ($m_{eff}$). For the conduction band (CB) the part of the Bloch wave-function related to the lattice periodicity exhibits s-type symmetry with angular momentum L = 0. The total angular momentum ***j*** = L+½ and its projection in the ***z*** direction $j_z$ take values $(j, j_z) = (\frac{1}{2}, \pm\frac{1}{2})$, resulting in two-fold spin-degeneracy of the CB states. The valence band (VB) states have p-type symmetry with L=1 at ***k***=0. The total angular momentum and its projection in ***z*** direction are: $(j, j_z) = (\frac{3}{2}, \pm\frac{3}{2}), (\frac{3}{2}, \pm\frac{1}{2})$ and $(\frac{1}{2}, \pm\frac{1}{2})$. Hence, the VB states are six-fold degenerate. The spin-orbit interaction (strong in semiconductor of the II-IV and II-V group) leads to a splitting of the $j = \frac{3}{2}$ and $j = \frac{1}{2}$ states into two separate bands, and the $j = \frac{1}{2}$ states are shifted by spin-orbit energy $E_{SO}$ to lower energy values. The upper valence band states with $j = \frac{3}{2}$ are four-fold degenerate at ***k*** = 0. The different values of the ***z*** projection of the total angular momentum for these states ( $j_z = \pm\frac{3}{2}$ and $j_z = \pm\frac{1}{2}$) originates separation of the upper VB into two sub-bands at $\boldsymbol{k} \neq 0$ with different effective masses. The upper-VBs with $j_z = \pm\frac{3}{2}$ and $j_z = \pm\frac{1}{2}$ correspond to the *heavy*- (hh) and *light-hole* (lh) sub-bands, respectively, each with two-fold spin-degeneration of states.

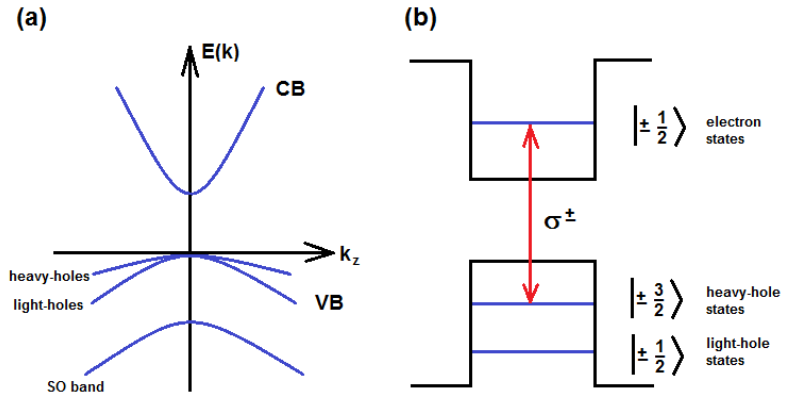


Figure 2.3 (a) Band structure in semiconductor bulk. (b) Single-particle energy levels in QD. The arrow represents the circularly polarized ($\sigma^{\pm}$) optical transition.

The tree-dimensional confinement of a QD leads to formation of single-particle levels. They result from the quantization of the allowed values of $\boldsymbol{k}_i$ (i=***x***,***y***,***z***) to integer multiples of $\pi/d$. The confined states can be understood as standing-wave-like wave-functions in the confining potential. The CB ground state is formed by two degenerate states $|\pm\frac{1}{2}\rangle$. In the first approximation the heavy- and light-hole are no longer degenerate at $\mathbf{k}_i=0$ [17,18], and the VB ground state consists of the two-fold degenerate heave-hole states $|\pm\frac{3}{2}\rangle$, and the light-holes states $|\pm\frac{1}{2}\rangle$ are split-off by several meV due to their much smaller $m_{eff}$. Optical transitions between the CB and VB states must obey selection rules, since the photon total angular momentum is $|\pm 1\rangle$. In consequence, absorption or emission between electron states and heavy-hole states with angular momentum $|\pm\frac{3}{2}\rangle$ occur only via circularly polarized photons ($\sigma^{\pm}$) respectively. However, these selection rules are often partially violated due to the light-heavy hole state mixing.

In case of an undoped QD in the neutral ground state $|g\rangle$ all the valence band states are filled and all conduction band states are empty. The QD is than in its neutral, ground state $|g\rangle$. When an electron from the VB is excited by an external means across the band-gap to the CB, it leaves a hole in the VB. The system passes from the ground to the excited state $|e\rangle$. The *e-h* pair can be formed directly inside the QD confining potential well, if the excitation energy is equal to the energy difference between the energy levels $(\Delta E = E_e - E_h)$ in the QD. This is so called *resonant* excitation (see Figure 2.4 (a)). For excitation above the band-gap of the QD barrier (i.e. *off-resonant* excitation) both carries are excited to the

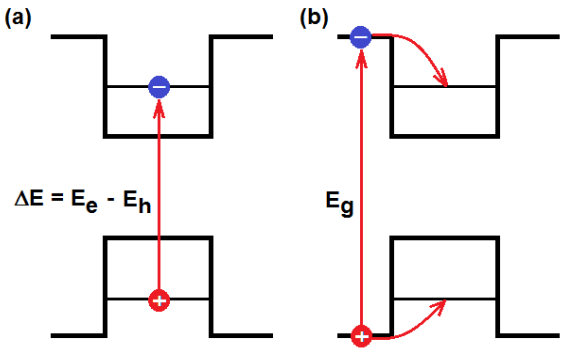


Figure 2.4 Exciton formations in QD for (a) resonant and (b) off-resonant excitation.

continuum states of the QD barriers in the CB and VB. Then they can be trapped by the QD potential via phonon assisted relaxation process (see Figure 2.4 (b)). The excitonic states can be created by optical or electrical excitation. The first consists of absorption of a photon with energy $h\nu$ at least equal to the ΔE. The second is produced by injecting the carriers (electron and hole) into the QD by external electric field [19].

Due to spatial confinement and Coulomb interaction between the carriers, the *e-h* pair forms a quasi-particle, called *exciton*. The nature and optical properties of the excitons in semiconductor QD will be discussed in the next section.

## 2.3. Excitons confined in a Quantum Dot

When the QD ground states of the electrons and holes are populated by one carrier each, they form a neutral exciton (X). In contrast to the bulk semiconductor, where X is stabilized only by Coulomb attraction and can decay rapidly (~ few ps), the QD confining potential and the Coulomb interaction between the *e-h* pair make the X state stable and long-lived (~1 ns) [16].

The lowest energy state of the exciton is four-fold degenerate, since it is a combination of the electron $|\pm\tfrac{1}{2}\rangle$ and heavy-hole $|\pm\tfrac{3}{2}\rangle$ states:

$$\begin{aligned} |X_{\sigma^-}\rangle &= |+\tfrac{1}{2}\uparrow -\tfrac{3}{2}\Downarrow\rangle = |-1\rangle \\ |X_{\sigma^+}\rangle &= |-\tfrac{1}{2}\downarrow +\tfrac{3}{2}\Uparrow\rangle = |+1\rangle \\ |DX_{-}\rangle &= |-\tfrac{1}{2}\downarrow -\tfrac{3}{2}\Downarrow\rangle = |-2\rangle \\ |DX_{+}\rangle &= |+\tfrac{1}{2}\uparrow +\tfrac{3}{2}\Uparrow\rangle = |+2\rangle \end{aligned} \quad . \qquad (2.1)$$

The arrows (↑ and ⇓) represent spin-sign of the electron and hole, respectively. Two of the states are optically allowed for their total angular momenta ±1. These are *bright excitons* (BX) as they can decay optically to the ground state emitting one circularly-polarized photon ($\sigma^{\pm}$). The other two states (total angular momenta ±2) are optically forbidden, and they are denominated as *dark exciton* (DX) states.

The four-fold degeneracy of the lowest exciton states occurs only in the single-particle picture of ideal-QD states. However, in a real semiconductor QD there are many factors that can provoke the degeneracy lifting and state mixing (i.e. asymmetry in the shape, strain in the crystal lattice, or exchange interaction between the carries). The exchange interaction between the *e-h* pair couples their spin producing *fine structure* of the X state [20]. The exchange energy is sensitive to the symmetry of the crystal lattice and to the shape of the envelope part of the exciton wave function. So, the asymmetry and strain introduced to the QD due to the lattice mismatch of the underlying substrate produces splitting of the bright and dark states. It also lifts the degeneracy of the dark states by mixing them into nonradiative *singlets*, so the mixed dark states are formed by symmetric $|DX_{+}\rangle$ and anti-symmetric $|DX_{-}\rangle$ combinations of the $|\pm 2\rangle$ states:

$$|DX_{\pm}\rangle = \frac{1}{\sqrt{2}}\left(|+2\rangle \pm |-2\rangle\right). \tag{2.2}$$

The exchange interaction introduces also a dark-bright energy splitting ($\Delta_{DB}$) which is typically of order of few hundreds of μeV. In small self-assembled InP QDs values of 1÷5 meV have been reported [21].

If the QD has a highly asymmetric shape, which breaks the symmetry in the confinement potential, than the reduction of the point-group symmetry[1] in the plane of the quantum well will affect the envelope part of the exciton wave function. Thus, the bright exciton states will also suffer the state-mixing and splitting of the radiative doublet $|\pm 1\rangle$ into two linearly polarized, orthogonal states:

$$|X_{x,y}\rangle = \frac{1}{\sqrt{2}}\left(|+1\rangle \pm |-1\rangle\right). \tag{2.3}$$

The splitting in energy appearing for the mixed bright states is analogue to the one observed for the dark states mixture. This *fine structure splitting* ($\Delta_{FSS}$) is typically

[1] In the zinc-blend the point-group symmetry is $D_{2d}$.

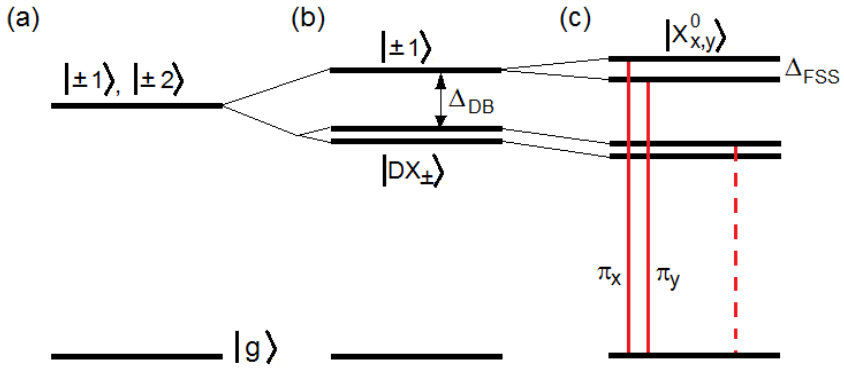


Figure 2.5 Level schemes for X state: (a) four-fold degeneration of the exciton state in absence of the exchange interaction, (b) fine structure splitting of bright and dark states and state mixing due to exchange interaction, (c) further fine structure splitting and state mixing due to the broken in-plane symmetry of the QD. The solid (dashed) lines represent transition optically permitted (prohibited) by selection rules.

of order of few tens to few hundreds of μeV, depending on the composition, shape and size of a particular QD [20,22]. The *x* and *y* sub-indices in Eq. (2.3) represent the orthogonal directions in the QD plane. The dipole moments associated to the $|X_i\rangle$ states ($i$=$x$,$y$), are oriented along the main crystallographic axes of the QD. Consequently, the optical transition from the $|X_i\rangle$ to $|g\rangle$ state produces two emission lines, linearly polarized ($\pi_x$ and $\pi_y$) and split by $\Delta_{FSS}$. The scheme of the X levels is shown in Figure 2.5.

When the single-particle ground states for electrons and holes (s-shell) are filled by two carriers each than a *biexciton* (XX) is formed in a QD. Contrary to a bulk crystal, where XX can dissociate into two spatially separate excitons, the QD potential does not allow the creation of two independent excitons, as a single exciton is not an eigenstate of the four-particle Hamiltonian [16]. The spatial confinement of the QD potential maintains the carriers localized. A rather complicated Coulomb interaction between the four carriers gives rise to a difference between the XX energy and the energy of two excitons: $E_{XX}^b = 2E_X - E_{XX}$. The biexciton binding energy ($E_{XX}^b$) can be observed experimentally in the luminescence spectrum, as the XX energy is usually red-shifted by $E_{XX}^b$ (~ few meV) from the X emission line. Thus, the QD excited to a biexcitonic state can emit two photons of different energies. The first is emitted in the recombination of the first e-h pair from XX to X state. The second is emitted from the X to ground state, resulting in a cascade emission. The relative position of the XX and X

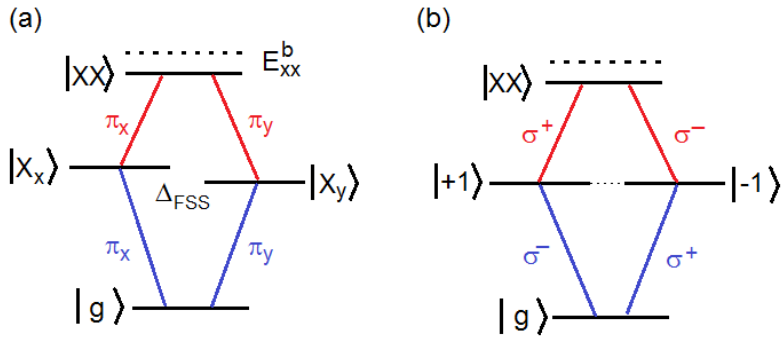


Figure 2.6 Level scheme for XX state: (a) the decay from XX to Xx,y originates fine structure splitting in the XX emission energy. (b) In case of $\Delta_{FSS}=0$ the XX→ X→ G emission cascade can provide entangled photon pairs.

emission lines observed in the luminescence spectrum depends on two factors: i) Coulomb interaction which depends on relative shape and size of excitonic wave function, and ii) correlation effect between the electron and hole levels [23] related to a number of confined states within the dot. The first one will blue-shit the XX transition energy above the X energy (anti-binding). The second will depend on the QD size and the number of bound states. Increasing the QD size red-shifts the XX energy below the X emission line (binding). Combination of both effects leads to transition from a binding ($E_{XX}<E_X$) to anti-binding ($E_{XX}>E_X$) limit while the QD decreases [24].

As the biexciton is formed by two electrons and two holes in the s-shell the spin is compensated and the biexciton is spin-singlet state (see Figure 2.6). The recombination of one *e-h* pair leaves another pair in the dot, so the $|XX\rangle$ state decays optically to one of the split exciton states $|X_{x,y}\rangle$. In consequence, the XX emission has the same fine structure splitting as the exciton one. In case of $\Delta_{FSS}=0$, the indistinguishability of the two decay cascades XX →X →G can lead to entanglement of emitted photon pairs. (see Figure 2.6). The entanglement of the photon pairs emitted from a semiconductor QD was experimentally observed in InAs QDs [4].

In presence of an additional carrier in a QD ground state, the energy of a photo-created or injected *e-h* pair confined in the QD will change due to the Coulomb interaction. The ground state of a negatively (positively) charged QD with total angular momentum j=$\frac{1}{2}$ (j=$\frac{3}{2}$) is doubly degenerated. The excited state of the charged QD, designated as *trion*, is formed by three carriers: i) two electrons

and one hole (2*e*-*h*) or ii) one electron and two holes (*e*-2*h*). As two carriers in the same spin-singlet state do not experience the exchange interaction the negatively ($X^{1-}$) or positively ($X^{+1}$) charged excitons have no fine structure splitting and thus decay optically to the charged ground $|g^{\pm}\rangle$ state producing unpolarized emission lines in the luminescence spectrum.

For high enough excitation power a charged QD in the ground state can be filled by two *e*-*h* pair leading to formation of charged biexciton state $XX^{1\pm}$. Extra doping or carrier injection will increase the charge level of the exciton ($X^{2\pm}$, $X^{3\pm}$, etc.).

# References


[1] *see for instance:* Michael A. Nielsen, Isaac L. Chuang, "*Quantum computation and quantum information*", Cambridge University Press (2000)

[2] C. Santori, D. Fattal, J. Vuckovic, G. S. Solomon, & Y. Yamamoto, Nature 419, 594–597(2002).

[3] D. F. V. James, P. G. Kwiat, W. J. Munro and A. G. White, PHYS. REV. A, 64, 052312 (2001).

[4] *see for instance* R. M. Stevenson et al. Nature (2006),

[5] H. J. Kimble, M. Dagenais, L. Mandel, Phys. Rev. Lett. 39, pp. 691-694 (1977)

[6] F. Diedrich and H. Walther, Phys. Rev. Lett. 58, pp. 203-206 (1987)

[7] Th. Basché,W. E. Morener, M. Orrit, H. Talon, Phys. Rev. Lett. 69, pp. 1516-1519 (1992)

[8] R. Brouri, A. Beveratos, J.-P. Poizat, and P. Grangier, Opt. Lett. Vol. 25, No. 17, p. 1294 (2000).

[9] P. Michler, A. Imamoglu, M. D. Mason, P. J. Carson, G. F. Strouse, and S. K. Buratto, Nature (London) 406, 268 (2000).

[10] P. Michler, A. Kiraz, C. Becher, W. V. Shoenfeld, P. M. Petroff, L. Zhang, E. Hu, and A. Imamoglu, Science 290, 2282 (2000).

[11] I.N. Stranski and L. Krastanow, Sitzungsber. Akad. Wiss. Wien, Math.-Naturwiss. Kl., Abt. 2B 146, 797 (1938)

[12] Y.-W. Mo, B. S. Swartzentruber, R. Kariotis, M. B. Webb, and M. G. Lagally, Phys. Rev. Lett. 63, 2393–2396 (1989).

[13] J. Y. Yao, T. G. Andersson, and G. L. Dunlop, J. Appl. Phys. 69, 2224 (1991).

[14] N. Carlsson, W. Seifert, A. Petersson, P. Castrillo, M. E. Pistol, and L. Samuelson, Appl. Phys. Lett. 65, 3093 (1994).

[15] R. Notzel, Semicond. Sci. Technol. 11, 1365 (1996).

[16] D. Bimberg, M. Grundmann, N. N. Ledenstov, "Quantum Dot Heterostructures", Jonhm Wiley & Sons (2001)

[17] E. Blackwood, M. J. Snelling, R. T. Barley S. R. Andrews C. T. B. Foxon, Phys. Rev. B 50, 14246 (1994)

[18] L. Besombes, K. Kheng, and D. Martrou Phys. Rev. Lett. 85, N2, pp.425-428 (2000).

[19] N. A. J. M. Kleemans, J. van Bree, A. O. Govorov, J. G. Keizer, G. J. Hamhuis, R. Nötzel, A. Yu. Silov & P. M. Koenraad, Nature Physics 6, 534–538 (2010)

[20] M. Bayer, G. Ortner, O. Stern, A. Kuther, A. A. Gorbunov, and A. Forchel, P. Hawrylak, S. Fafard, and K. Hinzer, T. L. Reinecke and S. N. Walck, J. P. Reithmaier, F. Klopf, and F. Scha¨fer, Phys. Rev. B, 65, 195315 (2001).

[21] M. Reischle, G. J. Beirne, R. Roßbach, M. Jetter, and P. Michler, Phys. Rev. Lett. 101, 146402 (2008).

[22] S. Rodt, A. Schliwa, K. Pötschke, F. Guffarth, and D. Bimberg, Phys. Rev. B 71, 155325 (2005).

[23] G.A. Narvaez, G. Bester, and A. Zunger, Phys. Rev. B 72, 245318 (2005).

[24] D. Sarkar, H.P. van der Meulen, J.M. Calleja, J.M. Becker, R.J. Haug, and K. Pierz, J. Appl. Phys. **100**, 023109 (2006)

# Chapter 3

# Experimental Techniques

Optical and electrical properties of semiconductor structures can be studied by different types of spectroscopy. In this chapter the experimental the methods of spectroscopy used in this thesis will de described. For the QD emission characterization the micro-photoluminescence technique (micro-PL) was used. The dynamics of the QD optical transitions were studied with Time-Resolved PL (TRPL). The PL excitation (PLE) measurements were run to study the QD excited states. Finally, the single photon emission was studied in the Time-Correlated Single-Photon Counting (TCSPC) experiment.

## 3.1. Photoluminescence spectroscopy

The photon emission process after previous energy absorption is called *luminescence*, and is widely used for semiconductor QDs characterization. In the luminescence experiment a nonequilibrium distribution of electron – hole (*e-h*) pairs is initially excited by some external means. Then the *e-h* pairs thermalize and reach a quasi-thermal equilibrium. In the final step the radiative recombination of the *e-h* pairs occurs and photons are emitted [1].

There are many types of luminescence depending on the carrier-excitation method. In *electroluminescence* the carriers are injected via an external current. Light emission induced by electron bombardment is known as *cathodoluminescence*, and the carrier thermal excitation by sample heating is called *thermoluminescence*. The semiconductor samples studied in this thesis were excited optically. In this technique photons of energy higher than the band gap are absorbed, promoting electrons from the valence band to the conduction band and

living holes in the valence band. After relaxation the electrons recombine with the holes. This type of luminescence is called *photoluminescence* (PL).

The basic principle of the photoluminescence process in semiconductors is shown in Figure 3.1. In a perfect semiconductor crystal the *e-h* pairs thermalize in the time scale of picoseconds and accumulate at the conduction (CB) and valence (VB) band extrema, and then recombine (Figure 3.1 (a)). This process is called *band-to-band* transition and the energy of the emitted photon corresponds to the direct band-gap energy ($E_g$), except for excitonic corrections. However, in semiconductor QDs the energy levels in the CB and VB are quantized and the emitted photon energies correspond to the energies of the discrete states of the QD (Figure 3.1 (b)). These transitions can be observed in a luminescence spectroscopy experiment by collection of the emitted light and its spectral analysis.

*Micro-PL experimental set-up*

A sketch of the PL set-up is shown in Figure 3.2. The samples are optically excited with a laser light, whose frequency is chosen depending on the sample band gap and the character of the excitation: (i) off-resonant above WL or (ii) quasi-resonant into one of the QD excited states. In this thesis continuous Ar (2.4 eV) and HeNe (1.95 eV) lasers were used for the optical excitation of the InP QDs above WL (1.93 eV). A tunable DCM[1] dye laser (1.86 eV ÷ 1.95 eV) was utilized for the quasi-resonant excitation. The laser beam was filtered with a prism monochromator to eliminate the background emission (dye laser) or to remove plasma lines (gas lasers). More detailed information about lasers used in the photoluminescence experiment can be found in Table 3.1.

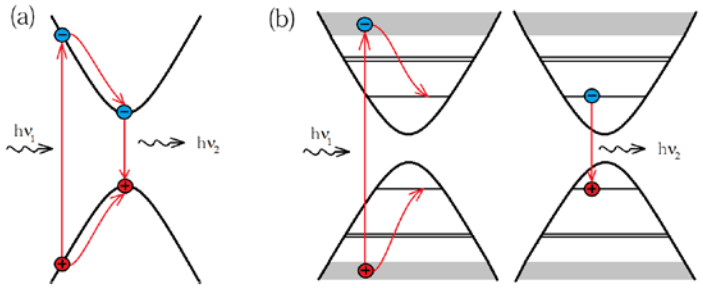


Figure 3.1 Principle of photoluminescence. (a) Formation of an electron-hole pair in bulk semiconductor after photon absorption. The thermalization of the carriers precedes the radiative recombination. (b) Carrier excitation in the QD and non-radiative relaxation into the ground states. The radiative recombination produces the emitted photon.

[1] DCM – 4-dicyanomethylene-2-methyl-6-p-dimethylaminostyryl-4H-pyran

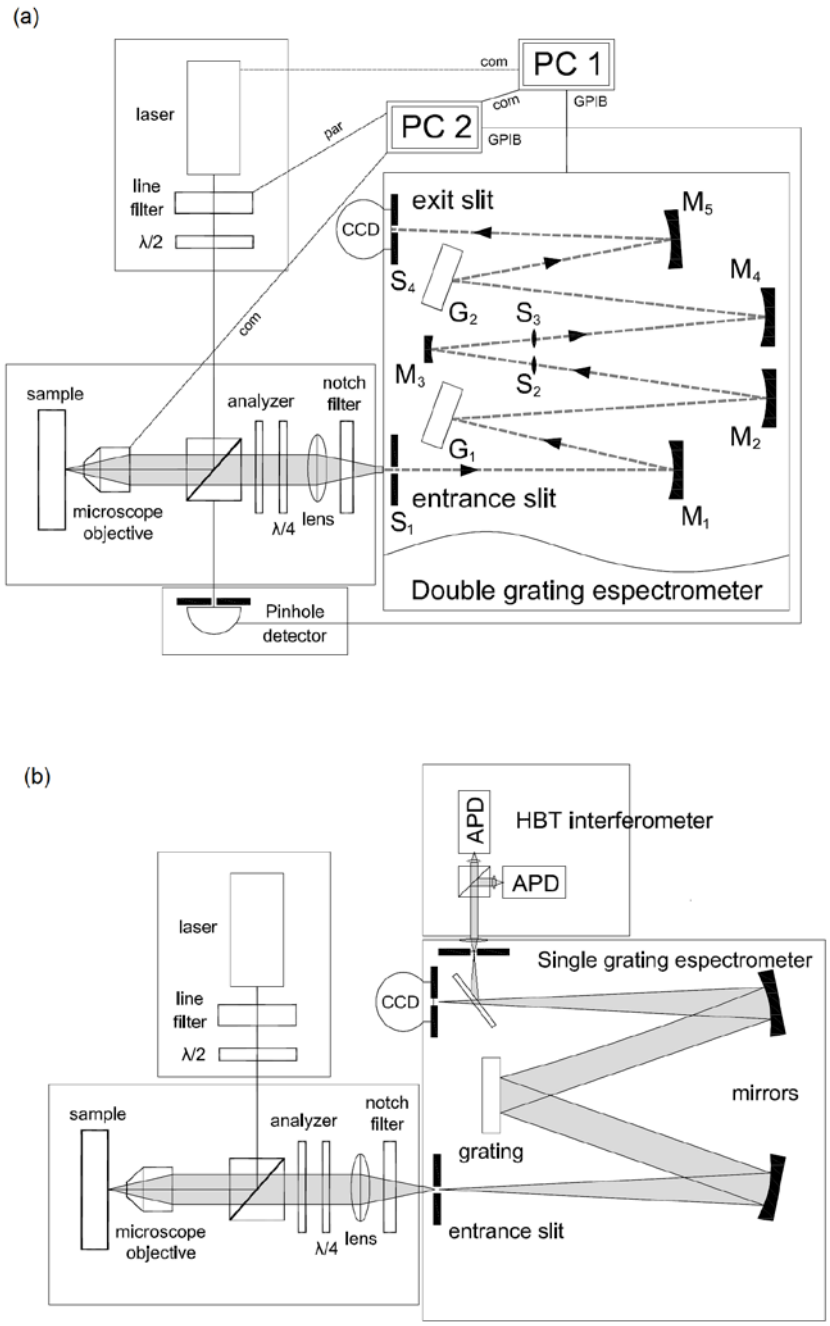


Figure 3.2 Micro-PL experimental set-ups: (a) Double spectrometer for micro-PL and micro-PLE, (b) Single spectrometer for micro-PL and HBT.

**Table 3.1** Details of the lasers used for the optical excitation.

| Laser | | Emission wavelengths |
|---|---|---|
| $Ar^+$ | Spectra-Physics Beamlok 2060 | 457.9 and 514.5 nm (cw) |
| HeNe | Melles Griot 25-LHP-928-230 | 632.8 nm (cw) |
| Dye laser | Spectra-Physics 375 B (DCM dye) | 633-660 nm (cw) |
| Ti: Sapphire | Spectra Physics Tsunami pumped with CW diode laser SP Millenia | 640 nm (pulsed), pulse width 1.5 ps, repetition rate 82.1 MHZ |

**Table 3.2** Specification of the optical components used in the experiments

| Beamsplitters | | Specifications |
|---|---|---|
| Broadband Non-Polarizing Cube | Newport | 400-700 nm; T=45±5%, R=45±5%, |
| Dichroic mirror | Semrock | Tr = 0.05% at 633 nm (45º incidence angle) |
| Dichroic mirror | Semrock | Tr = 0.0% at 635 nm (45º incidence angle) |
| Other Optical Components | | Specifications |
| Microscope Objectives | Nikon | A=50×, NA=0.55, Ø < 1.5 μm, WD 4.7 mm, $\theta_{air}$=33º, $\theta_{InP}$=10º<br>A=100×, NA=0.73, Ø < 1.0 μm, WD 8.7 mm, $\theta_{air}$=47º, $\theta_{InP}$=13º |
| Mirrors | Semrock | R = 99% |
| Linear Polarizer | Newport | VIS 430-670 nm |
| Half Wave Plates (λ/2) | Newport | achromatic, zero order, VIS 400-700 nm |
| Quarter Wave Plates (λ/4) | Newport | achromatic, zero order, VIS 400-700 nm |
| Razor Edge Filters | Kaiser | super notch at 514.4 nm<br>super notch at 632.8 nm |

Amplification (A), Numerical Aperture (NA), spot size (Ø), Reflectivity (R), Working Distance (WD), Collection Angle (θ)

**Table 3.3** Details of the spectrometers and detectors used in micro-PL measurements.

| Charged coupled device (CCD) | | Specifications |
|---|---|---|
| Jobin Ybon CCD-3000 (V) (single spectrometer)<br>Jobin Ybon SpectraView-2D (double spectrometer) | | UV-NIR, pixel size 26 μm<br>VIS-NIR, pixel size 27 μm |
| Spectrometer | Focal length *f*, Numerical aperture (NA) | Gratings, Resolution (res) |
| Spex 750 | *f* = 75 cm, NA = *f* / 6 | 1200* grooves/mm, res = 0.01 nm |
| Spex 1404 | *f* = 85 cm, NA = *f* /7.8 | 1800 grooves/mm, res=0.005 nm |

* Holographic grating

To minimize non-radiative recombination, the samples were studied at low temperatures. For that purpose the samples were placed inside the vacuum chamber of a cryostat (Konti-Cryostat-Mikro from *CryoVac*) and cooled down with liquid helium. The cryostat is equipped with a temperature sensor (Si-diode DT670A), a heater and a temperature controller (TIC 304-MA). Before cooling the cryostat was evacuated with a turbo pump down to $1\times10^{-4}$ Pa. As the samples are not in direct contact with the He gas, they are glued with silver paint to a cooper "cold finger" to ensure good thermal conductivity. The measurements presented in this thesis were run at low temperatures in the range between 6 K and 70 K.

In order to limit the excitation region of the sample to a small area, the PL spectra were measured through a microscope objective, which is used to focus the laser beam on the sample surface and to collect the PL signal. The high numerical aperture (NA) of the objective permits focusing of the laser beam to a diffraction limited spot of around 1 micrometer in diameter ($Ø=2\lambda/(\pi NA)$). Simultaneously, the microscope objective allows collecting the PL signal with the widest angle ($\theta$) possible (see Table 3.2). This configuration increases significantly the efficiency of the light collection.

As the laser beam and the PL emission propagate in the same direction, a dichroic mirror acting as a beamsplitter must be placed before the microscope objective. The dichroic mirror separates spectrally the PL signal from the optical excitation. This allows reflecting up to 90% of the laser light while almost 100% of the signal collected by the microscope objective can pass through the beamsplitter. More details about the dichroic mirror used in this thesis can be found in the Table 3.2.

The microscope objective is mounted on a computer-controlled three axes DC-motor stage. This allows a fine adjustment of the objective position above the sample. The step size of the motor stage is 13 nm. However, the spatial resolution is limited by the laser spot size. In our case it corresponds to one third of the laser wavelength, which is equivalent to 20 steps. The cryostat was mounted horizontally on a XYZ translation stage to access the different regions of the samples without changing the optical alignment. The horizontal position of the cryostat together with the optic table stabilizer (NewPort, I-2000 Series) guaranteed a good mechanical stability (up to 2 hours in optimal external conditions).

As the extraction efficiency of the emitted light from the samples is low (due to the high refraction index of the sample, together with absorption and scattering losses), high reflectance silver mirrors were used for the PL collection. Notch filters or long wave pass filters placed in front of the spectrometer entrance slit

serve to cut off the laser background. The PL signal is focused by a lens on the entrance slit of the spectrometer. To optimize both spectral resolution and throughput this lens is matched with the numerical aperture of the spectrometer.

Detection is done with a spectrometer and a charge coupled device (CCD) detector, both controlled by a PC. The CCD is cooled with liquid nitrogen to about 140 K in order to reduce the background noise. Two spectrometers were used in the PL experiments with different focal lengths *f* and diffraction gratings: (i) A double spectrometer with *f* = 85 cm and gratings with 1800 grooves/mm, and (ii) A single spectrometer with *f* = 75 cm and a holographic grating of 1200 grooves/mm. As the diffraction gratings efficiency depends on the linear polarization of the light, it was necessary to use a quarter-wave plate ($\lambda/4$) at 45º in front of the spectrometer entrance slit to convert the linearly polarized light into circularly polarized.

The detailed information about all the components used in the *micro*-PL set-up can be found in Tables 3.2 and 3.3.

## 3.2. Photoluminescence Excitation

In PL measurements one obtains the emission spectrum, which gives information mainly on the lowest energy radiative transitions in the sample. However, it does not allow for the direct observation of excited states. These can be observed in absorption or reflectance experiments. However, most of the semiconductor structures, including our QDs samples, are grown on opaque substrates, and absorption cannot be measured. Reflectance measurements have not this drawback, but they rely very critically on the surface state and usually lack of good spatial resolution. The easiest way to access excited states in this case is to use PL excitation (PLE).

A PLE experiment consists on measuring the PL intensity at particular photon energy ($E_{PL}$) as a function of the excitation energy ($E_{exct}$). In this technique the spectrometer is set to detect the selected wavelength (normally at the emission maximum), and the PL intensity is recorded as a function of $E_{exct}$. This method is equivalent in good approximation to an absorption measurement.

*PLE experimental set-up*

PLE measurements were performed automatically using a computer controlled feedback system to synchronize the tunable dye laser and a prism monochromator which eliminates the dye background emission (see Figure 3.2 (a)). The laser was tuned in the energy range 1.87 eV to 1.95 eV and the monochromator was adjusted synchronously. For that purpose a stepper motor installed in the prism

monochromator and an optical power meter with a pinhole in front were used to reproduce the light path for every exciting wavelength. This was done by maximizing the intensity of the laser light trough the pinhole. The control of the set-up was performed by two PC: One for the spectrometer and CCD control, and a second one for the prism monochromator and power meter control.

The automatic acquisition of PLE spectra starts with the manual alignment of the set-up. The laser frequency is set before each new acquisition and the prism monochromator position is automatically adjusted by maximizing the laser intensity at the power meter. As the power meter and the pinhole are placed behind the unused beamsplitter output in the microscope set-up, and the distance from the beamsplitter is large, the alignment of the new laser wavelength is identical to the first one, and the laser spot hits on the same sample surface location.

*Spectral resolution of the PL and PLE spectrum*

In chapter §5.1 the high resolution record of the exciton PLE will be presented. The excitation energy steps $\Delta E_{exct}$ corresponding to the separation between the two laser frequencies (measured with the spectrometer and CCD) was estimated to be 200 μeV. The spectral resolution of the photoluminescence (PL) measurements is of the order of 8 μeV. In the Figure 3.3 this is illustrated by a blow-up of two spectra of the exciton peak of Figure 5.1. The peak position for each peak is determined by a Gaussian fit. Both PL lines are normalized to the same height and they show nearly the same width. The measured PL spectra deviate slightly from the Gaussian fits in the low energy side. There are several well known reasons for that in real QDs: (i) A small polarization leakage between the two fine-structure components, or (ii) The asymmetric broadening by acoustic phonons [2]. The PL resolution is not limited by this fact. The separation between the peaks in Fig.3.3 is 30 μeV.

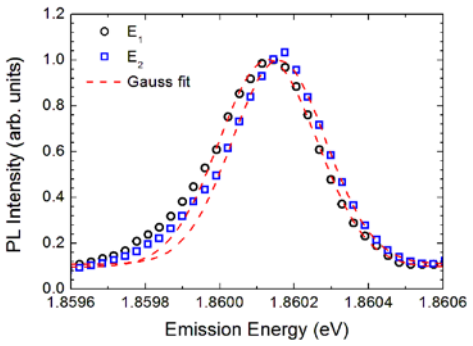


Figure 3.3 Blow-up of two spectra of the exciton peak of Figure 5.1. The peak positions are determined by a Gaussian fit.

## 3.3. Time-Resolved Photoluminescence Spectroscopy

The PL spectrum under continuous excitation gives information about the optically allowed transitions but not about the dynamics of the studied system. Instead, the emission dynamics can be recorded in time-resolved PL (TRPL) experiments, and the characteristic relaxation times of the involved excitonic states can be obtained [3].

In a TRPL experiment the emitted light intensity of a single quantum dot is recorded as a function of the time elapsed after a short light pulse excitation. For semiconductor QDs the typical PL decay lasts from a few hundred picoseconds to few nanoseconds, and the PL rise time is even shorter (~50 ps). To observe the PL time evolution of a single QD a time resolution of 20 ps or less is needed. This is hard to achieve with ordinary electronic transient recorders of reasonable dynamic range. Moreover, the PL emission may be too weak to be measured, as in the case of one photon emitted in one excitation-emission cycle. The solution for these problems is to record single photon events in many excitation-emission cycles under periodic excitation with a pulsed laser. The excitation laser pulse is the time reference for the photon detection. If the probability of registering more than one photon per laser pulse is low, one can construct a histogram of photon detection for different time delays $\tau$ (time difference between the laser pulse detection and single photon arrival to the detector). The histogram (see Figure 3.4) represents then the PL dynamic curve which one would obtain from a single measurement of a time-resolved analog recording.

To guarantee that the histogram represents precisely the PL decay, the probability of multi photon detection must remain low. This is ensured by the *dead time*[2] of the photo-detectors, which is much longer than the duration of the laser pulse. Typically the laser pulse duration is of order of few picoseconds, while the dead time of the detectors (avalanche photodiodes or APD) is of the order of 50 ns. So in case of two or more photons emitted in the same excitation cycle only the first one will be recorded. That may introduce a distortion in the PL decay profile (the decay time seems to be shorter than it really is) as the early photons will be recorded in first place. Thus, it is of high importance to keep the probability of multiple photon emission low.

The single photon detection can be achieved by using fast photon counting detectors with high detection efficiency. Usually, for TRPL measurements one uses an APD or a streak camera, both synchronized with the laser pulses by a trigger

[2] *Dead time* – the time interval in which the detector cannot register photons while it is processing a previous photon event.

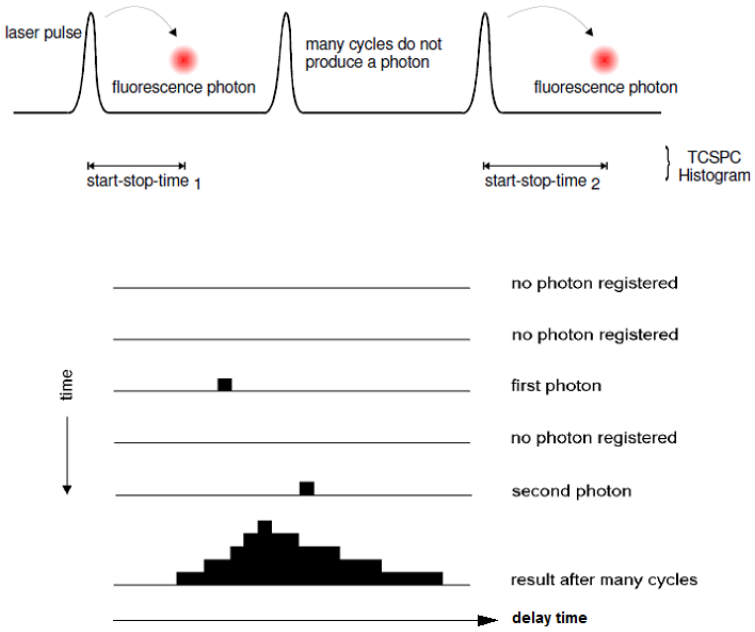


Figure 3.4 Basic principle of the time correlated single photon counting method and histogram construction. After Ref. [3].

unit. The laser pulse must be short enough to create few or only one exciton per pulse. For the TRPL measurements presented in this work a pulsed Ti:$Al_2O_3$ laser was used. The pulse width was 1.5 ps and the repetition rate was 82.1 MHz. More detailed information about the pulsed laser can be found in the Table 3.1.

*Streak camera*

Ultra-fast PL processes can be measured with a streak camera (Figure 3.5) which combines the spectral imaging with the temporal evolution of the emitted light [4]. The light (previously dispersed in a spectrometer) is projected on the photocathode (1) of the streak tube. The photons are converted into electrons, whose total number depends on the intensity of the incident light. The horizontal position of the electrons inside the tube corresponds to the spatial distribution of incident photons. The electrons pass between two electrodes (2) to which a high AC voltage is applied with a frequency controlled by the external trigger. The AC voltage swaps the electrons from top to bottom depending on their arrival time. The carriers are deflected at different times and at different horizontal positions. Then the carriers impinge into a micro-channel plate (3) where they are multiplied with a high gain. The electron beam resolved in 2D hits a phosphor screen (4) and converts again into photons. The light intensity is registered in a 2D matrix: (i)

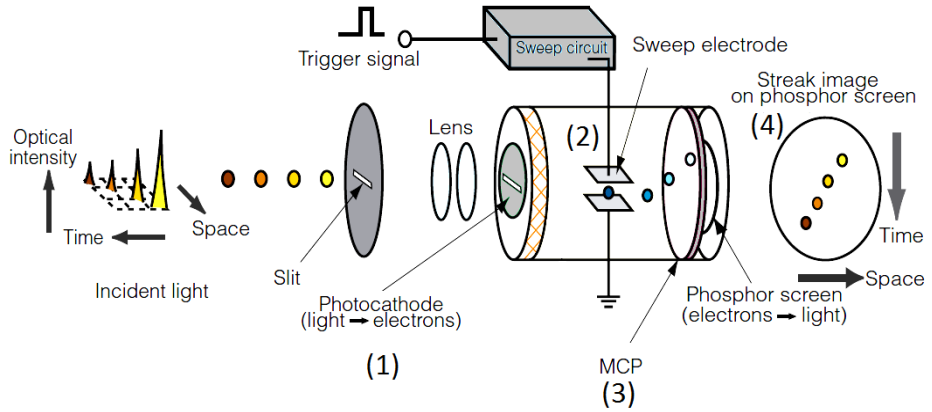


Figure 3.5 Simple sketch of the streak camera principle. After Ref. [4].

horizontal axis corresponds to the wavelength, and (ii) vertical one represents the temporal axis.

The streak camera used in the TRPL measurements presented in this work was produced by Hamamatsu Corporation (Universal Streak Camera C5680). The technical data of the streak camera are presented in the Table 3.4.

*Avalanche Photodiode*

Detection of single photons requires a very sensitive and high speed detector. This requirement can be fulfilled with an avalanche photodiode (APD) of high detection efficiency. These detectors work by applying a high reverse voltage to a semiconductor p-n junction. Commercial APDs are made from Si with a band gap of 1.12 eV at room temperature, equivalent to 1100 nm wavelength. The Figure 3.6 shows a scheme of the p-n junction used in a typical APD.

Table 3.4 Technical data of the streak camera used in TRPL experiment.

| Universal Streak Camera C5680 Hamamatsu | |
|---|---|
| Main unit C5680 | time window 2100 ps, timing resolution 30 ps |
| Inter-line CCD C4742-95 | effective pixel number 756(H)×485(V) |
| Synchroscan swep unit M5675 | synchronized with Tsunami laser 82.1 MHz |

When light is absorbed by the detector, electron-hole pairs are generated in the depletion region. The electric field applied to the diode causes a drift of the carriers to the corresponding charged regions: the electrons propagate towards the $P^+$ layer whiles the holes towards the $N^-$ one. The speed of the carriers depends on the field strength and it saturates for high voltage values. However, for very high reverse voltages break-down regime is reached, and an avalanche multiplication of the photo-current takes place. In this way the APD generates a single electrical pulse for every absorbed photon.

Three different types of APDs were used in this work:

1. PerkinElmer (SPCM AQRH-16)
2. Pico Quant (τ-SPAD 50)
3. Micro Photon Devices (MPD-5CTC).

These detectors have different quantum efficiency and response time (jitter). Their technical data are listed in Table 3.5.

The APD detectors have been used for the measurement of the emission dynamics in the TRPL experiment, as well as for the single photon correlation measurements. In the second case two avalanche photodiodes are used in the Hanbury-Brown and Twiss (HBT) interferometer [5].

It is important to mention that some APD detectors emit radiation during the electron avalanche. This effect, called *breakdown flash*, can be a significant problem in a photon correlation experiment. Typically the APD breakdown flash photons are in the 700-1000 nm wavelength range [6] and may influence the single photon coincidence measurement. Nevertheless, this inconvenience can be overcome by a careful design of the experimental set-up (see §3.4).

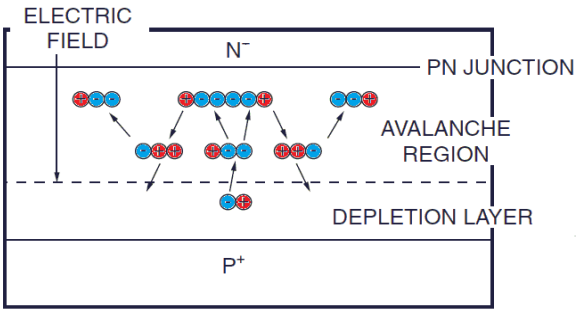


Figure 3.6 Basic principle of the avalanche photodiode (APD).

## 3.4. Single-Photon Correlation

The optical coherence of light is a fundamental issue for the study of single photons emitters, but also for any application of quantum information treatment mediated by photons. In the next sections the photon coherence of first and second order will be discussed for light sources of different origin and properties. Following, the photon correlation measurement will described as well as its application in quantum optics experiments.

### 3.4.1 First Order Coherence

In the classical theory of light, the first-order coherence properties of a light field is given by the classical first-order correlation function of the electric field *E(**z**,t)*:

$$g^{(1)}(z_1,t_1,z_2,t_2)=\frac{\langle E^*(z_1,t_1)E(z_2,t_2)\rangle}{\sqrt{\langle|E(z_1,t_1)^2|\rangle\langle|E(z_2,t_2)^2|\rangle}}, \tag{3.1}$$

which can be applied to any time-dependent light field. In the case of a stationary light field, as the one studied in this thesis, the space-time dependence reduces to the delay τ:

$$\tau=t_2-t_1=\frac{z_1-z_2}{c}, \tag{3.2}$$

where, *c* is the velocity of light in vacuum. The first order correlation function can be obtained experimentally from the visibility of the interference fringes. Depending on the degree of the coherence of the light source, $g^{(1)}(\tau)$ can take different values between 0 and 1, with the limits: $g^{(1)}(\tau)=1$ for coherent light and $g^{(1)}(\tau)=0$ for totally incoherent light. In the case of a chaotic light beam with Gaussian or Lorentzian spectrum, $g^{(1)}(\tau)$ measured in a fixed space-time point (*z*,*t*) is equal to unity ($g^{(1)}(0)=1$), as the light beam is fully correlated at the origin point. But for delays larger than the coherence time ($\tau >> \tau_c$), the light beam loses its coherence and $g^{(1)}(\tau)\rightarrow 0$. In contrary, for the classical monochromatic wave with stable amplitude and phase, $g^{(1)}(\tau)=1$ in all space-time points. More detailed information about the classical coherence of the first order can be found in Ref. [7,8].

### 3.4.2 Second-order Coherence

In first order coherence measurements one can determine the spectral purity of the light, or its coherence time $\tau_c$. However, $g^{(1)}(\tau)$ does not give the information about the statistical properties of the light. That is way the first-order correlation measurement cannot distinguish two sources of the same spectra but with different photon statistics. For that purpose one should measure the second order correlation function $g^{(2)}(\tau)$. It consists on two-time measurements in which many pairs of recorded average-intensities ($\bar{I}(t)$) are taken at fixed space-time point and for selected polarization. The average of the product of each pair is the *intensity* correlation of light and for the stationary classical light beam is defined as:

$$g^{(2)}(\tau)=\frac{\left\langle \bar{I}(t)\bar{I}(t+\tau)\right\rangle}{\bar{I}^2}=\frac{\left\langle E^*(t)E^*(t+\tau)E(t+\tau)E(t)\right\rangle}{\left\langle E^*(t)E(t)\right\rangle^2}, \tag{3.3}$$

where $\bar{I}(t)$ is the average intensity of light at instant *t*. Taking in to account that: i) $0<g^{(1)}(\tau)<1$, ii) The $g^{(2)}(\tau)$ values are controlled by Cauchy's inequality, and iii) The $g^{(2)}(\tau)$ is obtained for a large number of measurements, one obtains $g^{(2)}(0)\geq 1$ and $1<g^{(2)}(\tau)<\infty$ for the *classical* light beam (both stationary and non-stationary). Moreover, $g^{(2)}(\tau)$ cannot exceed $g^{(2)}(0)$.

There are two particular examples of light fields that can be described by classical theory, though both exhibit different properties in the second order coherence: i) The chaotic light with Gaussian or Lorenzian spectrum, which is emitted by a large number of radiating atoms (so called thermal emission). The degree of second-order coherence at zero delay is $g^{(2)}(0)=2$ while $g^{(2)}(\tau)\rightarrow 1$ for $\tau >> \tau_c$. ii) The classical wave of stable amplitude and phase (i.e. laser beam) for which the $g^{(2)}(\tau)$ function is always equal 1, regardless of the delay time.

In case of non-classical light, one should consider the *quantum* degree of the second order coherence, which is defined as:

$$g^{(2)}(\tau)=\frac{\left\langle n(n-1)\right\rangle}{\left\langle n\right\rangle^2}=1+\frac{\left(\Delta n\right)^2-\left\langle n\right\rangle}{\left\langle n^2\right\rangle}, \tag{3.4}$$

where *n* is the photon number and $\left(\Delta n\right)^2=\left\langle n\right\rangle^2+\left\langle n\right\rangle$ is the photon-number variance. Note that the *quantum* $g^{(2)}(\tau)$ is space-time independent, but it does depend on the nature of the light source, and it has different restrictions than

classical light. For instance, the quantum $g^{(2)}(\tau)$ for a non-classical light source can take values in an extended range, compared to the classical range:

$$1-\frac{1}{\langle n\rangle} < g^{(2)}(\tau) < \infty \quad for \quad \langle n\rangle \geq 1, \qquad for\, all \quad \tau$$
$$1-\frac{1}{\langle n\rangle} < g^{(2)}(0) < 1 \quad for \quad \langle n\rangle \geq 1 \tag{3.5}$$

The difference between the ranges of the $g^{(2)}(\tau)$ values in classical and quantum regimes lies in their numerators. The first one correlates the average intensity $\bar{I}(t)$, while the second correlates number of photons $n$.

### 3.4.3 Photon Bunching and Antibunching

The quantum degree of the second-order coherence can be derived not only for the non-classical light, but for chaotic light as well, which was previously presented in the classical picture. Let us consider a chaotic light beam with Lorenzian frequency distribution. If it is treated as a photon flux, then the quantum degree of coherence agrees with the classical expression for $g^{(2)}(\tau)$, and the classical inequality $g^{(2)}(\tau) \leq g^{(2)}(0)$ is fulfilled in the quantum theory, too. In the photon correlation experiment this will manifest in photon *bunching* what means that the photons are emitted in groups as they tend to bunch (see Figure 3.7 (a)). The details on statistics of chaotic light with Lorenzian spectrum can be found in Ref. [7].

The coherent light (i.e. laser) has no intensity fluctuations either in the classical regime or in the quantum regime. The degree of second order coherence $g^{(2)}(\tau)$ is equal to 1 in both cases, and corresponds to the *Poissonian* statistics. The fluctuations in $g^{(2)}(\tau)$ reflect a random stream of photons, in agreement with both classical and quantum theory (Figure 3.7 (b)).

In the case of source which does not emit more than one photon at once and, moreover, the photons tend to be emitted with a characteristic delay time, than one observes *antibunching* in the photon stream. The quantum degree of second order coherence satisfy the inequality $g^{(2)}(\tau) < 1$ in this case, what does not have a classical equivalent. This type of photon statistics is called sub-Poissonian and it characterizes the one-by-one photon emission. A multi-photon event is unlike to occur in this case (Figure 3.7 (c)). The light sources with the sub-Poissonian statistics have strictly quantum character, so their emission can be observed only in those physical systems with no classical description. Single atoms, ions, molecules

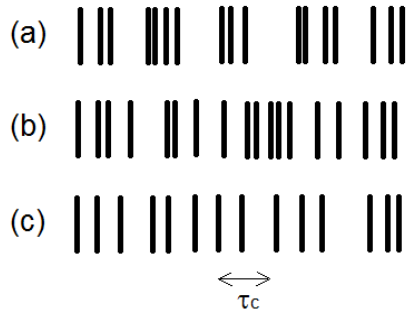


Figure 3.7 Schematic illustrations of the series of registered photon events for light beams of different statistics: (a) bunched, (b) random, and (c) anti-bunched.

or quantum dots are well known quantum emitters, and in all of them the anti-bunching phenomenon has been observed experimentally [9-12].

### 3.4.4 Auto- and Cross-correlation Function in QD

The correlation measurement of second order is a very good tool to determine whether a light source is a single photon emitter (SPE) or not. The auto-correlation experiment - commonly used for that purpose - consists on measuring second order correlation between the photons of the same frequency ν. The photon beam is divided in two beams by a 50/50 beam splitter (see. Figure 3.2 (b)), so the photons have equal probability to reach one of the two APDs. The $g^{(2)}(\tau)$ function is obtained by constructing a histogram, analogue to the one described in section §3.3, and normalized to the average coincidence number for $\tau\to\infty$. Moreover, instead of recording photon arrival to the detector versus arrival time, here one records photon pair detection at the two detectors versus arrival time difference. Anti-bunching is proven by a dip in $g^{(2)}(\tau)$ for zero delay, and evidences single photon emission (ideally when $g^{(2)}(0)=0$). In this case $g^{(2)}(\tau)$ can be well described by formula:

$$g^{(2)}(\tau) = 1 - \beta \cdot \exp\left(\frac{-|\tau|}{\tau_R}\right), \tag{3.6}$$

where $\tau_R$ is the characteristic anti-bunching time, and β is a parameter which contains information about the efficiency of the SPE. In the ideal case β=1, however it could be reduced by undesired background emission, decoherence processes or presence of more than one SPE in the same spectral range (in the latter situation $g^{(2)}(0) = 1 - 1/n$, where $n$ is number of SPEs). The study of $g^{(2)}(\tau)$ not

only provides information about the statistical nature of the source, but as well gives the insight to the dynamics of the emission process.

Another application of the second order correlation measurement is studying the correlation between photons originated in the same SPE at different frequencies $\nu_1$ and $\nu_2$, (as for instance resulting from two different transitions) in stationary conditions. The second order correlation function in this case is defined by:

$$g_{1,2}^{(2)}(\tau) = \frac{\langle I_{\nu 1}(t) I_{\nu 2}(t+\tau) \rangle}{\langle I_{\nu 1}(t) \rangle \langle I_{\nu 2}(t) \rangle}. \tag{3.7}$$

Eq. (3.8) represents a photon cross-correlation experiment in which one records the coincidence events of photons of frequency $\nu_1$ detected at one APD, and photons of frequency $\nu_2$ reaching the other detector. The form of the measured cross-correlated $g^{(2)}(\tau)$ will reflect correlations between the emission processes of the two kinds of photons. The examples of auto- and cross-correlation $g^{(2)}(\tau)$ plots can be found in chapter §6.2.

### 3.4.5 Photon Correlation Experimental Set-up

For the second-order correlation measurements one uses the Hanbury-Brown and Twiss (HBT) interferometer (Figure 3.2 (b)) integrated with the micro-PL set-up. The spectrometer serves to filter the selected light emission frequency. The HBT interferometer consists of a 50/50 beam splitter followed by two APDs placed on the transmitted and reflected light path, respectively. Each detector is connected by a coaxial cable to one of the two channels in the coincidence counter which records the time of the electrical pulse arrival. In the measurements presented in this thesis the PicoHarp 300 single-photon counting (SPC) module was used for its high timing-resolution [2]. The APDs provide “START” and “STOP” signals to the SPC in the moment they detect a photon. The minimum time delay between two photon counts registered by PicoHarp300 is 4 ps, but the temporal resolution is limited by the avalanche rise time in the detectors. Time-Tagged-Time-Resolved (TTTR) mode (available in PicoHarp 300) allows recording of each photon event separately, with the individual arrival times assigned to one of the channels. The output list of the arrival times sent to a PC serves to construct a histogram of the coincidence between the channels “START” and “STOP”. It is done by counting the number of coincidences in distinct channels for different delays between the photon count events. The histogram can be constructed with different delay resolution: $r = 2^n$ (n = 0, 1, 2…), so called *binning* resolution. Typically, the

resolution of 64 ps or 128 ps was good enough to observe photon bunching or anti-bunching.

*Timing resolution*

There are various factors which limit the timing resolution of the TRPL or TCSPC measurements. Usually, the most crucial one is the electric pulse rise time in the APD and its jitter (see Figure 3.8 (a)). Also the time jitter of the electronic components used in the SPC module affects the precision of the electric pulse detection. However, the contribution of the electronics to the total time uncertainty is less than 10 ps. The total time resolution of the APDs can be determined from the Full Width Half Maximum (FWHM) of the instrumental response function (IRF). This IRF can be determined by measuring the time-correlated SPC response to a short (<10ps) laser pulse. Figure 3.8 (b) shows a histogram representing the IRF of the Perkin Elmer SPCM AQRH-16 module measured with 2 ps pulses of a Ti: Sapphire laser. The response time ($\tau_{IRF}$) obtained from a Gaussian fit is equal to 0.46 ns in this case. Note that $\tau_{IRF}$ depends on spot size, wavelength and signal rate. It is crucial then to focus the light spot on the detector area in the most precisely way as possible.

The response time $\tau_{IRF}$ values and other important specifications of the APD detectors used in this thesis are listed in the Table 3.5.

**Table 3.5** Technical details of APD detectors used in TCSPC experiment.

| Parameter \ Detector | PerkinElmer (SPCM AQRH-16) | PicoQuant (τ-SPAD 50) | Micro Photon Devices (MPD-5CTC) |
|---|---|---|---|
| Photon detection efficiency at 670nm | 65% | 86% | 33% |
| Active area diameter (μm) | 170 | 150 | 50 |
| Timing resolution at FWHM (ps) | min. 350 * | min. 350 * | < 50 |
| Optimum spot size diameter (μm) for max. timing resol. | - | 30 | 50 |
| Dark count (counts per second) | 20 | max. 50 | < 50 |
| Dead time (ns) | 50 | 50 | 77.4 |
| After-pulsing probability: | 0.5% | 0.5% | max 3 % |

* depends on spot size, wavelength and signal rate.

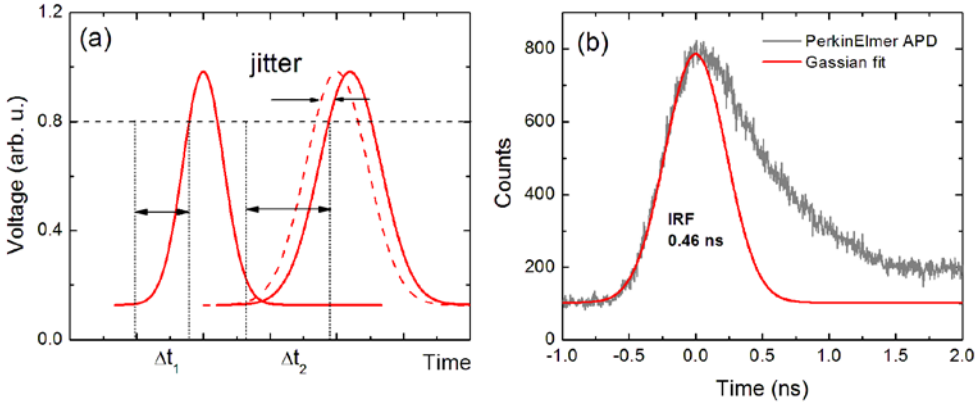


Figure 3.8 (a) Scheme of the electrical pulse detection by the SPC module. The timing resolution can be affected by APD jitter or rise time of the electric pulse. The horizontal, dashed line represents detection level of the SPC module. (b) Histogram representing the IRF of the PerkinElmer SPCM AQRH-16 module measured with a Ti: Sapphire pulse laser (pulse duration 2 ps).

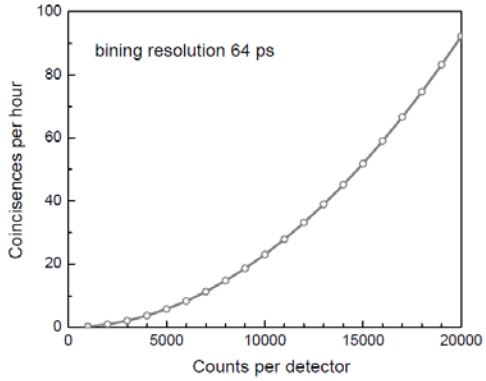


Figure 3.9 Estimation of the coincidence number ‹*C*› per hour for 64 ps binning resolution and equal count rates in the detectors.

The timing resolution of the HBT may affect the experimentally observed $g^{(2)}(\tau)$ values. Indeed, if the antibunching time $\tau_R$ is not much larger than the instrumental response time $\tau_{IRF}$, then the anti-bunching dip gets broadened. This broadening effect must be taken into account while analyzing the experimental results. The measured correlation function is in fact a convolution of the instrumental response function IRF, $h(\tau) \sim \exp(-|\tau|/\tau_{IRF})$ [13], and the real $g^2(\tau)$ function. To obtain the real $\tau_R$ values one has to deconvolute the measured correlation function $g^2_{meas}(\tau)$. With this method it is possible to measure times shorter than the IFR [14].

*Acquisition time*

The single photon correlation measurement is a statistical experiment and requires registering many excitation-emission events. That means that the measurement duration will depend among others on the number of photons detected in the detectors per time unit. The mean number of count coincidences ‹C› occurred between the "START" and "STOP" detectors at long delay times ($\tau \to \infty$) can be approximated by equation: $\langle C \rangle = N_1 N_2 \cdot \Delta t \cdot t$, where $N_i$ ($i$=1,2) is the number of counts per second in $i$-th detector, $\Delta t$ is the time binning resolution, and $t$ is the acquisition time. Note that the time required to collect ‹C› coincidences depends on the product of photon numbers $N_1 \cdot N_2$ collected in both detectors (see Figure 3.8). That implies that the number of counts detected in the APDs should be as high as possible to realize one measurement in relatively short time with low noise-to-signal ratio, and to prevent the possible misalignment in the experimental set-up due to mechanical or electrical instability. Typical recording time in our experimental conditions varies between 2 and 24 hours.

*Breakdown flash*

The effect of the breakdown flash, mentioned in §3.3, is quite typical in Si avalanche photodiodes and it may cause problems in SPC experiments. If the APDs are placed in a typical HBT interferometer (see Figure 3.1 (b)), the breakdown flash photons from one of the detectors could be reflected through the cube beamsplitter or from the entrance lens and would reach the other APD. In consequence a communication between the detectors would take place and a coincidence event would be registered by the counter module. This coincidence event would be

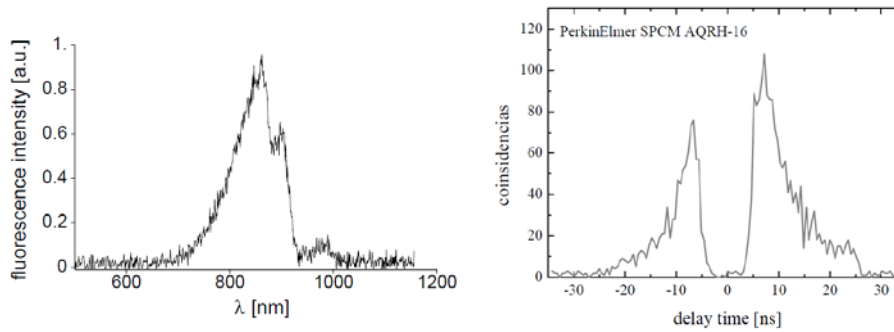


Figure 3.9 (*Top*) spectrum of the Si APD breakdown-flash [6]. (B*ottom*) typical bunching maxima due to APDs communication originated by the breakdown flash effect. Measurement was done with PerkinElmer SPCM AQRH-16 module.

reflected in the histogram as bunching of photons for short delay times, which correspond to the breakdown flash time. In the case of the PerkinElmer APDs this time is approximately 7 ns. Typical bunching maxima due the breakdown flash effect are shown in Figure 3.9 (*bottom*). To avoid the APD communication some modification of the HBT interferometer must be introduced. The cube beamsplitter has been replaced by a plate beamsplitter (i.e. thin silica beamsplitter or polka type beam-splitter).[3] Additionally, long- or short-wave pass filters have been placed in front of each APD. The filters should reflect or absorb photons in the breakdown flash spectral range [6] (see Figure 3.9 (*top*)), while letting pass through the photons emitted by the sample. If the sample signal dose not overlaps in the wavelength with the APD emitted photons, than there should be no spurious bunching maxima in the histogram. Other possible solutions can be found in Ref. [15].

# References


[1] P.Y. Yu and M. Cardona "Fundamentals of semiconductors: physics and material properties," § 7.1, Springer-Verlag, Berlin (1996)

[2] see for instance: D. Sarkar et al. Phys. Rev. B **78**, 241305R (2008)

[3] M. Wahl and R. Erdmann, "*Time-Correlated Single Photon Counting in Fluorescence Lifetime Analysis*," PicoQuant GmbH, January and April 2000.

[4] Hamamatsu Photonics K. K., Systems Divisions, "Guide to Streak Cameras", http://sales.hamamatsu.com/assets/pdf/catsandguides/e_streakh.pdf

[5] R. Hanbury Brown and R. Q. Twiss, Nature 178 (4541) pp. 1046–1048 (1956)

[6] C. Kurtsiefer, P. Zarda, S. Mayer, H. Weinfurter, J. Mod. Opt. **48**, 2039-2047 (2001)

[7] R. Loudon, "*The Quantum Theory of Light*", Oxford University Press (2000)

[8] C. C. Gerry and P. L. Knight, "*Introductory Quantum Optics*", §6.5, pp. 248-250, Cambridge University Press (2005)

[9] H. J. Kimble, M. Dagenais, L. Mandel, Phys. Rev. Lett. 39, pp. 691-694 (1977)

[10] F. Diedrich and H. Walther, Phys. Rev. Lett. 58, pp. 203-206 (1987)

[11] Th. Basché,W. E. Morener, M. Orrit, H. Talon, Phys. Rev. Lett. 69, pp. 1516-1519 (1992)


[3] Note that the beamsplitter should be non-polarizing, 50/50 for both linear polarizations, if the polarization dependent correlation is to be studied.

[12] P. Michler, A. Imamoglu, M. D. Mason, P. J. Carson, G. F. Strouse, and S. K. Buratto, Nature (London) **406**, 268 (2000).

[13] M. Reischle, G. J. Beirne, W.-M. Schulz, M. Eichfelder, R. Roßbach, M. Jetter, and P. Michler, Opt. Express **16**, 12771 (2008).

[14] D. V. O. O'Connor, W. R Ware, J. C Andre, J. Phys. Chem. 83, pp. 1333-1345 (1979)

[15] W. Becker, *"Advanced time-correlated single photon counting techniques"*, Springer-Verlag Berlin Heidelberg, 2005

# Chapter 4

# Optical Properties of InP/GaInP Quantum Dots

This chapter presents experimental results of the optical properties of InP/GaInP QD. First the growth sequence of the sample and the QD ensemble optical emission will be described. Latter the optical characterization by different spectroscopy methods will be presented for various individual QD. In the end the emission dynamics of single QDs and the influence of the QD size and temperature on the recombination process will be discussed.

## 4.1 Sample Description

The InP/(Ga,In)P QD samples studied in this thesis have been grown by molecular beam epitaxy (MBE) on GaAs (001) substrates at the "Instituto de Microelectrónica de Madrid". The growth sequence was 100 nm GaInP, 2 mono-layers (ML) GaAs, and 2.2 ML InP, repeated twice. The critical thickness for QD nucleation at 470ºC was 2 ML of InP at a growth rate 0.05 ML/s, so that InP QDs were formed. The second uncapped layer of QDs was used for atomic force microscopy (AFM) characterization (Figure 4.1 (b)). The scanning electron microscope (SEM) image (Figure 4.1 (a)) reveals the QD average diameter (d) and height (h) before capping to be 35 and 6 nm, respectively. However, the height of QDs is well known to decrease after capping. Statistical analysis of the SEM and AFM images reveals two size ensembles within the QD sample: i) large (d=48 nm, h=9 nm, density $\rho=3.4\times10^{9}$ $cm^{-2}$), and ii) medium (d=25 nm, h=5 nm, density $\rho=2.5\times10^{9}$ $cm^{-2}$). The QDs grown by Stranski – Krastanow method are characterized by random position in the sample and by wide spectral distribution.The single QDs selected for this work are in the high energy tail of the ensemble PL well outside the ensemble (see next section). We estimate their height between 1 and 2 nm from the emission energy. Being the smallest QDs of the

ensemble reduces significantly the contribution of other QDs to the background emission, and also prevents charge transfer from neighbouring QDs.

## 4.2 Optical Characterization

The micro-PL spectrum of our InP/(Ga,In)P QD sample is presented in Figure 4.1 (c). The broad emission between 1.6 eV and 1.8 eV corresponds to the QD ensemble. The two local maxima at 1.65 eV and 1.75 correspond to two size groups of the QDs mentioned in the previous section: large and medium.[1] In the high energy tail of the PL ensemble presented in the Figure 4.1 one observes sharp peaks with very little background emission. These are the small QDs (1-2 nm height), which are spectrally separated from the bigger ones. Their average spatial separation is of the order of 0.2 μm, what enables optical access to single QDs without using masks or mesas. The typical micro-PL spectra of single QDs are presented in Figure 4.2.

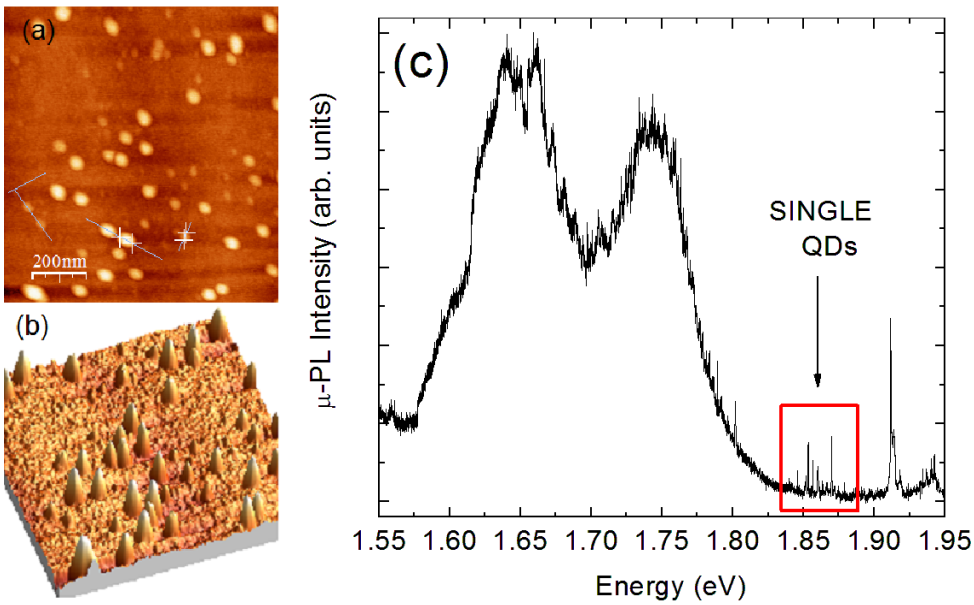


Figure 4.1 (a) SEM image and (b) AFM image of the InP/GaInP QD sample before capping; (c) micro-PL spectrum of the QD ensamble measured at 8 K.

[1] A rapid thermal annealing (RTA) treatment at temperature above 850º over 5 seconds makes the QDs size dispersion more homogenous and only one much narrower PL peak for the QDs ensemble is observed for the same excitation power (not shown).

Three lines are identified by their intensity dependence on excitation power (Figure 4.3 (a)) and linear polarization (Figure 4.3 (b)). Black and red traces correspond to linear polarization parallel to the [110] and [1-10] crystallographic directions, respectively. The emission intensities follow the power dependence $I \sim P^S$, where $s$ is the slope of the linear fit to the experimental points in the doubly logarithmic scale (Figure 4.3(b)). The slopes obtained for QD2 are indicated in Figure 4.3(a). Their values (1.8±0.1, 1.3±0.1 and 1.0±0.1) allow to assign the corresponding PL lines to the neutral biexciton ($XX^0$), negatively charged exciton ($X^{1-}$) and neutral exciton ($X^0$), respectively. The same procedure was applied for all QDs under study.

The band structure of the InP/GaInP QDs is characterized by a negative valence band (VB) offset in the absence of strain [1] ($\Delta E_V$ = -0.45 meV) and rather ordinary band offset in the conduction band (CB) ($\Delta E_C$ = 240÷250 meV). In real QDs, strain reduces somewhat the CB barrier, but electrons are still well confined inside the dot. In contrary, holes become weakly confined in the dot only by strain. This fact could explain the absence of intense $X^{1+}$ together with presence of the very intense $X^{1-}$, as the probability of capturing a hole inside the potential barriers is low in comparison to the probability of an electron.

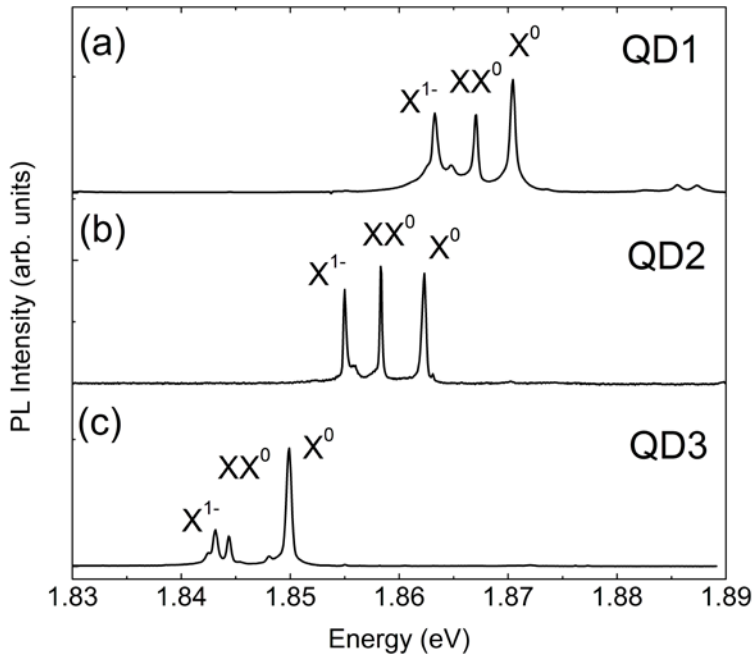


Figure 4.2 Micro-PL spectra for three single QDs. The spectra were off-shifted for clarity. The different energies of the emission lines suggest differences in QD sizes.

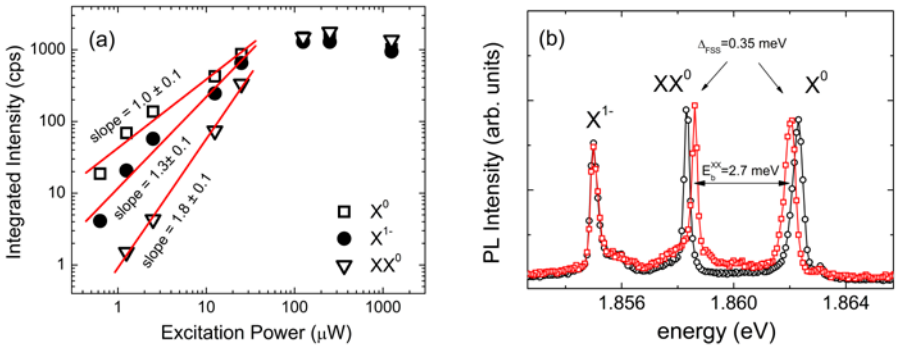


Figure 4.3 (a) The power dependence for the emission lines assigned to neutral exciton ($X^0$), negatively charged exciton ($X^{-1}$) and neutral biexciton ($XX^0$). (b) Spectrum of QD2 showing the fine-structure splitting ($\Delta_{FSS}$). The $\Delta_{FSS}$ and binding energy of the biexciton ($E_b^{XX}$) in this particular QD are equal 0.35 meV and 2.7 meV, respectively. The black and red lines represent vertical (V) and horizontal (H) polarization components, respectively, parallel to the crystallographic directions.

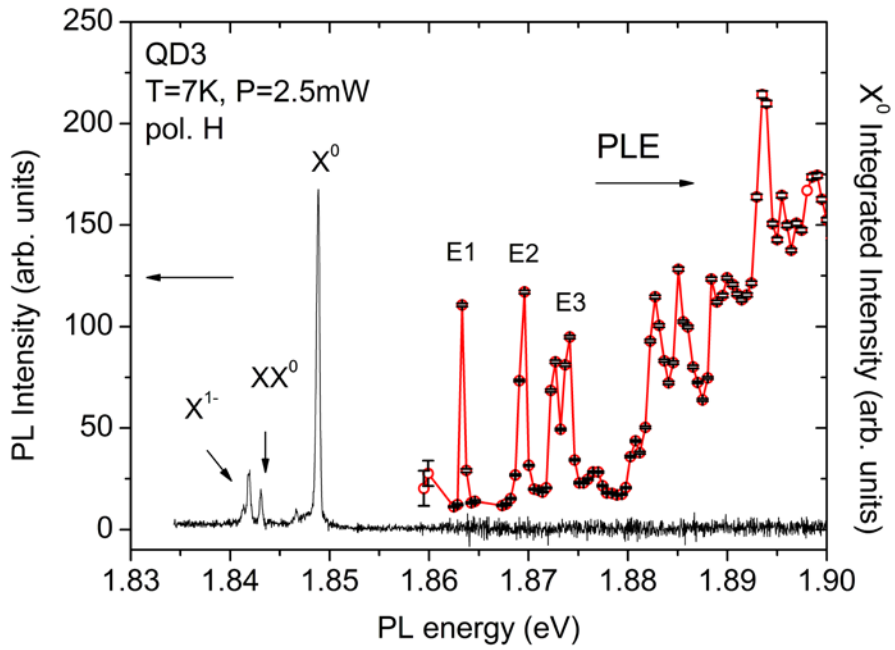


Figure 4.4 Micro-PL spectrum (left) and PLE spectrum (right) of QD3 measured for the neutral exciton. In the PLE spectrum there are various sharp peaks corresponding to the excited states. Above 1.88 eV one observes a quasi-continuum due to proximity of the WL (1.95 eV).

The different energy of the emission lines for the QDs shown in Figure 4.2 suggests different QD sizes. Besides, the biexciton binding energy ($E_b^{XX}$) increases for lower $X^0$ emission energies. That suggests differences in the exchange energy which depends on the overlap of the electron and hole wave functions and is strongly related to the size and shape of the QD [2,3]. A more detailed analysis of the $E_b^{XX}$ dependence on QD size can be found in chapter §6.2.

The excited states of the QDs were studied by micro-PLE. Figure 4.4 shows the PLE spectrum recorded for QD3. The sharp peaks, at energies between 1.86 eV and 1.88 eV above the emission energy correspond to absorption transitions involving excited states of the QD. For energies greater than 1.88 eV one observes an increase and broading in the PLE spectrum, what is associated to the quasi-continuum of the WL. The emission intensity dependence on excitation (horizontal axis) and emission (vertical axis) energy measured for the QD2 is shown in Figure 4.5. The excitation polarization was set at 45º to excite equally both polarization components of the QD emission. Various maxima in the PLE spectrum are detected between 20 and 40 meV above the emission energy (1.86 eV). They correspond to the p-shell excited states of the QD2. The three oblique lines correspond to Raman scattering by phonons: the GaP LO (395 $cm^{-1}$), InP LO (371 $cm^{-1}$) and (Ga,In)P TO (307 $cm^{-1}$). The measured values for the LO and TO lines are in good agreement with the values reported in reported in Ref. [4]. As no PL intensity increase is observed at the crossings of the PL and Raman lines, one can exclude phonon-assisted transitions in the PLE spectra. Consequently, the sharp PLE lines observed are electronic transitions between excited states (generically "p-states").

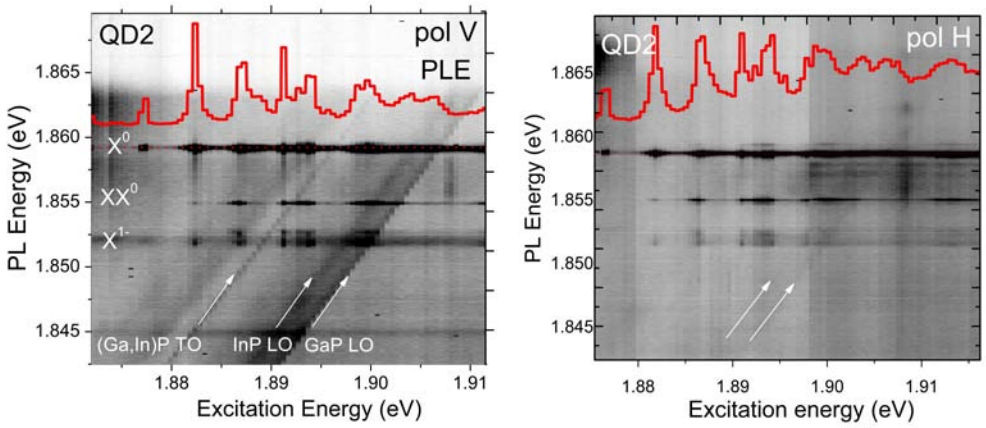


Figure 4.5 Emission intensity dependence on excitation (horizontal axis) and emission (vertical axis) energy measured for the V polarization component of the QD2 emission (7 K). The red line represents PLE profile for the neutral exciton ($X^0$).

## 4.3 Emission Dynamics of Quantum Dot

The decay characteristics of excitonic states in a single QD can be studied by simultaneous time- and space-resolved micro-PL. This method allows comparing the radiative decay times of various excitonic states confined within the same QD. In this section two excitonic states of $X^0$ and $XX^0$ will be studied, since their recombination processes are directly related: the final state of the $XX^0$ recombination is the initial state of the $X^0$ one. Figure 4.6 (a) shows the PL time decay of $X^0$ and $XX^0$ measured for a single QD2. The $X^0$ decay time ($\tau_1$=490±10 ps) is approximately double than the $XX^0$ one ($\tau_2$=270±10 ps).

The influence of the QD size on the emission dynamics was calculated by Wimmer et al. [5] in self-assembled InP/GaInP QDs. There are two limits for recombination rates $\Gamma_i = 1/\tau_i$, depending on the confinement strength. In the *strong confinement* limit, confinement affects the individual electron and hole wave functions. In this case $X^0$ and $XX^0$ wave functions are products of the *e-h* single particle functions, and their Coulomb interaction is only a small perturbation. Taking in to account the number of the allowed channels for the recombination process, the $XX^0$ should decay twice faster than $X^0$ ($\Gamma_{XX}/\Gamma_X$) = 2). In the weak confinement limit the $X^0$ and $XX^0$ radii are smaller than the QD size, so that they are bulk-like, with a small perturbation by the confining potential. In this case the dipole matrix element is dominated by the exciton or biexciton structure, which is independent of dot size. The exciton wave function extends across the volume of the dot, leading to constructive addition of radiative matrix elements for exciton decay. Thus, in the weak confinement limit, the radiative decay rate of the exciton *increases* with dot size. For the biexciton, the exciton final state after recombination suppresses this constructive enhancement [5], leading to $\Gamma_{XX}/\Gamma_X \rightarrow 1$ in the weak confining limit. For intermediate confinement the coherent extent of the many-particle wave function compared with the QD size leads to increasing decay rates, which is stronger for the exciton than for the biexciton. Consequently one has $2>(\Gamma_{XX}/\Gamma_X)>1$ and the ratio decreases with dot size [5].

The decay rates ratio measured $\Gamma_{XX}/\Gamma_X$ in our QDs are shown in see Table 4.1, together with the calculated values of Ref. [5]. Both sets of values agree rather well with each other. Also our measured values of $\Gamma_X$ and the biexciton binding energy lie in the calculated range. Thus, although the model dimensions of the QD used in the calculations of Ref. [5] are larger than ours, these results suggest that our self-assembled InP/InGaP QDs lie in the intermediate confinement regime.

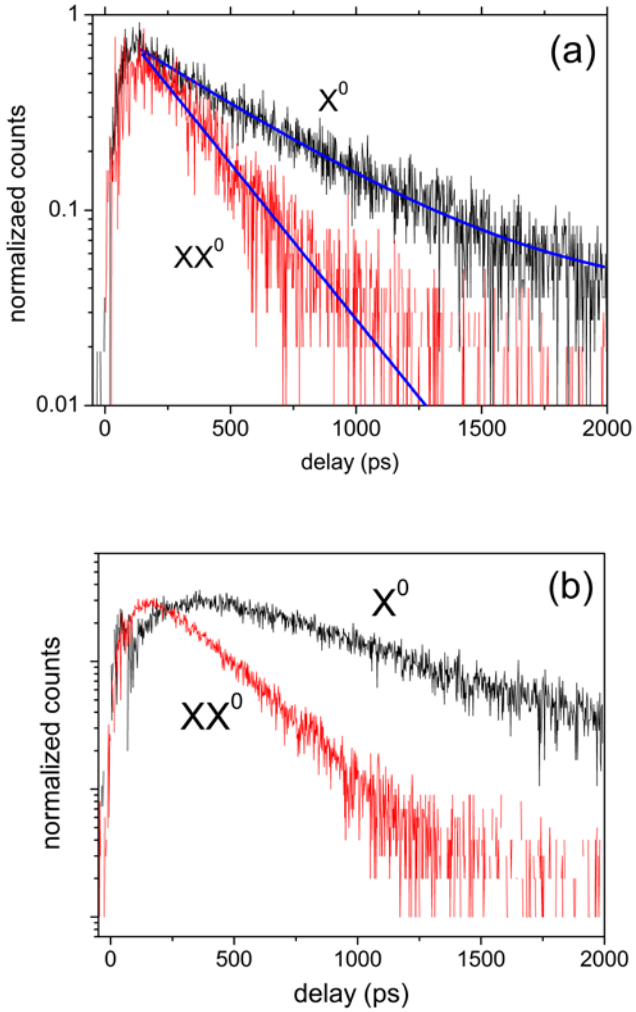


Figure 4.6 Time evolution of the exciton ($X^0$) and the biexciton ($XX^0$) PL intensity for QD2 measured by TRPL for 300 μW (*left*) and 490 μW (*right*) excitation power. The temperature was 12 K. For the low excitation power the decay times of $X^0$ and $XX^0$ are 490±10 ps and 270±10 ps, respectively.

Table 4.1 Calculated values [6] for QD increasing diameter $\phi$ = (10÷60) nm and measured values in our single InP QDs.

| Calculated values for increasing $\phi$ | measured values | |
|---|---|---|
| | QD2 | QD3 |
| $\Gamma_{XX}/\Gamma_X = (1.9 \div 1.55)$ ns$^{-1}$<br>$\Gamma_X = (2 \div 6)$ ns$^{-1}$<br>$E_b^{XX} = (2 \div 5)$ meV | $\Gamma_{XX}/\Gamma_X = 1.92$ ns$^{-1}$<br>$\Gamma_X = 2.2$ ns$^{-1}$<br>$E_b^{XX} = 2.7$ meV | $\Gamma_{XX}/\Gamma_X = 2$ ns$^{-1}$<br>$\Gamma_X = 5$ ns$^{-1}$<br>$E_b^{XX} = 5.3$ meV |

### 4.3.1 Effects of Excitation Power

In this section we describe the effects of the excitation power on the QD emission dynamics. These effects are mainly due to the power dependent probability of multi-exciton occupation in the QD and the role played by dark excitons.

The time evolution of the population probability of the $XX^0$ and $X^0$ states can be described by the rate equations [6]:

$$\frac{dN_{XX}}{dt} = -\frac{N_{XX}}{\tau_{XX}}$$
$$\frac{dN_X}{dt} = -\frac{N_X}{\tau_X} + \frac{N_{XX}}{\tau_{XX}} = -N_X\left(\frac{1}{\tau_{X0}} + \frac{1}{\tau_{DB}}\right) + \frac{N_{XX}}{\tau_{XX}} \quad (4.1)$$

where $N_X$ and $N_{XX}$ are the population probabilities of and XX, respectively, $\tau_{X,XX}$ are their respective decay times, $\tau_{X0}$ is the intrinsic exciton recombination time and $\tau_{DB}$ is the dark-to-bright exciton transition time. The solution of the rate equation system gives the mono- and double-exponential decays for $XX^0$ and $X^0$, respectively. The radiative recombination from the $XX^0$ state is allowed only into the bright $X^0$. Moreover, a change in the probability of the $XX^0$ occupation $N_{XX}$ has an influence in the $X^0$ decay. This effect is observed comparing Figures 4.6 (a) and (b), where the PL decay of the QD2 was measured for low and high excitation power, respectively. At high excitation power the $X^0$ state is *refilled* by the increased probability of $XX^0$ formation. This *refilling* is evident from the slower rise of the $X^0$ intensity in Figure 4.6 (b). In consequence, for increased excitation powers one should observe a progressive increase of the $X^0$ decay time, while the $XX^0$ life time should not be affected. Indeed this is precisely what we observe in the experiment. Figure 4.7 shows the power dependence of $\tau_X$ and $\tau_{XX}$ measured for QD2. A moderate increase for the $\tau_X$ is observed while $\tau_{XX}$ stays rather constant.

### 4.3.2 Effects of Temperature

In this section the temperature dependence of the exciton decay time ($\tau_X$) in our QDs will be presented. Figure 4.8 shows the decay times of QD2 (red points) and QD3 (black points) measured for temperatures in the range from 12 K to 72 K. The experiment was run under low excitation power (60 μW), so the intensities of $XX^0$ and $X^{1-}$ are much smaller than the the $X^0$ one. Marked differences are observed for both QDs. At low temperature QD2 has longer $\tau_X$ (350 ps) than QD3

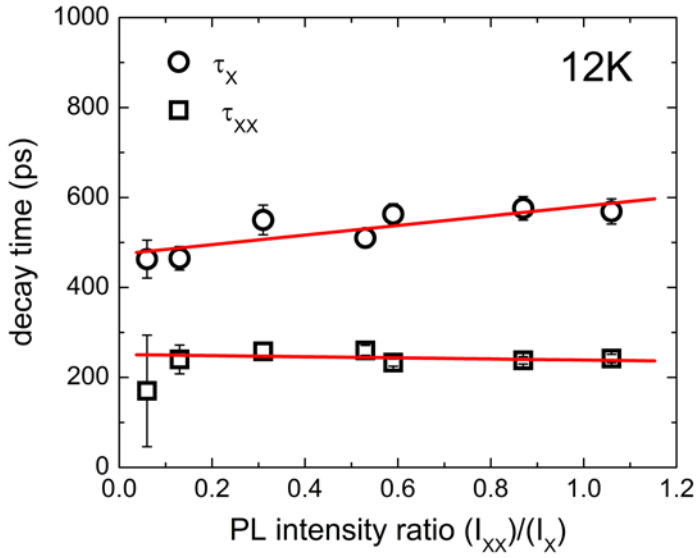


Figure 4.7 Power dependence of $\tau_X$ and $\tau_{XX}$ measured in low temperature (12 K). The red lines are the linear fit to the experimental points. The intensity ratio of the XX and X is used as the excitation power equivalent.

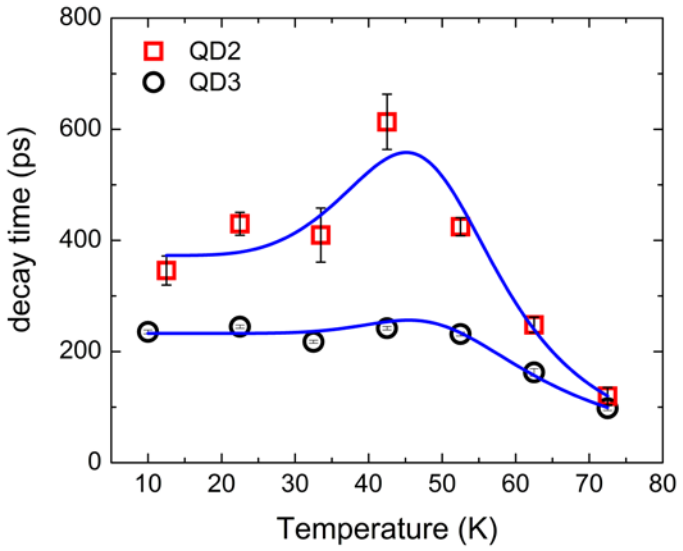


Figure 4.8 Temperature dependence of the decay times $\tau_X$ for the neutral exciton ($X^0$). The experimental data were taken for 1.93 eV excitation energy, and 60 μW excitation power. The lines are fits of Eq. (4.7) to the measured values, with $E_A$(QD2)=10 meV, $E_A$(QD3)=30 meV, and $E_{LA}$(X,K)=25meV.

(230 ps), which increases with temperature up to 50K. The QD3 decay time is constant in the same range of temperature. For both QDs the decay time starts to decay above 50K.

According to the previous discussion, this suggests different sizes of the QDs. Basing on the calculation reported in Ref. [5] one concludes that QD2 with longer $\tau_X$ is smaller than QD3. This is in agreement with the PL results shown in Figure 4.3 (b) and (c), where QD2 has higher emission energy than QD3.

The temperature dependence of the decay time in QD has been reported for InGaAs/InP QDs [7] and in InAs/InGaAs QDs [8]. Assuming the QD discrete density of states and that the ground state occupation follows the Boltzmann distribution, the decay time can be expressed by [9]:

$$\frac{1}{\tau_X(T)} = \frac{1}{\tau_X(0)} \cdot \frac{1}{1+\sum_n \exp\left(-\frac{E_n - E_0}{kT}\right)}, \tag{4.3}$$

where $\tau_X(0)$ is the decay time at 0K and $E_n$ are discrete energy levels confined in the QD. In general the exciton lifetime will be temperature independent as long the level separation is larger than *kT* (either at low T or high confinement). At higher temperatures $\tau_X(T)$ *increases* as a result of the increasing "storage" time of carriers in excited states. Apart from that, carriers can escape irreversibly to the WL continuum by thermal excitation. This process is responsible of a $\tau_X(T)$ *decrease*.

In the literature there are various reports on the temperature dependence of the decay time for semiconductor QDs ensemble. For InAsP/InP QDs [10] and InAs/InP QDs [11] thermal effects on the QD dynamics is discussed. In both cases the $\tau_X$ remains stable up to a certain temperature and then it starts to grow. In both cases this increase is explained by the thermal excitation of carriers to the upper energy states or defects. It is enough to excite only one of the carriers from the electron-hole pair to the upper excited state (i.e. p-shell) to delay the $X^0$ emission. The excited carrier relaxes after some time to the ground state, and in consequence the decay time increases.

In CdSe QDs reported in Ref. [12,13] a decrease of $\tau_X$ was observed while increasing the temperature. This behaviour was explained by thermally activated transition from the dark (DX) to bright (BX) state of the neutral exciton. The spin configuration of DX prevents radiative recombination (see chapter 2) and its lifetime is much longer (of order of several ns) than the BX one [14]. The phonon

mediated spin flip from dark to bright state decreases the radiative recombination time of the *e-h* pair.

The above interpretation of the temperature dependent decay time can be applied to our QD2 and QD3 cases. As QD2 is smaller than QD3, the confined states are closer to the WL continuum and the probability of carrier excitation (especially the holes [1]) is elevated in the higher temperature regime. For QD3 $\tau_X$ remains constant up to 50 K, what suggests that thermal excitation of carriers is not as efficient as in QD2 or is compensated by the DX→BX transition. This interpretation will be confirmed by the temperature dependence of the antibunching times in chapter §6.

For temperatures above 50 K the life time of the $X^0$ decreases for both QDs. A similar trend was reported in InAs/InGaAs QDs above 170 K [8], InAs/GaAs QDs above 100 K [15], and InP/AlGaInP QDs above 190 K [16]. The $\tau_X$ decrease can be explained in terms of the excitation of carriers to the WL continuum by phonon absorption or scattering.

The two mechanisms described above are sketched in Figure 4.9, where carriers can by thermally excited from the exciton ground state (a) to excited confined states (b) or to the WL (c). Depending on the dominating mechanism, the PL decay time will increase (b) or decrease (c). In our case only hole thermal excitation is relevant, as the excited states are closer in energy due to the small valence band offset. Only two confined hole states (heavy and light) are expected in our small dots. The decay time $\tau_X$ at fixed temperature can be obtained from the kinetic equation [8]:

$$\frac{dN}{dt} = -\frac{N}{\tau_0} - \frac{N}{\tau_{phn}} + \frac{N}{\tau_{phn}}\gamma(T), \tag{4.4}$$

where N is the exciton occupation probability, $\tau_0$ is the radiative recombination time at zero temperature, and $\tau_{phn}$ is the scattering time by phonons. The function $\gamma$(T) accounts for the thermally activated carrier exchange to QD excited states. The second term in the right hand side of Eq. 4.4 stands for the $\tau_X$ decrease due to thermal excitation of carriers to the WL, while the third one describes the $\tau_X$ increase due to carrier storage in excited states. The phonon scattering time is determined by the Bose-Einstein distribution for phonons of $E_{phn}$ energy:

$$\frac{1}{\tau_{phn}} \propto N_{phn} = \frac{1}{\exp\left(E_{phn}/kT\right) - 1} \quad . \tag{4.5}$$

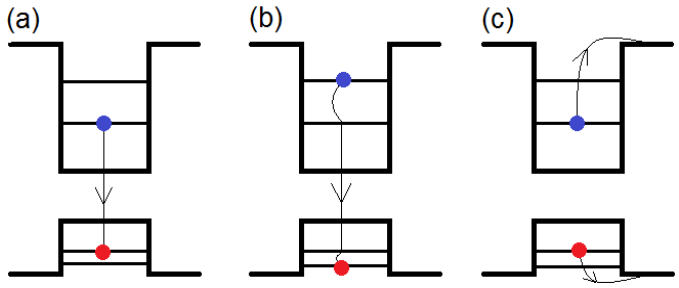


Figure 4.9 Illustration of the temperature dependent recombination inside the QD for (a) low, (b) mediate, and (c) high temperatures.

The function γ(T) is given by:

$$\gamma(T) = \frac{q}{1 + p \cdot \exp(-E_A / kT)} \quad , \tag{4.6}$$

where $E_A$ is the activation energy and q and p are parameters determined by the mechanism of carrier transfer to the WL [8] or excited states. This function governs the well known PL decay with temperature in semiconductor systems. The activation energy $E_A$ can be obtained from the temperature dependence of the $X^0$ PL intensity I(T) ~ γ(T). For QD2 and QD3 we obtain $E_A$ = 10 and 30 meV respectively. The decay time obtained from Eq. (4.4) is:

$$\frac{1}{\tau_X} = \frac{1}{\tau_0} - C\left(\frac{1}{\exp(E_{phn}/kT) - 1}\right)\left[1 - \left(\frac{q}{1 + p \cdot \exp(-E_A/kT)}\right)\right], \tag{4.7}$$

where C is a constant resulting from the proportionality relation in Eq. 4.5. This expression is plotted as blue lines in Figure 4.8. C, p and q were used as fitting parameters. The $E_A$ values were obtained from the temperature dependent PL, as explained above. As for the phonon energy, no reasonable fit could be obtained for the LO values. Instead a common value $E_{phn}$= 25 meV for both QDs was used. This phonon energy corresponds to the acoustic longitudinal phonons of InP at the Brillouin zone edge (LA(X), LA(K)), where the phonon density of states has a maximum. For QD2 one has $E_A < E_{phn}$, so that a $\tau_X$ increase followed by a decrease at higher temperature is observed. Instead, for QD3 $E_A \approx E_{phn}$ (what means that the hole excited state is degenerate with the continuum), so that no increase is observed. As the agreement of the temperature dependence given by Eq. 4.7 and the experimental results is quite satisfactory, we conclude that the temperature-dependent competition of hole excitation to higher energy confined states or to the

wetting layer is at the origin of the observed dependence of $\tau_X$ with temperature. More information about temperature effects on the QD dynamics will be given in chapter §6.2.

# References


[1] C. Pryor, M.-E. Pistol, and L. Samuelson, Phys. Rev. B **56**, 10404 (1997)

[2] M. Bayer, O. Stern, A. Kuther, and A. Forchel, Phys. Rev. B **61**, 7273 (2000).

[3] A. Narvaez, G. Bester, A. Franceschetti, and A. Zunger, Phys. Rev. B **74**, 205422 (2006).

[4] S. F. Yoon, P. Y. Lui, H. Q. Zheng, Mat. Sc. and Eng. B 76, pp.101-106 (2000)

[5] M. Wimmer, S. V. Nair and J. Shumway, Phys. Rev. B 73, 165305 (2006)

[6] G. Bacher, R. Weigand, J. Seufert, V. D. Kulakovskii, N. A. Gippius, and A. Forchel, Phys. Rev. Lett. 83, Nº 21, pp. 4417-4420 (1999)

[7] M. Sugawara, Phys. Rev. B 51, 10743 (1995)

[8] G. Shu, C. Wang, J. Wang, J. Shen, R. Hsiao, W. Chou, J. Chen, T. Lin, C. Ko and C. Lai, Nanotechnology 17, pp. 5722–5725 (2006)

[9] D. Bimberg, M. Grundmann, N. N. Ledenstov, "Quantum *Dot Hetero-structures*", Jonhm Wiley & Sons (2001)

[10] R. Hostein, A. Michon, G. Beaudoin, N. Gogneau, G. Patriache, J.-Y. Marzin, I. Robert-Philip, I. Sagnes, and A. Beveratos, Appl. Phys. Lett. 93, 073106 (2008)

[11] Y. Sakuma, T. Usuki, and Y. Masumoto, Phys. Rev. B 76, 205317 (2007)

[12] J. Seufert, M. Scheibner, G. Bacher, A. Forchel, S. Lee, M. Dobrowolska and J.K. Furdyna, Phys. Stat. Sol. (b) 229, 2 (2002).

[13] O. Labeau, P. Tamarat, and B. Lounis, Phys. Rev. Lett. 90, 257404 (2003).

[14] J. Puls and F. Henneberger Phys. Stat. Sol. (a) 164, 499 (1997).

[15] F. Pulizzi, A. J. Kent, A. Patanè, L. Eaves, and M. Henini, Appl. Phys. Lett. 84, 3046 (2004).

[16] Wolfgang-Michael Schulz, Robert Roßbach, Matthias Reischle, Gareth J. Beirne, Michael Jetter, and Peter Michler, Phys. Status Solidi C 6, No. 4, 906–909 (2009)

# Chapter 5

# Many-Body Effects in Quantum Dots

The Coulomb interaction between carriers inside a crystal lattice is responsible for many-body effects, which affect the electronic structure and optical properties of the material. One of the most ubiquitous manifestations of many-body effects in semiconductors is the fundamental energy gap lowering by increasing the free-carrier density. This effect is due to correlation and exchange contributions of the free carriers to the band structure [1-3]. In consequence, energy bands shift towards lower or higher energies, and the band gap "renormalizes" causing a red-shift in the emission spectrum. This phenomenon is called *band-gap renormalization* (BGR) and its influence on the band structure has been investigated in bulk semiconductors [1], quantum wells (QW) [4-7] and wires (QWR) [8-11]. BGR was observed in non-resonantly excited QD-*ensembles* at high excitation powers [12,13], and in single QDs coupled to a degenerate electron gas by Coulomb interaction or tunnelling [14,15].

In this chapter a red-shift of exciton emission-energy associated to BGR will be reported for *single* InP/GaInP QDs. A continuous and systematic energy red-shift of the PL exciton emission is observed for increasing excitation energies and intensities. In addition, emission-energy minima appear with a one-to-one correspondence to emission intensity maxima in the PLE spectrum as a function of the excitation energy. Hybridization of the QD excited states to the wetting layer (WL) continuum [16,17] will be discussed as a possible origin of the observed BGR phenomenon.

## 5.1 Exciton Red-Shift in InP/GaInP QD

The *micro*-PL spectra of a typical single InP/GaInP QD are plotted in Figure 5.1 for increasing excitation energy ($E_{exct}$). The spectra were taken for energies in

the range between 1.92 eV and 1.95 eV with 3.0 meV steps. There are two discrete lines corresponding to the neutral exciton ($X^0$) and neutral biexciton ($XX^0$). Both $X^0$ and $XX^0$ energies ($E_{PL}$) show a clear decrease for increasing $E_{exct}$. The total energy decrease of $XX^0$ in this excitation range is approximately one half of the $X^0$ one. This $E_{PL}$ decrease is better observed in Figure 5.2, where $X^0$ emission energy (red dots) vs. excitation energy is plotted together with PLE spectrum (black dots). As the PLE signal increases, corresponding to increasing light absorption, a continuous red-shift of the $X^0$ line is observed. By moving the excitation energy closer to the $X^0$ emission, a similar plot displays sharp peaks in the PLE spectrum. Figure 5.3 shows PLE spectrum (black dots) for energies between 20 and 40 meV above the $X^0$ emission energy. There are several discrete lines, corresponding to absorption transitions involving excited states of the QD. Whether these excited states are phonon-assisted absorption peaks or pure electronic transitions (between p-states) is not relevant for the present discussion. Thus, these states will be simply called *p-states*. The most remarkable fact in Figure 5.3 is the systematic appearance of weak but clear dips in the exciton luminescence energy at the energies of the PLE peaks, i.e. whenever the population probability of the QD excited states increases. These dips are also visible in Figure 5.2 below the WL absorption edge.

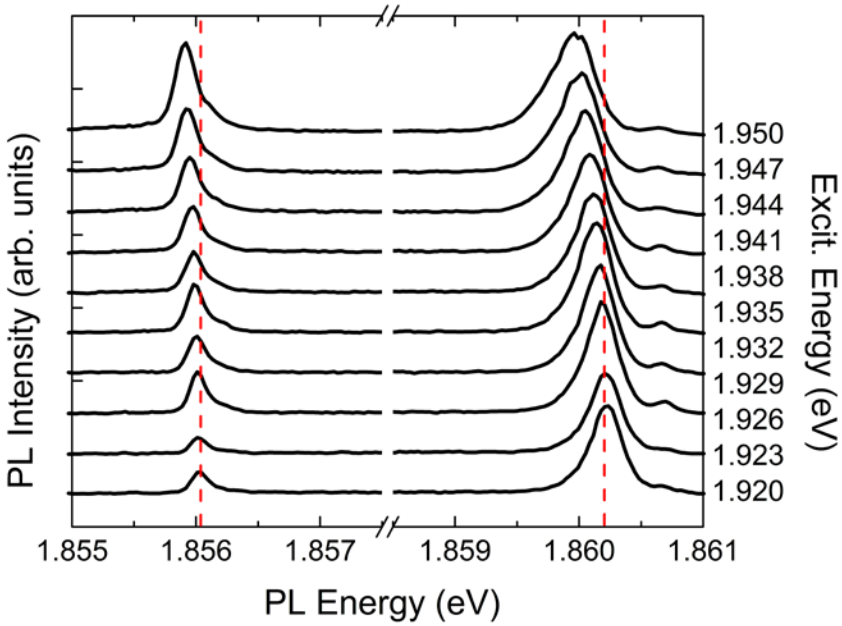


Figure 5.1 PL spectra of a single QD measured at 8K with 23 kW/cm$^2$ excitation power. The spectra are plotted for several excitation energies. The spectra are vertically shifted for clarity. A red-shift of $X^0$ and $XX^0$ lines is observed as the excitation energy increases.

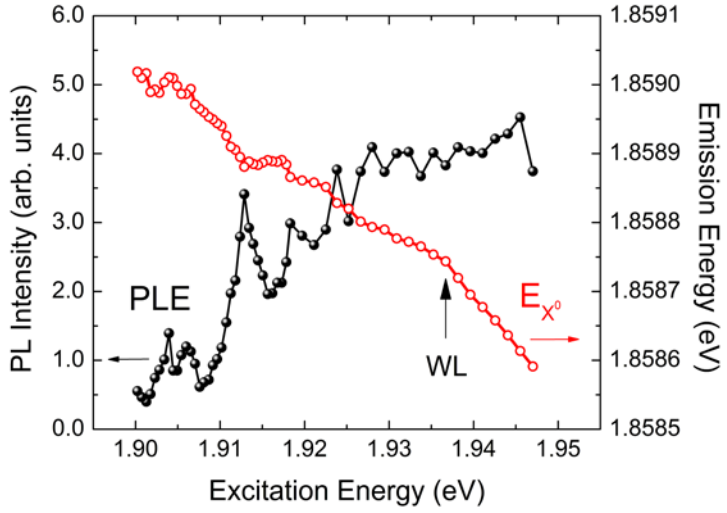


Figure 5.2 PLE spectrum (black circles) and $X^0$ emission energy vs. excitation energy (red circles) of a single QD. The drop of $X^0$ energy with increasing excitation energy is subtle but systematic. Above the wetting layer the red-shift is even more pronounced indicating stronger band-gap renormalization.

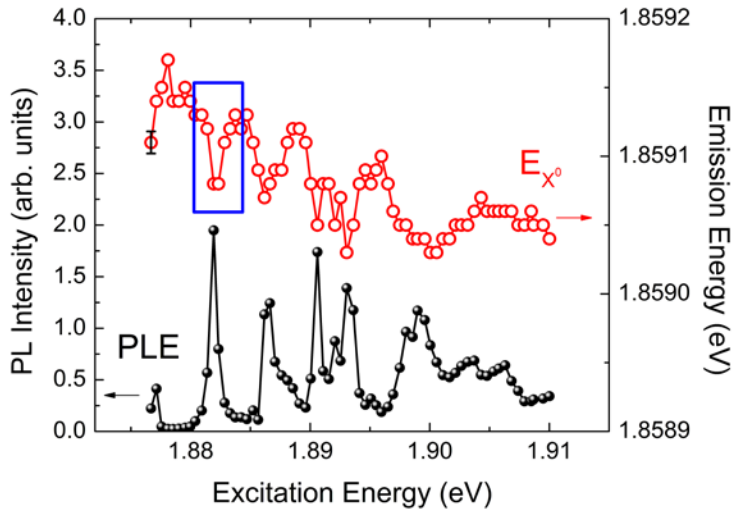


Figure 5.3 PLE spectrum (black dots) and $X^0$ emission energy (red dots) vs. excitation energy for a single QD. The spectra were taken for excitation energies between 20 and 40 meV above the $X^0$ energy. The PLE peaks corresponding to QD p-states coincidence with the $E_{PL}$ red-shift minima due to increased absorption and resulting band-gap renormalization. The resolution in the emission energy is indicated by error bars, the excitation energy has been measured with a resolution of 0.2 meV.

The emission intensity maxima in the PLE spectrum appear in the one-to-one correspondence to the $E_{PL}$ minima, i.e. whenever the light absorption (and the population of carriers in the excited states) increases. The exciton red-shift becomes even more pronounced for excitation energy above the wetting layer (WL) absorption edge (marked by an arrow in Figure 5.2). This indicates that free carriers photo-created in the WL play an important role in the observed red-shift. The red shift observed in Figures 5.1 to 5.3 is interpreted in terms of BGR, whose origin is discussed in the next section.

## 5.2 Hybridization of QD Excited States with WL Continuum

The possible origin of the observed $E_{PL}$ red-shift in Figures 5.1 – 5.3 can be discussed in terms of BGR due to exchange and correlation effects of photo-created carriers in the excited QD states. Note that extra carriers, present in the QD lowest state (s-state) together with $X^0$, lead to the formation of charged excitons ($X^{1\pm}$), neutral and charged biexcitons ($XX^0$, $XX^{1\pm}$), etc. The additional carriers trapped inside the QD produce discrete energy jumps and splittings (i.e. fine structure splitting $\Delta_{FS}$) in the emission lines in the meV range [18-21], which depend on the QD shape, strain, etc. The appearance of new emission lines occurs even for high occupancies [22]. Also, if electron-hole pairs are present in the p-states, the optical spectrum of the QD changes from a few discrete lines to a rich manifold [18,23,24].

Increasing excitation intensity and the resulting high occupation inside QDs were indicated as the origin of the continuous red-shift of the ground state emission in InAs/GaAs QD ensembles [12,13]. However, in a single QD this carrier-population increase would cause discrete energy changes of a few meV in the emission spectrum. Thus, the continuous red-shift observed in single InP/GaInP QDs is not likely to be due to the direct influence of excited carriers *inside* the QD. Other explanation for the observed BGR could be the existence of excited states of neighbouring larger QDs present in the same spectral region of the exciton emission. Larger QDs could couple to the actual QD and alter its energy level but the probability for this coupling to occur is low, as the average inter-QD distance in our sample is low (approximately 0.2 μm). However, this kind of coupling cannot be completely excluded.

Since neither the extra carriers inside the QD nor the inter-QD coupling are likely to cause the QD “gap” renormalization, we consider hybridization of the QD excited states with a continuum [16] as the possible origin of the BGR. Let us consider a QD with two carriers in a p-state after quasi-resonant excitation at this particular energy. This configuration has the same total energy as the configuration, in which one of the carriers relaxes to the lower s-state, while the other passes to

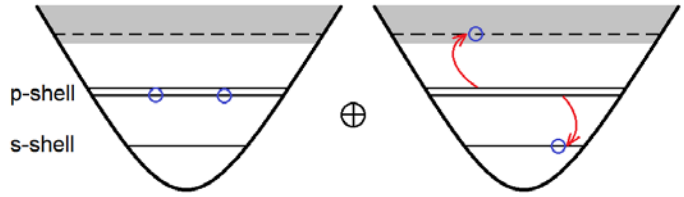


Figure 5.4 The admixture of the p-state and the two-dimensional wetting layer. In consequence, the QDs excited states have partially extended nature.

the near continuum. Both configurations are depicted in Figure 5.4. Coulomb interaction will produce their admixture to form eigenstates of the QD, which have partially discrete and partially extended nature. This hybridization would enable the BGR of the QD, in a similar way as in bulk or QW and QWR systems.

In the case of the InP/GaInP QD sample the WL is the only candidate to hybridize with the QD excited states in our case, as no doping is present in our simple. The hybridization of the QD excited states with WL can occur via one of the two possible types of coupling: dipole-dipole interaction or tunneling. The dipole-dipole coupling between the QD excited states and the WL continuum seems to be the most probable origin of the BGR in our case, since the distance between the QD centre and the WL states is quite short (~1 nm). At this small distance dipole-dipole interaction is expected to overcome tunnelling rate. This kind of hybridization has been reported in self-assembled InAs/GaAs QDs to explain the strong emission by cavity modes in QD-microcavity systems, even for large QD-cavity energy detuning [17]. Note that the small size of the InP/GaInPQDs brings the excited states (especially the holes' ones [25,26]) close in energy to the wetting layer, enabling this kind of hybridization. Moreover, since the biexciton has zero total angular momentum, one would expect less hybridization with the WL, as is reflected in its smaller red-shift (see Figure 5.1).

Additionally, the QD PL spectra were measured as a function of excitation power. Figure 5.5 displays the exciton emission line for excitation power densities ranging from 38 to 190 kW/cm$^2$ and excitation energy resonant at the p-shell (black symbols and red fit lines). The PL spectrum of the QD excited off-resonantly is presented for comparison (blue dots and black fit line). The spectra have been vertically offset and the lower ones magnified for a better display. Again red-shift $\Delta$ is observed which varies almost linearly with the excitation power (see inset of Figure 5.5). Since no significant variation of the line width or the intensity normalized to the excitation power are observed, one can safely exclude sample

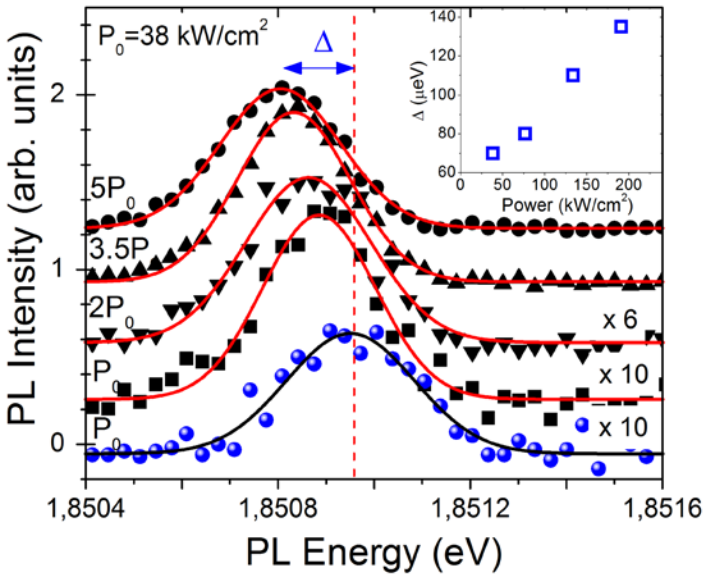


Figure 5.5 PL spectra of $X^0$ for off-resonance (blue dots) and on-resonance with the p-shell (black symbols) excitation measured for different excitation power values. The spectra are vertically off-set for clarity. The red-shift is observed for higher excitation powers. The in-set graph shows the total displacement (Δ) of the PL peak from the off-resonant $X^0$ position.

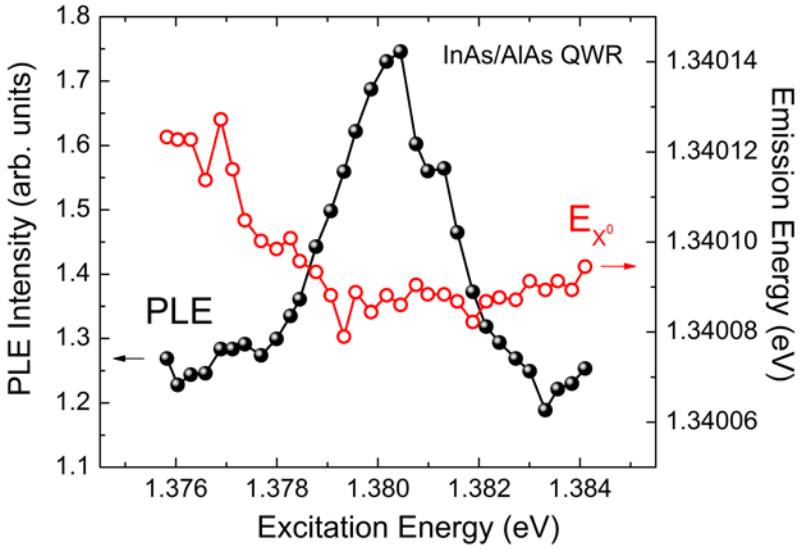


Figure 5.6 PLE spectrum (black circles) and $X^0$ emission energy vs. excitation energy (red squares) of a single InAs/GaAs QR. The description of the sample composition and growth process can be found in Ref. 28. The decrease of $X^0$ energy with increasing PL intensity is subtle but visible.

heating as the origin of the red-shift. Instead, higher population probability of the excited state together with its coupling to the WL states results in lowering the energy states confined inside the dot. This confirms our interpretation of the red-shift as due to BGR caused by hybridization of the QD excited states with the wetting layer.

The exciton red-shift has been observed in 80% of the studied InP/GaInP QDs. The natural question is whether BGR occurs also in other QDs with different composition. To the best of our knowledge, it has not been reported in the most common InAs/GaAs QD system. In fact, we do observe a similar but weaker effect in InAs quantum rings with GaAs barriers described in detail in Ref. 27 (see Figure 5.6). The conclusion is that BGR should occur in most of the QD systems grown by the Stransky-Krastanov method (i.e. having a wetting layer) although in cases of poor QD-WL hybridization it might be too weak to be detected.

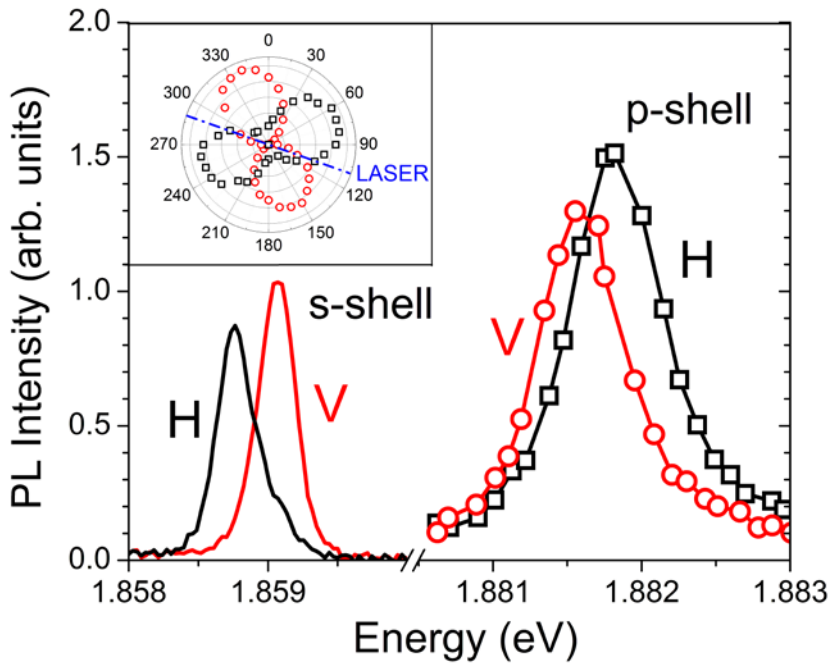


Figure 5.7 PL and PLE spectra of a single QD. The red and black lines represent vertical (V) and horizontal (H) polarization, respectively. Fine structure splitting ($\Delta_{FS}$) is observed for both s- and p-shell. $\Delta_{FS}$ is approximately 300 and 250 μeV for s- and p-state, respectively. (*Inset*) Polar plot for two polarization components of the $X^0$; the laser polarization is marked by a blue dashed line. Excitation energy: $E_{exct}$ = 1.8815 eV.

## 5.3 Fine-Structure Splitting-Modulation

In this section the polarization properties of the BGR in InP QDs will be described. Typical micro-PL spectra of a single QD for horizontal (H) and vertical (V) linear polarization in the low energy range are shown in Figure 5.7. The fine structure splitting ($\Delta_{FS}$) of the neutral exciton emission (300 μeV) is clearly seen. The splitting is due to QD anisotropy either in shape or in piezoelectric field [20,21]. The excited state at 1.882 eV, marked with a rectangle in Figure 5.3, also has a polarization splitting (250 μeV), which is observed in the PLE spectra on the right hand side of Figure 5.7. Note that the $\Delta_{FS}$ signs in the s- and p-states are opposite in this particular dot.

Figure 5.8 (a) represent a high resolution, polarization resolved record of the $X^0$ BGR around the same excited state. The $X^0$ red-shift of both polarization components is plotted vs. excitation energy. To equally populate the V and H split levels of the p-state, the excitation light was linearly polarized at 45º from V and H polarization components. Note that the maximum red-shift of the V and H components of the $X^0$ emission occurs at different excitation energies.

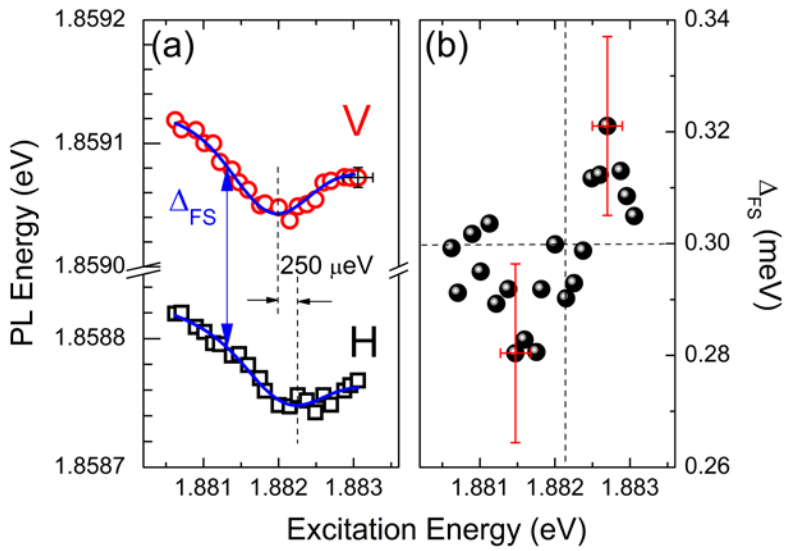


Figure 5.8 (a) Two polarization components of the $X^0$ emission energies vs. excitation energy. $X^0$ energy minima in V and H polarizations coincide with PLE maxima in p-shell (Figure 5.6). (b) $\Delta_{FS}$ of the s-state vs. excitation energy. The horizontal line represents the splitting for excitation not resonant with the p-shell. The variation around the non-resonant value is a consequence of the different positions of the $X^0$ energy minima in (a). The energy resolutions are indicated by error bars in (a) and (b).

These energies are separated by 250 μeV and correspond to the energies of their respective PLE maxima. The conclusion is that the energy distance between the two polarization components (s-shell $\Delta_{FS}$) varies with the excitation energy due to different energy values of the emission BGR maxima (p-shell $\Delta_{FS}$). The expected behaviour of the s-shell $\Delta_{FS}$ in this particular QD is: (i) to decrease when V polarization component of $X^0$ starts red-shifting, (ii) to recover its original value for an excitation energy corresponding to the midpoint (1.882 eV) of the PLE doublet, (iii) to continue increasing as the H exciton red-shifts and the V exciton blue-shifts back, and finally (iv) to recover its original value when both exciton components are non-resonantly excited.

The fine structure splitting of the s-state vs. excitation energy is plotted in Figure 5.8 (b). The expected modulation in $\Delta_{FS}$ is observed and its amplitude is $\pm$ 20 μeV, what corresponds to around 10% of the total fine structure splitting for the excitation not resonant with the p-shell. The question at this point is whether this polarization dependent BGR could be increased enough to become an alternative method to suppress $\Delta_{FS}$ for entangled photon pair production [28,29]. The obvious advantage over other methods of controlling $\Delta_{FS}$ (external magnetic or electric fields, elastic strain modulation or post-growth thermal annealing), is that polarization dependent BGR is a reversible process requiring only optical access to the sample. However, it is not clear whether a total cancellation of $\Delta_{FS}$ is possible by this method. The required conditions for a total cancellation or even sign reversal of $\Delta_{FS}$ would be a large polarization splitting of the p-state and a small one for the s-state. This would correspond to bringing the two curves in Figure 5.8 (a) closer together in vertical direction, while increasing the horizontal separation between their minima, until they cross each other. Such a condition could eventually be fulfilled by QDs with adequate shape and strain [20,21]. A simple argument to support this possibility is the fact that p-states are more extended laterally than s ones along the crystallographic axes, which in turn determines the polarization directions of the exciton fine structure doublet. Consequently, p-states should be more sensitive than the s-states to the QD anisotropy. Actually, an increasing hole p-state splitting has been reported for pyramidal QDs with increasing lateral size due to the piezoelectric potential [23].

# References

[1] W. F. Brinkman and T. M. Rice, Phys. Rev. B 7, 4, pp. 1508 – 1523 (1973)

[2] T.M. Rice, in Solid State Physics, edited by H. Ehrenreich, F. Seitz and D. Turnbull (Academic, New York, 1977) Vol.32, p.1-86, and references therein.

[3] G. Beni and T. M. Rice, Phys. Rev. B 18, 2, pp. 768 – 785 (1978)

[4] S. Schmitt-Rink, C. Ell, S. W. Koch, H. E. Schmidt and H. Haug, Solid State Communications **52**, 123 (1984).

[5] A. Pinczuk, Jagdeep Shah, H. L. Störmer, R.C. Miller, A. C. Ggossard and W. Wiegmann, Surface Science **142**, 492 (1984).

[6] D. A. Kleinman and R.C. Miller, Phys. Rev. B **32**, 2266 (1985).

[7] G. Tränkle, H. Leier, A. Forchel, H. Haug, C. Ell and G. Weimann, Phys. Rev. Lett. **58**, 419 (1987).

[8] W. Wegscheider, L. N. Pfeiffer, M. M. Dignam, A. Pinczuk, K. W. West, S. L. McCall and R. Hull, Phys. Rev. Lett. **71**, 4071 (1993).

[9] R. Ambigapathy, I. Bar-Joseph, D. Y. Oberli, S. Haacke, M. J. Brasil, F. Reinhardt, E. Kapon, and B. Deveaud, Phys. Rev. Lett. **78**, 3579 (1997).

[10] F. Rossi and E. Molinari, Phys. Rev. Lett. **76**, 3642 (1996).

[11] B. Alén, D. Fuster, G. Muñoz-Matutano, J. Martínez-Pastor, Y. González, J.Canet-Ferrer and L. González, Phys. Rev. Lett. 101, 067405 (2008).

[12] Z. L. Yuan, E. R. A. D. Foo, J. F. Ryan, D. J. Mowbray, M. S. Skolnick, and M. Hopkinson, phys. stat. sol. (a) **178**, 345 (2000).

[13] R. Heitz, F. Guffarth, I. Mukhametzhanov, M. Grundmann, A. Madhukar, and D. Bimberg, Phys. Rev. B **62**, 16881 (2000).

[14] Joo In Lee, Hyung Gyoo Lee, Eun-joo Shin, Sungkyu Yu, Kasi Viswanath, Dongho Kim, and Gukhyung Ihm, Mat. Sci. Eng. B **51**, 122 (1998).

[15] N. A. J. M. Kleemans, J. van Bree, A. O. Govorov, J. G. Keizer G. J. Hamhuis, R. Nötzel, A. Yu. Silov and P. M. Koenraad, Nature Physics **6**, 534 (2010).

[16] K. Karrai, R.J. Warburton, C. Schulhauser, A. Hoegele, B. Urbaszek, E. J. McGhee, A.O. Govorov, J.M. Garcia, B.D. Gerardot and P.M. Petroff, Nature **427**, 135 (2004).

[17] M. Winger, T. Volz, G.Tarel, S. Portolan, A. Badolato, K.J. Hennessy, E.L. Hu, A. Beveratos, J. Finley, V. Savona, and A. Imamoglu, Phys. Rev. Lett. **103**, 207403 (2009).

[18] M. Bayer, O. Stern, P. Hawrylak, S. Fafard, and A. Forchel, Nature, **405**, 923 (2000).

[19] R. J. Warburton, C. Schäflein, D. Haft, F. Bickel, A. Lorke, K. Karrai, J. M. Garcia, W. Schoenfeld, and P. M. Petroff, Nature, **405**, 926 (2000).

[20] M.Grundmann, O. Stier and D. Bimberg, , Phys. Rev. B **52**, 11969 (1995).

[21] G. A. Narvaez, G. Bester, and A. Zunger, Phys. Rev. B **72**, 245318 (2005).

[22] A. Wojs and P. Hawrylak, Phys. Rev. B **55**, 13066 (1997).

[23] V. Mlinar and A. Zunger, Phys. Rev. B **80**, 205311 (2009).

[24] D. V. Regelman, U. Mizrahi, D. Gershoni, and E. Ehrenfreund, W. V. Schoenfeld and P. M. Petroff, Phys. Rev. Lett. **87**, 257401 (2001).

[25] A. K. Nowak, E. Gallardo, D. Sarkar, H. P. van der Meulen, J. M. Calleja, J. M. Ripalda, L. González, and Y. González, Phys. Rev. B **80**, 161305(R) (2009).

[26] C. Pryor et al. Phys Rev B 65, 10404 (1997)

[27] E. Gallardo, L .J. Martínez, A. K. Nowak, D. Sarkar, H. P. van der Meulen, J. M. Calleja, C. Tejedor, I. Prieto, D. Granados, A. G. Taboada, J. M. García and P. A. Postigo, Phys. Rev. B **81**, 193301 (2010) and references therein.

[28] N. Akopian, N. H. Lindner, E. Poem, Y. Berlatzky, J. Avron, D. Gershoni, B. D. Gerardot and P. M. Petroff, Phys. Rev. Lett. **96,** 130501 (2006).

[29] R. M. Stevenson, R. J. Young, P. Atkinson, K. Cooper, D. A. Ritchie and A. J. Shields, Nature, **439**, 178 (2006).

# Chapter 6

# Single Photon Emission by InP Quantum Dots

This chapter addresses the properties of single photon emission by single InP quantum dots and the underlying mechanisms. The general issues of single photon emission measured by photon correlation spectroscopy will be presented in section §6.1. The experimental results on InP/GaInP QDs will be shown in section §6.2, where the influence of external and intrinsic effects on single-photon emission will also be discussed.

## 6.1. General considerations

Semiconductor quantum dots (QDs) belong to a group of the most promising systems for emitting single photons "on demand". The interest in single photon emitters (SPE) relies in their potential application in quantum information technologies. In comparison to other SPE, i.e. atoms or ions, semiconductor QDs are easy to use, flexible to design and scalable [1-4]. Their main drawbacks are the short decoherence time compared to atoms and the variability of their properties depending on their size, composition, strain and electrostatic environment. Newly developed technologies of nanostructures growth and spectroscopy give the possibility to study the optical emission of a single QD, and the coupling of the QD excitons to confined electromagnetic modes by precise positioning of the QD inside a photonic cavity [2,5,6].

InP/GaInP QDs have been intensively investigated in the last two decades as good candidates for SPE in the visible range [7-13]. Photon correlation experiments have been reported for these QDs under pulsed [8,10,12] and continuous [7,9] optical excitation, as well as under electrical injection [11]. All the published experimental results of the second order photon correlation function $g^{(2)}(\tau)$

measured in InP QDs present clear antibunching with low values of $g^{(2)}(0)$ (between 0.1 and 0.2 [7-12]) indicating efficient single photon emission.

From a practical point of view it is important to operate the SPE at relatively high temperature. The antibunching dip was observed at room temperature in CdSe/ZnS QDs [1], up to 200K in GaN QDs [14] and up to 90K in InGaAs/AlGaAs QDs [15]. In unstrained InP QDs (with Al containing potential barriers) the upper temperature limit was 80K [10]. As the temperature increases the $g^{(2)}(0)$ value rises as a consequence of the background luminescence. The temperature also influences the antibunching time $\tau_R$. In fact $\tau_R$ depends on many factors as pumping rate, exciton life time and carrier relaxation time from excited states. Some of these factors are temperature dependent. The $\tau_R$ increase with temperature has been reported in InGaAs/AlGaAs QDs [15].

Photon correlation in semiconductor QDs has been also studied under different excitation conditions: non resonantly above the WL [2,16,17], quasi-resonantly at one of the excited states [3,18], or resonantly at the neutral exciton ground state [19]. The excitation below the WL continuum favours relaxation of electron-hole pairs inside the QD compared to individual carrier relaxation, reducing the number of created carriers in the vicinity of the QD. In turn, excitation in the excited states increases absorption and favours the formation of electron-hole pairs within potential barriers of the dot. For QDs excited quasi-resonantly at one of the excited states $g^{(2)}(0)$ is less than 0.03 [3,18,20], what indicates very efficient single photon emission.

The single photon emission on demand is conditioned by background photons and decoherence of the optical transitions. The optically induced coherence between two states (i.e. exciton $|X\rangle$ and ground sate $|e\rangle$) degrades over time by two mechanisms [21]: i) The amplitude of either state could vanish due to inelastic relaxation processes to a different state in the quantum system (relaxation or recombination), and ii) Elastic scattering (i.e. by phonons) leading to a change of the relative phase between the two states but without decay of the individual probability amplitudes. This is known as pure dephasing. The second mechanism introduces random change in phase, producing rapid decoherence, despite the long life times for both states.

In bulk semiconductors and quantum wells (QW) pure dephasing by phonon-exciton or exciton-exciton interaction dominate even at low temperatures. However, in single QDs the pure dephasing is highly reduced due to the QD discrete density of states, which diminishes the elastic scattering probability of excitons by phonons. Besides, the isolation of the single dot reduces scattering with

uncorrelated excitons what leads to relatively long-lived coherence. One of the possible origins of decoherence within the QD is a random transition between bright (BX) and dark (DX) exciton states with the total angular momentum ±1 and ±2, respectively [22]. The influence of this transition on the QD optical coherence will be discussed in section §6.2.2.

## 6.2. External and Intrinsic Effects on Single-Photon Emission

The micro-PL spectra of three selected QDs are shown in Figure 6.1. Each QD has three emission lines corresponding to: exciton ($X^0$), charged exciton ($X^-$) and biexciton ($XX^0$). The assignment is done by their dependence on excitation power and their linear polarization (see chapter §4.2). Clear differences in the biexciton binding energy ($E_b^{XX}$) and the fine structure splitting ($\Delta_{FS}$) are observed between the QDs. For QD3 the energy $E_b^{XX}$ is larger and the splitting $\Delta_{FS}$ is smaller than for the QD1 and QD2. This suggests weaker electron-hole exchange energy in QD3. As the exchange energy depends on the overlap of the electron and hole wave functions, we deduce that QD3 must be larger in height than the other dots [23], which is consistent with its lower emission energy. Moreover, the decay times ($\tau_X$) for QD2 and QD3 obtained in the TRPL measurements (~0.4 ns and ~0.2 ns, respectively) clearly support the conclusion that QD2 is smaller than QD3 (see §4.3) [24].

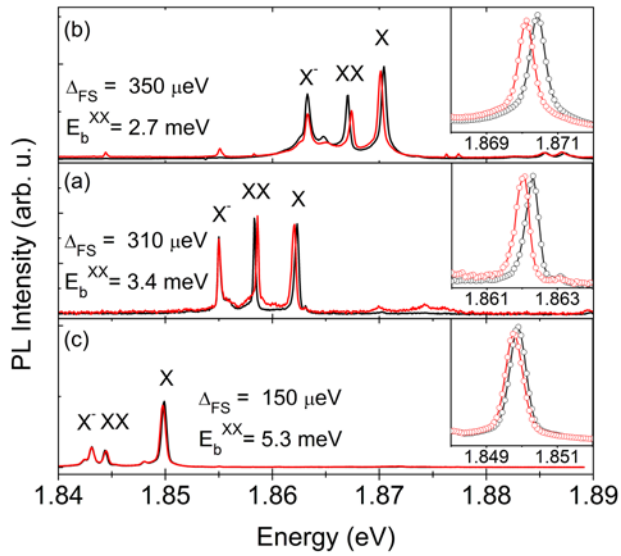


Figure 6.1 Micro-PL spectra of the three QD under study: (a) QD1, (b) QD2, and (c) QD3. The red and black lines represent the orthogonal polarizations H, V. The differences in $E_b^{XX}$ and $\Delta_{FS}$ indicate different dot sizes. Right panels display $\Delta_{FS}$ of X lines in an enlarged scale.

The second order correlation function $g^{(2)}(\tau)$ was measured for the three QDs. The auto- and cross-correlation functions of the different emission lines of QD2 are presented in Figure 6.2. Figures 6.2 (a), (c) and (d) show the measured auto-correlation functions $g_{meas}^{(2)}(\tau)$ of $X^0$, $X^{1-}$ and $XX^0$, respectively. The $XX^0$-$X^0$ cross-correlation is shown in Figure 6.2 (b). All the measurements were taken at temperatures below 13K. In the autocorrelation measurements of $X^0$ the antibunching appears at zero delay time. A similar behaviour is observed for the charged exciton $X^{1-}$, though not so pronounced due to high signal-to-noise ratio (S/N). Both antibunching and bunching are observed in the $XX^0$-$X^0$ cross-correlation experiment for delays close to zero. The bunching observed in Figure 6.2 (b) for positive delay time ($\tau>0$) evidences the photon cascade from the QD. The recombination from the biexciton to the exciton state ($XX^0$-$X^0$) precedes the transition from the exciton to the ground state ($X^0$-G). The probability of the inverted process is very low, as the QD needs certain time to capture two electron-hole pairs to form the following biexciton state. Thus, the antibunching appears in the negative delay axis ($\tau<0$). No antibunching was registered in the $XX^0$ autocorrelation function. Shorter recombination time (see chapter §4.3) implies narrower antibunching.

The temperature dependence of $g^{(2)}(\tau)$ was studied for the selected QDs excited non resonantly above the WL. The temperature was varied between 5K and 45 K. Figure 6.3 shows the $X^0$ auto-correlation function measured for QD2 at two different temperatures. There are clear antibunching minima in the auto-correlation plots, indicating single photon emission even at higher temperatures. Due to relatively long response time of the experimental set-up ($\tau_{IRF}$ = 350 ps), the measured antibunching deep suffers broadening which increases antibunching time $\tau_R$ and $g^{(2)}(0)$. The real $\tau_R$ and $g^{(2)}(0)$ are obtained in the deconvolution fitting procedure. The solid (dashed) lines in the Figure 6.3 are theoretical fits to Eq. 3.7 for $g^{(2)}(\tau)$ convoluted (not convoluted) with the instrumental response function $h(\tau)\sim\exp(-|\tau|/\tau_{IRF})$ [11]. The values of the measured $g^{(2)}{}_{meas}(0)$ and real $g^{(2)}(0)$ for the three QDs are shown in Table 6.1.

The $g^{(2)}{}_{meas}(0)$ and $g^{(2)}(0)$ values differ essentially due to the broadening effect. The $g^{(2)}{}_{meas}(0)$ error bars were estimated from the noise level in the HBT histogram, and the error bars for $g^{(2)}(0)$ were calculated by least square fit. Note, the $g^{(2)}(0)$ values remain below 0.2 even for high temperatures. The background contribution to the QD emission was less than 2%, so no background correction has been done [26]. The convolution of Eq. 3.7 and $h(\tau)$ function is derived in **Appendix**.

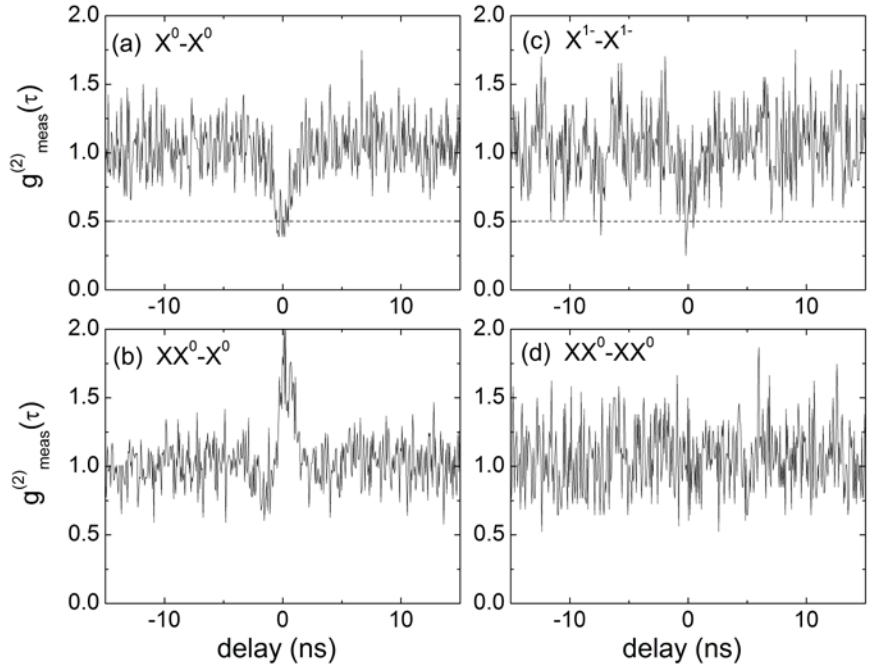


Figure 6.2 Second order correlation function $g^{(2)}_{meas}(\tau)$ measured for different emission lines of QD2: (a) Auto-correlation of the neutral exciton; (b) Cross-correlation between neutral biexciton and neutral exciton; (c) Auto-correlation of the charged exciton; auto-correlation of the neutral biexciton.

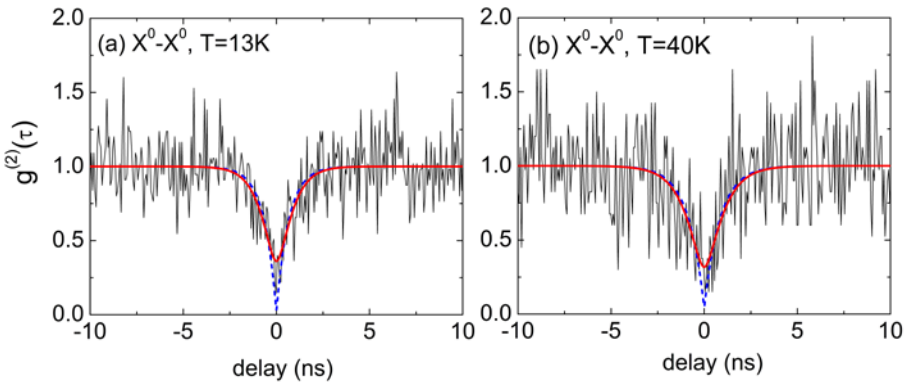


Figure 6.3 $X^0$ auto-correlation function $g^{(2)}(\tau)$ for the QD2 measured at: (a) T=13 K, and (b) T=40 K. The $g^{(2)}(0)$ value and the antibunching time for both temperatures (obtained in the least squares fit with Eq 3.7) are 0.02±0.13, 0.66±0.12 ns (13 K), and 0.04±0.14 and 0.85±0.17 ns (40 K), respectively.

Table 6.1 Comparison of the 2nd order correlation function value at zero delay time at different temperatures (T) for the three QDs. Measured ($g^{(2)}_{meas}(0)$) and real values obtained in the deconvolution fit ($g^{(2)}_{meas}(0)$).

| QD1 | | | QD2 | | | QD3 | | |
|---|---|---|---|---|---|---|---|---|
| T(K) | $g^{(2)}_{meas}(0)$ | $g^{(2)}(0)$ | T(K) | $g^{(2)}_{meas}(0)$ | $g^{(2)}(0)$ | T(K) | $g^{(2)}_{meas}(0)$ | $g^{(2)}(0)$ |
| 7 | 0.41±0.04 | 0.0± 0.1 | 13 | 0.40±0.09 | 0.1± 0.3 | 5 | 0.39±0.03 | 0.1± 0.2 |
| 30 | 0.37±0.05 | 0.0± 0.2 | 25 | 0.40±0.11 | 0.1± 0.3 | 7 | 0.30±0.03 | 0.0± 0.2 |
| 40 | 0.43±0.05 | 0.0± 0.1 | 35 | 0.42±0.14 | 0.2± 0.4 | 20 | 0.28±0.03 | 0.0± 0.2 |
| | - | - | 45 | 0.32±0.13 | 0.1± 0.3 | 30 | 0.32±0.03 | 0.0± 0.2 |
| | | | | | | 40 | 0.40±0.03 | 0.0± 0.2 |

The plot of the antibunching time vs. temperature is shown in Figure 6.4 (right panels) for the three quantum dots. Different temperature trends of $\tau_R$ are observed: while $\tau_R$ increases with temperature for QD1 and QD2, it decreases for QD3. To understand the origin of this difference, we will discuss it together with the PL intensity ratio $I_X/(I_X+I_{XX})$, where $I_X$ and $I_{XX}$ are the exciton and biexciton emission intensities, respectively (Figure 6.4 *left* panels). The measurements were done under low excitation power, so that the $X^0$ intensity was much higher than the $XX^0$ one ($I_{XX} < 0.15\ I_X$). We observe significant differences also in the temperature dependence of the $I_X/(I_X+I_{XX})$ ratio between the dots. The PL intensity ratio rises rather steadily for QD1 and QD2, while for QD3 it is constant up to 40K and then it starts to grow rapidly.

Among the possible mechanisms that influence both $\tau_R$ (i.e. exciton life time, optical pumping rate and others) [27,28] and the intensity ratio $I_X/(I_X+I_{XX})$ one can point out two which are temperature dependent:

i) Dark-to-bright exciton transitions [29,30], and

ii) Thermal excitation of holes [15].

The first one will decrease $\tau_R$ because DX→BX transitions produce bright excitons in addition to those formed directly from relaxation of electron-hole pairs excited at the wetting layer. The second process (characterized by a hole excitation energy $E_h$) will increase $\tau_R$ as the thermal excitation of holes decreases the probability of the $X^0$ recombination to the ground state. As for the PL intensity ratio, both mechanisms will produce an increase: DX→BX transitions enhance $I_X$ with respect to $I_{XX}$, and thermal excitation of holes will reduce the XX occupancy probability (two holes in the ground state) more efficiently than the X occupancy (one hole in the ground state). Depending on the $E_{DB}$ and $E_h$ values, the rise of the intensity ratio will have different origin. In the following sections both processes and their influence on the single photon emission from the QD will be discussed.

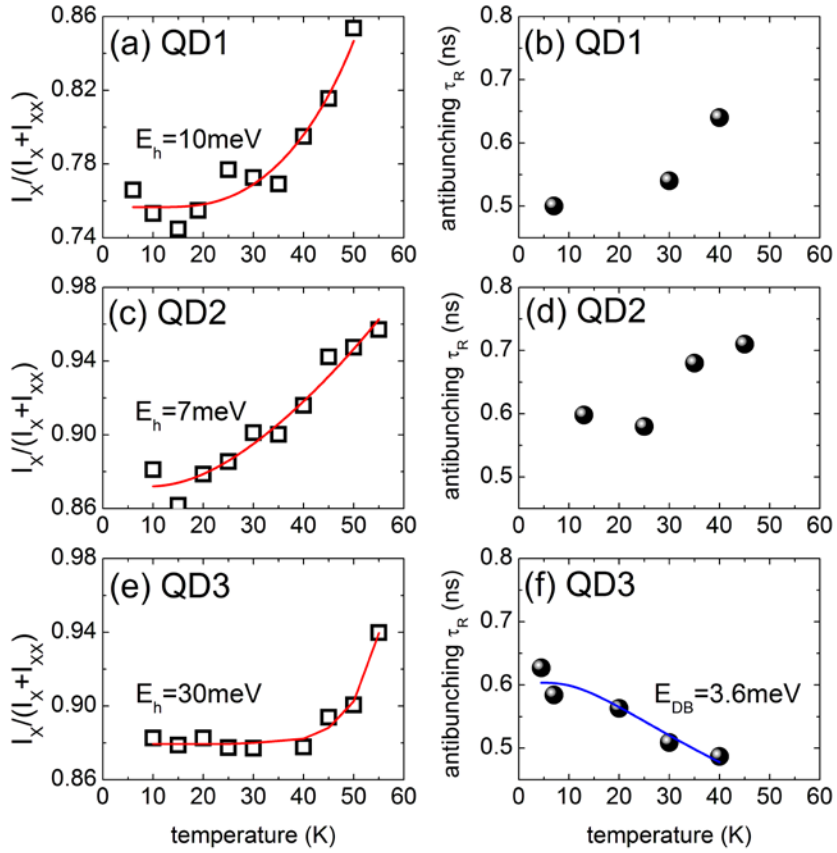


Figure 6.4 Temperature dependence of the $I_X/(I_{XX}+I_X)$ intensity ratio and of the antibunching time $\tau_R$ obtained for QD1 (a)-(b), QD2 (c)-(d), and QD3 (e)-(f), respectively.

### 6.2.1. PL Ratio Dependence

The intensity ratio $I_X/(I_X+I_{XX})$ increase has been reported earlier by Reischle *et al*. [12], and its origin was assigned to the dark-to-bright exciton transition. The DX→BX transition rate depends on the splitting between both states ($E_{DB}$). The energy splitting $E_{DB}$ (as the fine structure splitting) is strongly sensitive to the QD shape and size [23,31,32]. The $E_{DB}$ values in small InP QDs were estimated experimentally to be between 1.4 and 5 meV [12].

A theoretical fit to the PL intensity ratio data (Figure 6.4 *left*) with an Arrheniuns type function: $I(T) \propto \left(1 - C\exp\left(-\Delta E\right)/kT\right)$ gives energy values ΔE in order of tens meV (C is a fitting parameter). This is too much to be DX→BX transition energy. Therefore in our case this mechanism, invoked in Ref. [12], is not

the origin of the PL increase. However, the expected separation between ground and excited hole states is of this order of magnitude. Thus, in principle thermal excitation of holes could explain the trend of $I_X/(I_X+I_{XX})$ vs. temperature. In a rough approximation $E_h$ can be estimated assuming that $I_X$ and $I_{XX}$ decrease with temperature according to equations:

$$\begin{aligned} I_X &= A - BN, \\ I_{XX} &= C - DN, \\ N &= \left( \exp\left( E_h / kT \right) - 1 \right)^{-1}, \end{aligned} \tag{6.1}$$

where A, B, C and D are temperature independent constants, and N is the Bose-Einstein occupation factor of phonons responsible for the thermal excitation of holes. Then the intensity ratio can be expressed as:

$$\frac{I_X}{I_X + I_{XX}} = \frac{1 - aN}{b - cN} \ , \tag{6.2}$$

where $a=B/A$, $b=1+C/A$ and $c=(B+D)/A$. The parameter $b$ is fixed by the low temperature limit ($b>1$, $c>a$). The fit of our data with Eq. (6.2) gives a thermal activation energy $E_h$ equal 10 meV, 7 meV and 30 meV for QD1, QD2 and QD3, respectively (see Figure 6.4 (a), (c) and (e)). These values are of the order of magnitude of the expected hole state splitting in our dots. In InP/GaInP QDs the holes are weakly confined in the potential barriers due to the low valence band off-set. Indeed, the band off-set is negative in strain-free hetero-junctions, and the carriers are confined only by strain (see §4.1) [33]. In the very small InP QDs studied in this thesis one expects only one heavy and light hole state pair confined inside the potential barriers. We have estimated that for a 1 nm high QD, with a square-type potential and 50 meV valence band off-set, the heavy-light hole splitting is approximately 6 meV. If the QD height rises, then the heavy-light hole splitting increases.

### 6.2.2. Antibunching Time.

The photon correlation measurements have been done under very low excitation power ($I_{xx}=0.15I_x$). Under such pumping conditions the biexciton formation probability by direct pumping is low. Thus, biexcitons are mainly formed by "refilling" of dark excitons with an additional *e-h* pair from the WL. Bright excitons can result from three different channels: 1) capture of one electron and one

hole with proper spins directly from the wetting layer, 2) emission of a photon from the biexciton state, and 3) thermally activated spin flip from the dark to the bright exciton state mediated by acoustic phonons [30]. A scheme of these contributions to BX is shown in Figure 6.5 (a). As only the third channel is temperature dependent, the antibunching time can be described as follows:

$$\begin{aligned} \frac{1}{\tau_R} &= \frac{1}{\tau_A} + \frac{1}{\tau_B}, \\ \frac{1}{\tau_B} &= A \cdot \left( \exp\left( E_{DB} \middle/ kT \right) - 1 \right)^{-1}, \end{aligned} \tag{6.3}$$

where $1/\tau_A$ is a combined probability of channels 1) and 2) while $1/\tau_B$ represents channel 3).

The DX→BX transition is assumed to be activated by acoustic phonons with energy close to $E_{DB}$. The temperature trend of $\tau_R$ for the QD3 in the Figure 6.4 (f) can be well described by the Eq. 6.3. The resulting value of $E_{DB}$ is 3.6 meV. This value is substantially higher than in InAs QDs (0.1÷0.3 meV) [34,35], as a consequence of the increased electron-hole interaction exchange energy due to stronger carrier confinement in the small InP QDs studied in Ref. [12] and in this thesis. Values of $E_{DB}$ of order of few meV have been obtained earlier theoretically [36] and experimentally [12] for small InP QDs. The same order of magnitude for $E_{DB}$ has been reported by other authors [37] for CdSe QDs ($E_{DB}$ = 2 meV). In the smaller QDs (QD1 and QD2) we expect an even larger $E_{DB}$ value due to the increased overlap of electron and hole wave functions. On the other hand a smaller hole excitation energy is expected because of the stronger confinement inside the potential barrier (see Figure 6.5 (b)). As a result there are two competing processes activated thermally from which the thermal excitation of holes is dominating ($E_{DB} \geq E_h$). This mechanism explains the rising trend of $\tau_R$ vs. T for QD1 and QD2 (see Figure 6.4 (b) and (d)). Indeed, when the probability of finding a hole in its ground state decreases, then the mean time needed to populate the exciton state (after previous photon emission) increases. For larger QDs (QD3), the ~~DX~~BX process determines the temperature dependence of $\tau_R$ ($E_{DB} < E_h$). A spin flip is then more probable at lower temperatures than the hole excitation process, so the probability of BX population increases. As a consequence a mean time to recharge a QD after previous photon emission gets shorter. Contrary, for smaller QDs (QD1, QD2) the condition $E_{DB} > E_h$ holds and the dominating mechanism at low temperatures is thermal hole excitation. This, as explained, provokes an increase of $\tau_R$ as temperature increases.

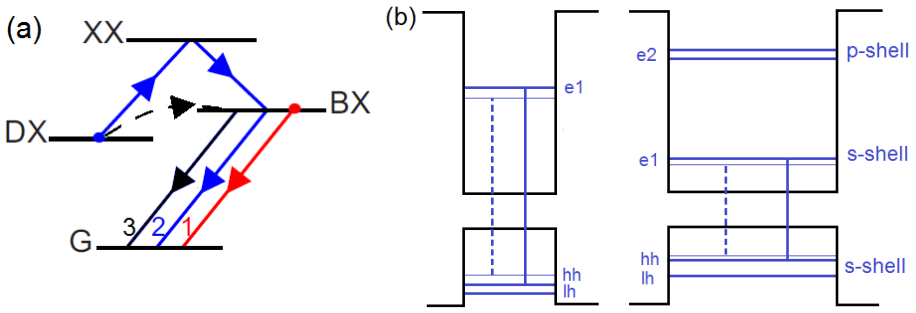


Figure 6.5 (a) Level scheme including: QD ground state (G), DX, BX, and biexciton (XX). The arrows (1, 2, and 3) represent the photon emission of the bright exciton state after three possible ways of charging. (b) Band structure for two QDs with different size. The straight (dashed) line represents optically allowed (forbidden) recombination from the BX (DX) to the ground state.

### 6.2.3. Quasi-Resonant Excitation

To avoid the influence of long relaxation processes and defect charging, which occur when exciting above the QD potential barriers, we have studied single photon emission under quasi-resonant excitation at the QD excited states. This approach should diminish the multi-photon emission probability and increase the quantum efficiency of the single photon emission [3,18,20]. In this section the influence of the quasi-resonant excitation on the dynamics of the QD populating process will be discussed. The memory effect [3,16] due to long-time delays is also discussed.

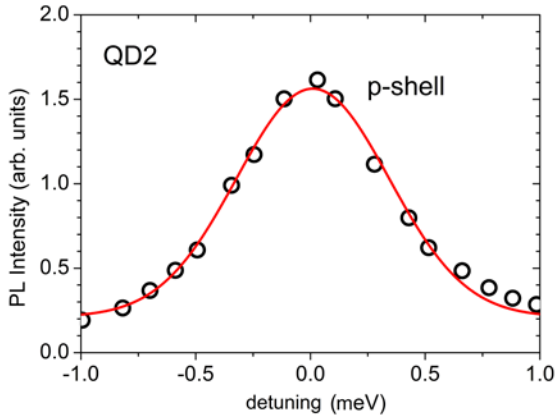


Figure 6.6 High resolution PLE spectrum of the p-shell excited state measured with no polarization selection for neutral exciton ($X^0$) of the QD2. The PLE is plotted as a function of the excitation energy detuning defined by Eq. 6.4. The line is a Gauss fit to experimental points. The FWHM is 0.8 meV.

A high resolution micro-PLE spectrum of the QD2 excited state at 1.882 eV labeled as $E_{p\text{-}shell}$ (marked by a rectangle in the Figure 5.3) is presented in Figure 6.6. The PLE spectrum is plotted as a function of the excitation-energy detuning:

$$\delta = E_{p-shell} - E_{ex}, \tag{6.4}$$

The $X^0$ autocorrelation function was measured for QD2 under quasi-resonant excitation at the p-state. The $g^{(2)}(\tau)$ measurement was run for different values of the excitation power $P_{exct}$ and $\delta$, and without polarization selection of the emission. The $g^{(2)}(\tau)$ plots for three different $\delta$ values are shown in Figure 6.7 for high excitation power (140 kW/cm$^2$). Both antibunching and bunching (at a longer time scale) are observed at all detuning values. The antibunching minima of $g^{(2)}(\tau)$ at zero delay evidences SPE. Although true SPE from a single QD requires $g^{(2)}(0)<0.5$, our measured $g^{(2)}_{meas}(0)$ values (>0.5) are affected by the instrumental response time of the experimental set-up ($\tau_{IRF}$ = 350 ps), as in the previous section, and by the presence of photon bunching at a longer time scale, as observed in Figure 6.7.

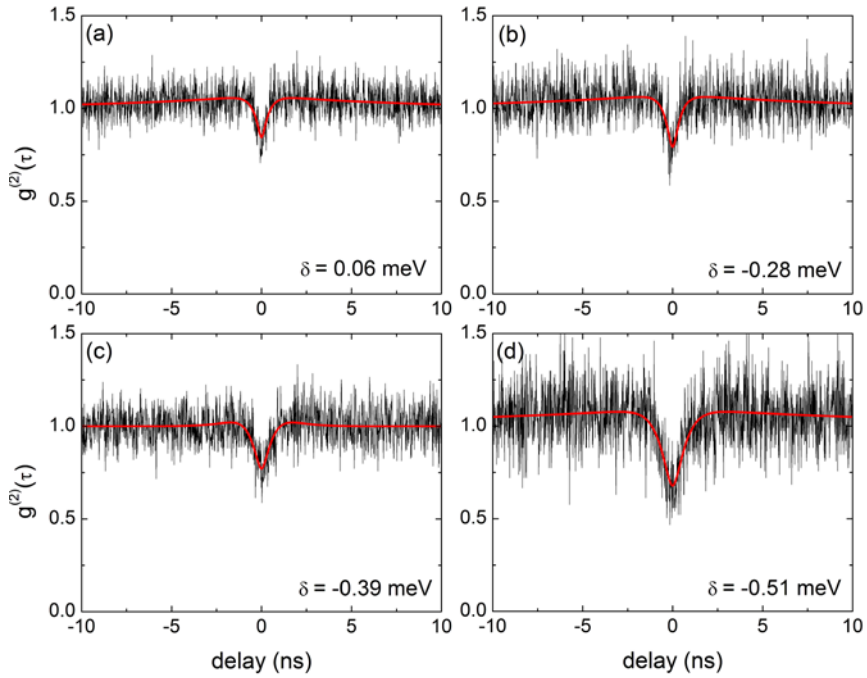


Figure 6.7 $X^0$ auto-correlation functions measured for four detuning values $\delta$. Count rates at the detectors varied from $1.3\times10^4$ cps to $8\times10^4$ cps depending on the the excitation energy. Measurements were taken at 15K with excitation power of 140 kW/cm$^2$, and binning resolution of 64 ps.

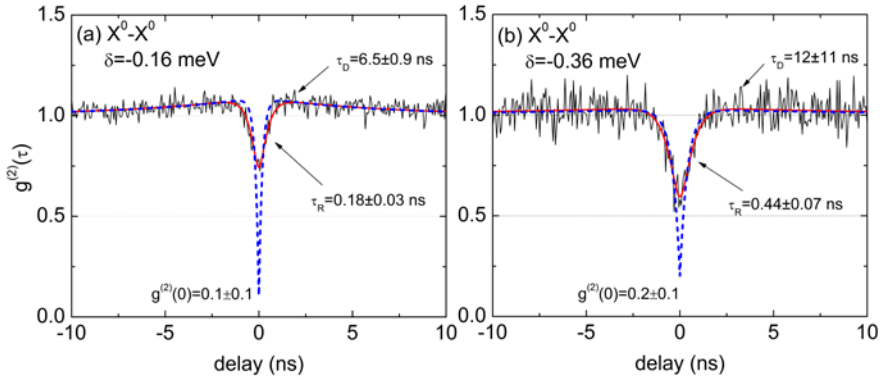


Figure 6.8 $X^0$ auto-correlation functions measured for two detuning value δ. (a) δ = -0.16 meV, count rate $3.8\times10^4$ cps, <C>=1150 coincidences, N/S=0.96; (b) δ = 0.36 meV, count rate $1.3\times10^4$ cps, <C>=310 coincidences, N/S=0.96. Measurements were taken at 15K with excitation power of 60 kW/cm$^2$, and binning resolution of 64 ps.

This bunching appears when the QD occupation probability with an *e-h* pair is higher than average for short delay times after photon emission. Its origin will be discussed afterwards. Under non resonant excitation (above the wetting layer absorption edge) values of $g^{(2)}_{meas}(0)<0.4$ up to 50K were reported in section §6.2. The real value of $g^{(2)}(0)$ can be obtained from a deconvolution of the experimental data with IRF, in the same way as explained earlier.

To estimate the QD recharging rate $\Gamma_R$ and the $g^{(2)}(0)$ value, we use a two exponential phenomenological equation for $g^{(2)}(\tau)$:

$$g^{(2)}(\tau) = 1 - \beta \cdot \exp(-|\tau| \cdot \Gamma_R) + \alpha \cdot \exp(-|\tau| \cdot \Gamma_D), \qquad (6.5)$$

where α and β ($\beta \le 1+\alpha$) are the constants representing the bunching and antibunching amplitude, respectively, and $\Gamma_D$ is the bunching rate. The red line in Figure 6.7 represent fit with Eq. (6.5) convoluted with the IRF. The convolution of the Eq. 6.5 and 3.2 can be found in **Appendix**.

To reduce the S/N ratio in the $g^{(2)}_{meas}(\tau)$ histogram, the $X^0$ auto-correlation functions for two different detuning values were recorded for the acquisition times much longer ($\Delta t_{acc}$ = 4÷6 hours) than those presented in Figure 6.7. The results are shown in Figure 6.8. The dashed blue line is the fit of the real $g^{(2)}(\tau)$ after deconvolution. The $g^{(2)}(0)$ values of the plots presented in Figure 6.8 were estimated to be 0.1±0.1 for the small detuning (δ = -0.16 meV), and 0.2±0.1 for the large detuning (δ = 0.36 meV). The error bars are relatively high due to long

instrumental response time $\tau_{IRF}$. However, we expect $g^{(2)}(0)$ to be close to zero for $\delta \rightarrow 0$ since the resonant excitation at the *p-shell* excited state can excite only carriers within the QD, so that the background emission is highly reduced [20]. For excitation far from resonance with the excited states the excitation process is less efficient and the single photon emission efficiency decreases.

The dependence of $\Gamma_R$ with the excitation power ($P_{exct}$) at fixed detuning value ($\delta$=0) is plotted in Figure 6.9 (a). It reflects the expected increase according to the expression [28]:

$$\Gamma_R = G + \frac{1}{\tau_X}, \tag{6.6}$$

where G is the pumping rate for non resonant excitation and $\tau_X$ is exciton decay time ($\tau_X=1/\Gamma_0$). The $\Gamma_R$ increase is due to the higher probability of $X^0$ occupation under strong optical excitation. $\Gamma_R$ tends to the experimentally measured $\Gamma_0$ value for the zero excitation power (see §4.3).

The narrowing of the anti-bunching peak that can be observed for $|\delta| \rightarrow 0$ (Figures 6.7 and 6.8) indicates changes in the QD emission dynamics. The $\Gamma_R$ vs. $\delta$ plot in the range between -0.5 meV and 0.6 meV is shown in Figure 6.9 (b) for two excitation powers: 70 kW/cm$^2$ (full symbols), and 140 kW/cm$^2$ (open symbols). The $\Gamma_R$ dependence on $\delta$ follows closely the PLE band (black dots and red curve) and reaches its maximum for $\delta$=0. We attribute this behaviour to the increase of the absorption probability as the excitation energy approaches $E_{p\text{-}shell}$. In consequence *e–h* pair formation is faster and the QD recharge process is shorter for quasi-resonant excitation at the *p-state* than for off-resonant excitation. In other words, quasi-resonant excitation increases the occupation probability of $X^0$ for decreasing $\delta$ in a similar way as for increasing $P_{exct}$. This effect can be formally included as a $\delta$–dependent G in Eq. (6.6).

The phenomenon of photon bunching under quasi-resonant excitation, known as “memory effect”, has been explained by the “blinking” of single QDs [3,16,38]. It is due to the random change of the QD between “bright” and “dark” states, so photons tend to bunch during the bright periods [39,40] causing positive correlation. In our case these “bright” and “dark” states can be naturally assigned to the bright ($BX^0$) and dark ($DX^0$) states of the neutral exciton. Additionally, at high power (equivalent to increased absorption probability or small detuning) many *e-h* pairs coexist in the QD. The time averaged probability of single occupancy is small and it increases after recombination [41].

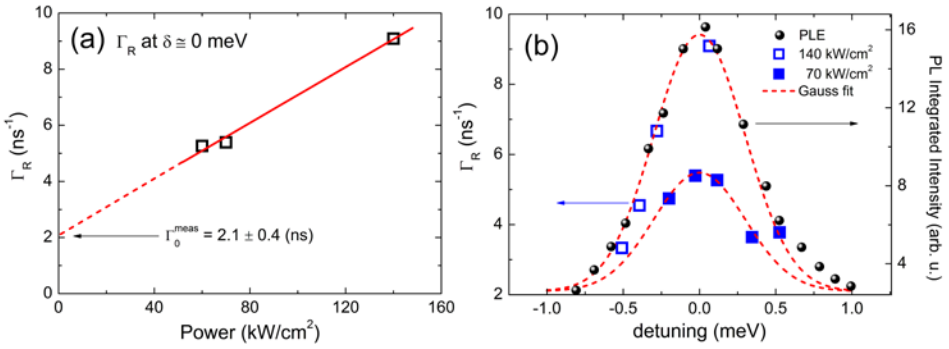


Figure 6.9 (a) Antibunching rate ($\Gamma_R = 1/\tau_R$) vs. excitation power at fixed $\delta$=0. $\Gamma_R$ tends to the experimentally measured $\Gamma_0$ value for the zero excitation power. (b) Antibunching rate vs. excitation detuning from the $E_{p\text{-shell}}$. The $\Gamma_R$ dependence on $\delta$ follows closely the PLE band (black dots) and reaches its maximum for $\delta$=0.

Charged versus neutral exciton states are not likely to be at the origin of the observed bunching [40] as $X^{-1}$ is very weak under quasi-resonant excitation (not shown). The bunching rates are approximately 50 times smaller than the antibunching ones. Contrary to $\Gamma_R$, the $\Gamma_B$ dependence on $\delta$ is not clear due to relatively high experimental noise.

# References


[1] P. Michler, A. Imamoglu, M. D. Mason, P. J. Carson, G. F. Strouse, and S. K. Buratto, Nature (London) **406**, 268 (2000).

[2] P. Michler, A. Kiraz, C. Becher, W. V. Shoenfeld, P. M. Petroff, L. Zhang, E. Hu, and A. Imamoglu, Science **290**, 2282 (2000).

[3] C. Santori, M. Pelton, G. Solomon, Y. Dale, and Y. Yamamoto, Phys. Rev. Lett. **86**, 1502 (2001).

[4] V. Zwiller, H. Blom, P. Jonsson, N. Panev, S. Jeppesen, T. Tsegaye, E. Goobar, M.-E. Pistol, L. Samuelson, and G. Björk, Appl. Phys. Lett. **78**, 2476 (2001).

[5] K. Hennessy, A. Badolato, M. Winger, D. Gerace, M. Atature, S. Falt, E. L. Hu, and A. Imamoglu, Nature 445, 896 (2007)

[6] A. Dousse, J. Suffczyński, R. Braive, A. Miard, A. Lemaître, I. Sagnes, L. Lanco, J. Bloch, P. Voisin, P. Senellart Appl. Phys. Lett. **94**, 121102 (2009).

[7] J. Persson, T. Aichele, V. Zwiller, L. Samuelson, and O. Benson, Phys. Rev. B **69**, 233314 (2004).

[8] G. J. Beirne, M.Reischle, R. Roßbach, W.M. Schulz, M. Jetter, J. Seebeck, P.Gartner, C. Gies, F. Jahnke, and P. Michler, Phys. Rev. B **75**, 195302 (2007).

[9] R.Roßbach, M. Reischle, G. J. Beirne, M. Jetter, and P. Michler, Appl. Phys. Lett. **92**, 071105 (2008).

[10] W.-M. Schulz, R. Roßbach, M. Reischle, G. J. Beirne, M. Bommer, M. Jetter, and P. Michler, Phys. Rev. B **79**, 035329 (2009).

[11] M. Reischle, G. J. Beirne, W.-M. Schulz, M. Eichfelder, R. Roßbach, M. Jetter, and P. Michler, Opt. Express **16**, 12771 (2008).

[12] M. Reischle, G. J. Beirne, R. Roßbach, M. Jetter, and P. Michler, Phys. Rev. Lett. **101**, 146402 (2008).

[13] Y. Masumoto, K. Toshiyuki, T. Suzuki, and M. Ikezawa, Phys. Rev. B **77**, 115331 (2008).

[14] S. Kako, C. Santori, K.Hoshino, S. Götzinger, Y. Yamamoto and Y. Arakawa. *Nature Materials* **5**, 887 (2006)

[15] A. Malko, D. Y. Oberli, M. H. Baier, E. Pelucchi, F. Michelini, K. F. Karlsson, M.-A. Dupertuis, and E. Kapon, Phys. Rev. B **72**, 195332 (2005).

[16] C. Santori, D. Fattal, J. Vučković, G. S. Solomon, E. Waks, and Y. Yamamoto, Phys. Rev. B 69, 205324 (2004)

[17] D. V. Regelman, U. Mizrahi, D. Gershoni, E. Ehrenfreud, W. V. Schoenfeld, and P. M. Petroff, Phys. Rev. Lett. 87, 257401 (2001)

[18] J. Vuckovic, D. Fattal, C. Santori, G. S. Solomon, Y. Yamamoto, Appl. Phys. Lett. 82, 21, 3596 (2003)

[19] E. B. Flagg, A. Muller, J.W. Robertson, S. Founta, D. G. Deppe, M. Xiao, W. Ma, G. J. Salamo and C. K. Shih, Nature Physics 5, 203 (2009)

[20] A. Malko, M. H. Baier, K. F. Karlsson, E. Pelucchi, D. Y. Oberli, and E. Kapon, Applied Physics Lett.s 88, 081905 (2006)

[21] Toshihide Takagahara "*Quantum coherence, correlation and decoherence in semiconductor nanostructures*", §7, pp. 282-365, Elsevier Science Ltd. (2003)

[22] See for instance P. Palinginis, H. Wang, S. V. Goupalov, D. S. Citrin, M. Dobrowolska and J. K. Furdyna, Phys. Rev. B **70**, 073302 (2004);

[23] G.A. Narvaez, G. Bester, and A. Zunger, Phys. Rev. B **72**, 245318 (2005)

[24] M. Wimmer, S. V. Nair, and J. Shumway, Phys. Rev. B **73**, 165305 (2006)

[25] C. Gerry, P. L. Knight "*Introductory Quantum Optics*", Cambrige University Press, §5.4 (2006).

[26] R. Brouri, A. Beveratos, J.-P. Poizat, and P. Grangier, Opt. Lett **25**, 1294 (2000).

[27] B. Lounis, H.A. Bechtel, D. Gerion, P. Alivisatos, and W.E. Moerner, Chem. Phys. Lett. **329**, 399 (2000);

[28] S. Kimura, H. Kumano, M. Endo, I. Suemunei, T.Yokoi, H. Sasakura, S.Adachi, S. Muto, H. Z. Song, S. Hirose and T. Usuki, Japn. J. of Appl. Phys. **44**, L 793 (2005).

[29] D. W. Snoke, J. Hübner, W. W. Rühle, and M. Zundel, Phys. Rev. B **70**, 115329 (2004).

[30] E. Tsitsishvili, R. v. Baltz, and H. Kalt, Phys. Rev. B **67**, 205330 (2003).

[31] M. Bayer, G. Ortner, O. Stern, A. Kuther, A. A. Gorbunov, A. Forchel, P. Hawrylak, S. Fafard, K. Hinzer, T. L. Reinecke and S. N. Walck, J. P. Reithmaier, F. Klopf, and F. Schäfer, Phys. Rev. B **65**, 195315 (2002).

[32] S. Rodt, A. Schliwa, K. Pötschke, F. Guffarth, and D. Bimberg, Phys. Rev. B **71**, 155325 (2005).

[33] C. Pryor, M-E. Pistol, and L. Samuelson, Phys. Rev. B **56**, 10404 (1997).

[34] 26 G. A. Narvaez, G. Bester, A. Franceschetti, and A. Zunger, Phys. Rev. B **74**, 205422 (2006).

[35] 27 M. Bayer, O. Stern, A. Kuther, and A. Forchel, Phys. Rev. B **61**, 7273 (2000).

[36] J. Persson, M. Holm and C. Pryor, D. Hessman, W. Seifert, L. Samuelson, M. E. Pistol, Phys. Rev. B **67**, 035320 (2003).

[37] J. Puls, M. Rabe, H.-J. Wünsche, and F. Henneberger Phys. Rev. B **60**, R16 303 (1999).

[38] C. Zinoni, B. Alloing, L. H. Li, F. Marsili, A. Fiore, L. Lunghi, A. Gerardino, Yu. B. Vakhtomin, K. V. Smirnov, and G. N. Gol'tsman Appl. Phys. Lett. **91**, 031106 (2007).

[39] J. Bernard, L. Fleury, H. Talon and M. Orrit, J. Chem. Phys. 98, 2 (1993).

[40] G. Sallen, A. Tribu, T. Aichele, R. André, L. Besombes, C. Bougerol, S. Tatarenko, K. Kheng, and J. Ph. Poizat, Phys. Rev. B 80, 085310 (2009).

[41] D. V. Regelman, U. Mizrahi, D. Gershoni, and E. Ehrenfreund, W. V. Schoenfeld and P. M. Petroff, Phys. Rev. Lett. 87, 257401 (2005).

# Chapter 7

# Conclusions

The present dissertation provides a detailed study of the optical properties and electronic structure of single InP/GaInP QDs for their potential use as single photon emitters. The main conclusions are the following:

1. The optical emission of small InP QDs (1-2 nm height) embedded in a InGaP matrix has been studied under different conditions of excitation and temperature. Their average spatial separation (~0.2 μm) enables optical access to single QDs without using masks or mesas. A micro-PL set-up with three axes DC-motor stage allows repeatable observation of a single QD emission lines in the range of 660 nm – 670 nm (1.85 eV – 1.88 eV).

2. Micro-PLE spectra recorded for various QDs reveal sharp peaks below the wetting layer (WL) (1.935 eV) corresponding to absorption transitions involving excited states. For energies greater than 1.88 eV one observes an increase and broadening in the PLE spectrum, what is associated to the WL. The small height of the dots and the small valence band offset originates a hybridization of the excited states with the WL continuum, especially in the valence band where the carriers are confined only by strain (negative band-offset).

3. Differences observed in the PL energies (biexciton binding energy and fine structure splitting) and decay time allows us to identify QDs with different sizes. The excitonic decay rates ($\Gamma_X$, $\Gamma_{XX}$) measured in our QDs agree with calculated values by Wimmer et al. (2006). Also the biexciton binding energy lies in the calculated range. Thus, although the model dimensions of the QD used in the calculations are larger than ours, these results suggest that our self-assembled InP/InGaP QDs lie in the intermediate confinement regime.

4. The emission dynamics of the single QDs was measured at different excitation powers and temperatures. The exciton and biexciton decay rates follow the expected power dependent behavior. A progressive increase of the $X^0$ decay time and rather constant $XX^0$ life time for increasing excitation intensity were observed. The temperature dependent TRPL experiment reveals different trends depending on the QD size due to the competition of two thermally activated processes: 1) The phonon mediated spin flip from dark to bright exciton states, which decreases the radiative recombination time of the *e-h* pair; 2) The hole excitation to the excited states or the WL continuum. Depending on the dominating mechanism, the PL decay time will increase (in smaller QDs), decrease (in bigger QDs), or stay constant, if both processes compensate. Above 50 K all QD exhibit a decrease of the decay time due to phonon (mainly zone boundary LA) mediated escape of the carriers to the WL.

5. A continuous and systematic red-shift of the PL exciton emission is observed for increasing excitation energies and intensities in individual QDs. This effect is explained as a band-gap renormalization (BGR) due to many-body interaction. The $X^0$ energy red-shifts up to ~0.4 meV. The emission-energy minima appear with a one-to-one correspondence to emission intensity maxima in the PLE spectrum as a function of the excitation energy. The BGR is explained by hybridization of the QD excited hole states to the WL continuum. The small size of the InP/GaInPQDs brings the excited states close in energy to the wetting layer, enabling hybridization.

6. Modulation of the exciton fine-structure splitting (up to 10%) is observed under quasi-resonant excitation at an excited state with proper fine structure splitting. This phenomenon is originated by the polarization dependent BGR. The advantage over other methods of controlling $\Delta_{FS}$ is an optical access to the sample. However, it is not likely that a total cancellation of $\Delta_{FS}$ is possible by this method.

7. Auto-correlation measurements of the exciton emission reveal photon antibunching for single InP QDs. Under off-resonant excitation the $g^{(2)}(0)$ values remain below 0.2 even for high temperatures due to low background contribution to the QD emission. Quasi-resonantly excited QDs present even smaller $g^{(2)}(0)$ values ($\approx$0.1), as the long relaxation processes and defect charging are highly reduced. For low excitation powers the anti-bunching time measured for the InP QD is in the range of 0.5 ÷0.8 ns, depending on the size of the QD and temperature.

8. A narrowing of the anti-bunching dip is observed for quasi-resonant excitation at excited state (p-state), due to increased absorption-probability as the excitation energy approaches the p-state. Hence the $X^0$ occupation probability

increases for decreasing detuning from the p-state. A similar explanation is applied to the power dependent anti-bunching rate.

9. Temperature dependent measurements of the $X^0$ auto-correlation show a similar behaviour as the exciton decay measured by TRPL. Two competing processes activated thermally: 1) The thermal excitation of holes which increases the anti-bunching rise time ($\tau_R$); 2) The dark-to-bright transition via spin flip which increases the probability of $X^0$ population and hence decreases the $\tau_R$. The activation energy was estimated to be 7÷30 meV depending on the QD size, while the dark-bright exciton splitting was estimated to 3.6 meV for the larger QD.

# Appendix

## Convolution of $g^{(2)}(\tau)$ and IRF

The second order correlation function is expressed by Eq. (3.7):

$$g^{(2)}(\tau) = 1 - \beta \cdot \exp\left(-|\tau|/t_R\right) \tag{A.1}$$

The instrumental response function (IRF) is well described by equation:

$$h(\tau) = \frac{1}{2\tau_{IRF}} \cdot \exp\left(-|\tau|/\tau_{IRF}\right) \tag{A.2}$$

The measured correlation function is a convolution of the Eq. (A.1) with Eq. (A.2), and is expressed as follows:

$$g^{(2)}_{meas}(\tau) = \int_{-\infty}^{\infty} h(\tau - \tau')g^{(2)}(\tau')d\tau' \tag{A.3}$$

The numerical calculation of the (A.3) convolution was done with the MathCad 2001 program. The resulting function has the form:

$$g^{(2)}_{meas}(\tau) = 1 - \beta\left[\frac{\tau_R^2 \cdot \tau_{IRF}}{\tau_{IRF}^2 - \tau_R^2} \cdot \left(\frac{1}{\tau_R} e^{(-|\tau|/\tau_{IRF})} - \frac{1}{\tau_{IRF}} e^{(-|\tau|/\tau_R)}\right)\right] \tag{A.4}$$

Analogue procedure was applied to calculate the convolution of the Eq.(6.5):

$$\begin{aligned} g^{(2)}_{meas}(\tau) = 1 &- \beta\left[\frac{\tau_R^2 \cdot \tau_{IRF}}{\tau_{IRF}^2 - \tau_R^2} \cdot \left(\frac{1}{\tau_R} e^{(-|\tau|/\tau_{IRF})} - \frac{1}{\tau_{IRF}} e^{(-|\tau|/\tau_R)}\right)\right] \\ &+ \alpha\left[\frac{\tau_D^2 \cdot \tau_{IRF}}{\tau_{IRF}^2 - \tau_D^2} \cdot \left(\frac{1}{\tau_D} e^{(-|\tau|/\tau_{IRF})} - \frac{1}{\tau_{IRF}} e^{(-|\tau|/\tau_D)}\right)\right] \end{aligned} \tag{A.5}$$

# List of Figures

# List of Tables

# List of Publications

**Publications in International Journals:**

1. *Thermal effects in InP/(Ga,In)P quantum-dot single-photon emitters*
   A. K. Nowak, E. Gallardo, D. Sarkar, H. P. van der Meulen, J. M. Calleja, J. M. Ripalda, L. González, and Y. González,
   Physical Review B **80**, 161305(R) (2009)

2. *Temperature dependent single photon emission in InP/GaInP quantum dots*
   A. K. Nowak, E. Gallardo, D. Sarkar, D. Sanvitto, H. P. van der Meulen, J. M. Calleja, J. M. Ripalda, L. González, and Y. González,
   Physica E 42, 2509–2513 (2010)

3. *Single-photon emission by semiconductor quantum rings in a photonic crystal*
   E. Gallardo, L. J. Martínez, A. K. Nowak, D. Sarkar, D. Sanvitto, H. P. van der Meulen, J. M. Calleja, I. Prieto, D. Granados, A. G. Taboada, J. M. García, and P. A. Postigo,
   Journal of The Optical Society Of America B Vol. **27**, No. 6, A21 (2010)

4. *Band-gap renormalization in InP/GaxIn$_{1?x}$P quantum dots*
   A. K. Nowak, E. Gallardo, H. P. van der Meulen, J. M. Calleja, J. M. Ripalda, L. Gonzalez, and Y. Gonzalez,
   Physical Review B **83**, 245447 (2011)

**Other publications**:

1. *Relaxation of persistent photo-conductivity in Ga-doped Cd(1-x)Mn(x)Te*,
   E.M. Popko, A.K. Nowak, J. Szatkowski, Z. Gumienny, A. Augousti (Poster)
   Proc. SPIE, Vol. 5957, 59571J (2005)

2. *Capture barrier for DX centers in gallium doped Cd(1-x)Mn(x)Te*
   Ewa Placzek-Popko, Anna Nowak, Jan Szatkowski, Kazimierz Sieranski,
   Journal of Applied Physics **99**, 083510 (2006)

3. *Investigation of the Quantum Confinement Effects in CdTe Dots by Electrical Meaurements.*
   E. Placzek-Popko, A. Nowak, G. Karczewski, T. Wojtowicz, M. Wiater, M. Guziewicz, Z. Gumienny
   ICPS Conf. Proc. Vol. 893, pp. 813-814 (2007)

4. *On the stretched-exponential decay kinetics of the ionized DX centers in gallium doped $Cd1_xMn_xTe$*
   J. Trzmiel, E. Placzek-Popko, A. Nowak, K. Weron, Z. Gumienny
   Physica B 404, 5251–5254 (2009)

5. *Optical coupling of two distant InAs/GaAs quantum dots by a photonic-crystal microcavity*
   E. Gallardo, L. J. Martínez, A. K. Nowak, D. Sarkar, H. P. van der Meulen, J. M. Calleja, C. Tejedor, I. Prieto, D. Granados, A. G. Taboada, J. M. García, and P. A. Postigo,
   Physical Review B **81**, 193301 (2010)

6. *Emission polarization control in semiconductor quantum dots coupled to a photonic crystal microcavity*
   E. Gallardo, L. J. Martínez, A. K. Nowak, H. P. van der Meulen, J. M. Calleja, C. Tejedor, I. Prieto, D. Granados, A. G. Taboada, J. M. García, and P. A. Postigo,
   Optics Express Vol. 18, No. 12, 13301 (2010)

**Participation in International Conferences:**

1. *Photoconductivity kinetics of DX related center in Ga-doped Cd(1-x)Mn(x)Te*
   E. Placzek-Popko, J. Szatkowski, J. Trzmiel, A. Nowak, A. Hajdusianek, P. Becla (Poster) Congress: International School in Semiconducting Compounds, Jaszowiec, Poland 2004

2. *Decay kinetics of photoconductivity in Ga-doped CdMnTe*
   E.M. Popko, A.K. Nowak, J. Szatkowski, Z. Gumienny, A. Augousti (Poster) Congress: Eurocongress SPIE, Optics and Optoelectronics, Warsaw, Poland 2005

3. *Electrical Properties of CdTe Quantum Dots*
   A. Nowak, E. Placzek-Popko, T. Wojtowicz, M. Guziewicz, Z. Gumienny, G. Karczewski (Poster) Congress: International School in semiconducting compounds, Jaszowiec, Poland 2006

4. *Investigation of the Quantum Confinement Effects in CdTe Dots by Electrical Meaurements*
   E. Placzek-Popko, A. Nowak, G. Karczewski, T. Wojtowicz, M. Wiater, M. Guziewicz, Z. Gumienny (Poster) International Congress in Physics of Semiconductors, Vienna, Austria 2006

5. *Temperature dependent single photon emission in InP/GaInP quantum dots*
   A. K. Nowak, E. Gallardo, D. Sarkar, D. Sanvitto, H. P. van der Meulen, J. M. Calleja, J. M. Ripalda, L. González, and Y. González (Poster) Congress: EP2DS18-MSS14, Kobe, Japan 2009

6. *Size and temperature effects on single photon emission in InP/GaInP quantum dots*
   A. K. Nowak, E. Gallardo, D. Sarkar, D. Sanvitto, H. P. van der Meulen, J. M. Calleja, J. M. Ripalda, L. González, and Y. González
   (Poster) Optics of Excitons in Confined Systems 11, Madrid, Spain 2009

7. *Single photon emission and quantum ring-cavity coupling in Inas/GaAs quantum rings*
   E. Gallardo, L.J. Martínez, A.K. Nowak, D. Sarkar, D. Sanvitto, H.P. van der Meulen, J.M. Calleja, E. del Valle, F. Laussy, C. Tejedor, I. Prieto, A.R. Alija, D. Granados, A.G. Taboada, J.M. García and P.A. PostigoCongress: Optics of Excitons in Confined Systems 11, Madrid, Spain 2009

8. *Temperature effects on the dynamics of InP/(Ga,In)P quantum dot single-photon emitters*
   A. K. Nowak, M. D. Martín, E. Gallardo, H. P. van der Meulen, L. Viña, J. M. Calleja, J. M. Ripalda, L. González, and Y. González (Poster) Congress: International Congress in Physics of Semiconductors, Seul, Corea 2010

9. *Exciton emission dynamics of single-photon emitters based on InP/(Ga, In)P quantum dots*
   M. D. Martín, A. K. Nowak, E. Gallardo, H. P. van der Meulen, L. Viña, and J. M. Calleja, J. M. Ripalda, L. González, and Y. González, Conferecnia Española de Nano-fotonica, Segovia, Spain 2010

10. *Puntos cuánticos de InP/(Ga,In)P como emisores de fotones individuales*
    A. K. Nowak, (Oral presentation)
    Conference: XIII Jornada de Jóvenes Científicos del Instituto de Ciencia de Materiales Nicolás Cabrera, Residencia La Cristalera, Miraflores de la Sierra, MADRID, Spain 2010

11. *Many-body effects in InP/GaInP quantum dots under p-state quasi-resonant excitation*.
    A. K. Nowak, E. Gallardo, H. P. van der Meulen, J. M. Calleja, J. M. Ripalda, L. Gonzalez, and Y. Gonzalez (Poster) Congress: EP2DS19-MSS15, Tallahassee, Florida, US 2011

12. *Band-gap renormalization in quantum dot excitons under quasi-resonant excitation*
    A. K. Nowak, E. Gallardo, H. P. van der Meulen, J. M. Calleja, J. M. Ripalda, L. Gonzalez, and Y. Gonzalez, (Poster) Congress: OECS 12, Paris, France 2011